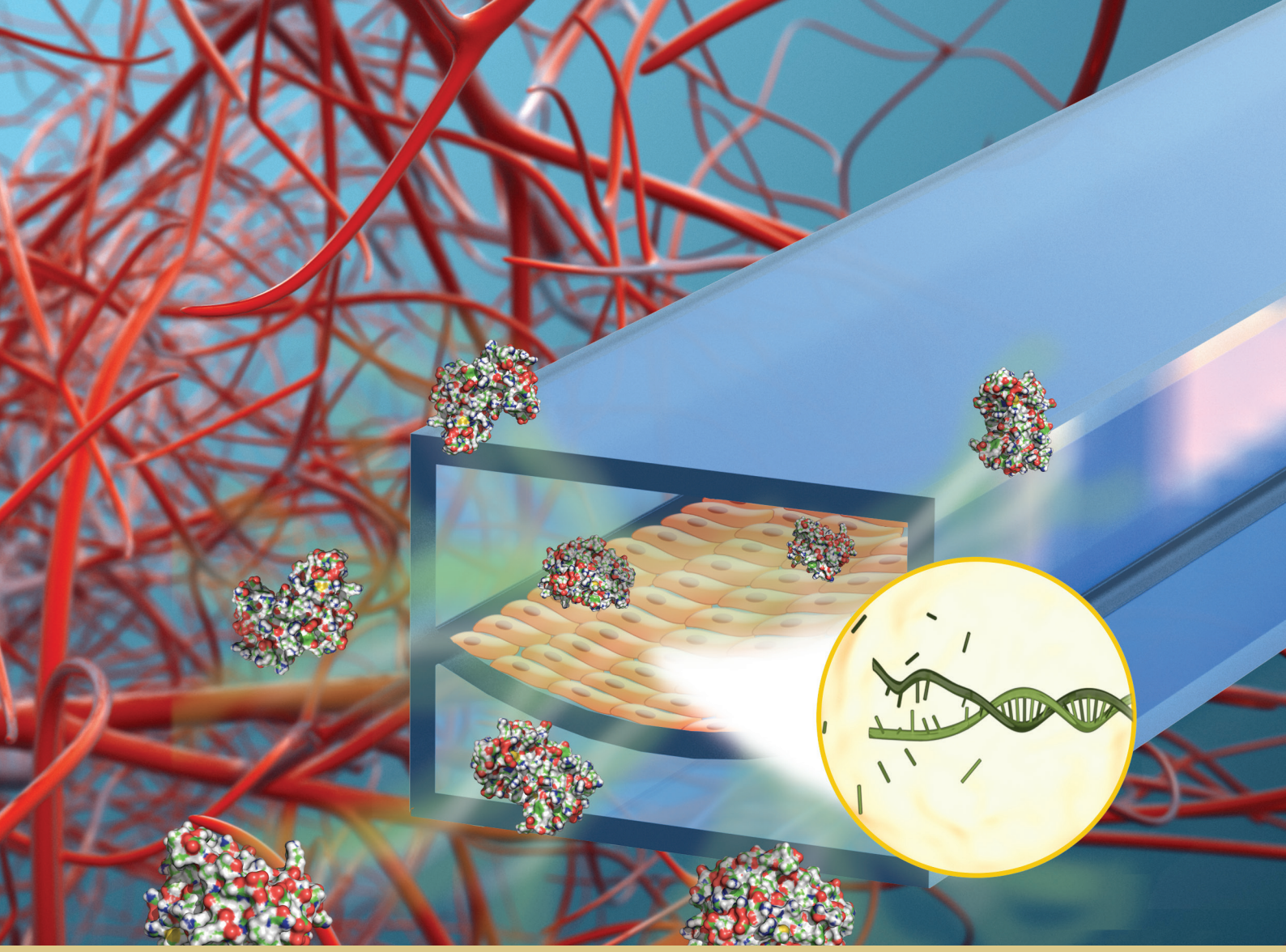

João Carlos Ribas de Almeida

VASCULAR ORGAN-ON-A-CHIP PLATFORMS FOR DISEASE MODELING

Tese de Doutoramento em Biologia Experimental e Biomedicina, ramo de Biotecnologia e Saúde,
orientada pelo Doutor Lino Ferreira e pelo Doutor Ali Khademhosseini,
apresentada ao Instituto de Investigação Interdisciplinar da Universidade de Coimbra

Junho de 2017

· U C ·

UNIVERSIDADE DE COIMBRA

João Carlos Ribas de Almeida

VASCULAR ORGAN-ON-A-CHIP PLATFORMS FOR DISEASE MODELING

June 2017

Thesis submitted to the Institute for Interdisciplinary Research of the University of Coimbra to apply for the degree of Doctor in Philosophy in the area of Experimental Biology and Biomedicine, specialization in Biotechnology and Health

UNIVERSIDADE DE COIMBRA

FINANCIAL SUPPORT AND WORKPLACE

This thesis experimental work was performed at the Kadehmosseini Laboratory of Harvard Medical School, Brigham and Women's Hospital, and Harvard-MIT Health Sciences and Technology Division, in Boston, Massachusetts, USA. We acknowledge the funding from the Portuguese Foundation for Science and Technology, the National Institutes of Health, and the Defense and Threat Reduction Agency.

HARVARD
MEDICAL SCHOOL

BRIGHAM
AND
WOMEN'S
HOSPITAL

FCT
Fundação para a Ciência e a Tecnologia
MINISTÉRIO DA CIÊNCIA, TECNOLOGIA E ENSINO SUPERIOR

NIH National Institutes of Health

Index

Abstract

Organs-on-chips have emerged as viable platforms for expediting the drug development process. These systems potentially enable the prediction of human responses towards pharmaceutical compounds, and the development and testing of nanomedicines, chemicals, and even biopharmaceuticals. In the past decade, advances in microfluidics technologies have facilitated the development of organs-on-chips as simple, reproducible, and scalable platforms that recapitulate organ-level functions, by incorporation of biological materials such as cells and biophysical cues. The use of a small number of cells and culture media volume makes this approach cost effective and scalable. Different microfabrication techniques have enabled the creation of dynamic microenvironments to apply shear stress, strain, and/or interfaces on different biological materials. In this context, the cardiovascular system is one of the most important organ systems where biophysical forces play a crucial role.

Millions of people are diagnosed every year with different cardiovascular diseases, and aging represents the number one risk factor. In this context, organ-on-a-chip devices hold promise to revolutionize drug discovery by unveiling responses unobserved using conventional cell culture systems that lack the dynamics of living systems, potentially expediting the drug discovery process. Additionally, with the advent of organs-on-a-chip, a new set of tools and sensors is required to monitor cell responses in real-time and harness the potential of the technology.

Here, we first provide a broad landscape analysis on the state-of-the-art organ-on-a-chip technologies. We identify challenges and opportunities in the cardiovascular arena, and lay out areas of potential benefit in the drug development pipeline. We have developed a new progeria-on-a-chip device to examine the effects of biomechanical strain in the context of vascular aging and disease. The vasculature-on-a-chip recapitulates markers of hypertension under pathological strain, which are observed under angiotensin II treatment. Smooth muscle cells derived from human induced pluripotent stem cells of Hutchinson Gilford Progeria Syndrome donors, but not from healthy donors, showed an exacerbated

inflammatory response to strain. In particular, we observed increased levels of inflammatory markers, as well as DNA damage. Pharmacological intervention with a statin or a farnesyltransferase inhibitor reversed the strain-induced damage by shifting gene expression profile away from inflammation.

In addition, we have developed a set of tools to operate and monitor organ-on-a-chip systems. We have first created a mini-microscope capable of real-time monitoring of cell morphology and behavior, either under bright light or fluorescence. Such monitoring approach allows the cheap and scalable integration of imaging analysis to organ-on-a-chip systems. Finally, we have developed an Augmented Reality solution to monitor and control organ-on-a-chip devices via Google Glass. The set of software and hardware created allow performing research remotely, when experimental conditions present a danger to the experimenter. The tool also aims to lay ground on the future applications of augmented reality in laboratory settings.

The devices and tools created in this thesis aim at providing a platform to be implemented in drug discovery platforms, allowing high-throughput control and analysis of multiple test conditions in a model of vascular disease and aging.

Keywords: organ-on-a-chip, microfluidics, sensors, cardiovascular, progeria.

Resumo

As plataformas de sistemas microfisiológicos têm emergido como aceleradores do desenvolvimento e descoberta de novos fármacos. Estes sistemas têm o potencial de prever respostas humanas a diferentes compostos farmacêuticos, de desenvolver e testar novos nano-fármacos, compostos químicos e biológicos com potencial terapêutico. Na última década, avanços nas técnicas de microfluídica têm facilitado o desenvolvimento de sistemas microfisiológicos como plataformas simples, reprodutíveis e escaláveis que recapitulam as funções de órgãos humanos, tanto pela incorporação de materiais biológicos, como de células e propriedades biofísicas. A utilização de fluidos em micro-canais é desejável devido às reduções nas quantidades de células e reagentes utilizados, tornando-se mais facilmente escalável. Adicionalmente, novas técnicas de microfabricação permitiram a criação de microambientes dinâmicos para aplicar tensão de corte, tensão e/ou interfaces de diferentes materiais biológicos. Neste contexto, o sistema cardiovascular é um dos sistemas de órgãos mais importantes onde as forças biofísicas desempenham um papel crucial.

Milhões de pessoas são diagnosticadas a cada ano com diferentes doenças cardiovasculares, sendo o envelhecimento o primeiro fator de risco. Neste contexto, os dispositivos de órgão-num-chip prometem revolucionar a descoberta de fármacos através da descoberta de respostas não observadas usando sistemas de cultura de células convencionais, potencialmente acelerando o processo de descoberta de fármacos. Além disso, com o aparecimento de sistemas microfisiológicos, um novo conjunto de ferramentas e sensores é necessário para monitorar as respostas das células em tempo real e utilizar o potencial da tecnologia.

Esta tese começa primeiramente com uma análise do estado da arte em sistemas microfisiológicos. Identificamos desafios e oportunidades na área cardiovascular e definimos áreas de benefício potencial no pipeline de desenvolvimento de medicamentos. Desenvolvemos plataformas de vasculatura-num-chip e progeria-num-chip para examinar os efeitos da tensão biomecânica no contexto de envelhecimento e doença vasculares. A plataforma de vasculatura-num-chip recapitula marcadores de hipertensão sob tensão

patológica, que são observados sob tratamento com angiotensina II. Células vasculares de músculo liso derivadas de células-tronco pluripotentes induzidas, obtidas de dadores humanos com Síndrome de Progeria de Hutchinson Gilford mostraram uma resposta inflamatória exacerbada à tensão biomecânica, enquanto as de dadores saudáveis não mostraram alterações. Em particular, observamos níveis aumentados de marcadores inflamatórios, bem como danos no DNA. A intervenção farmacológica com uma estatina ou com um inibidor de farnesiltransferase reverteu os danos induzidos pela tensão biomecânica, normalizando o perfil de expressão de genes pró-inflamatórios.

Além disto, desenvolvemos um conjunto de ferramentas para operar e monitorar sistemas microfisiológicos. Foi criado um mini-microscópio capaz de monitorar em tempo real a morfologia e o comportamento das células, com ou sem fluorescência. Esta abordagem de monitoramento permite a integração económica e escalável de análises de imagem em sistemas microfisiológicos. Finalmente, desenvolvemos uma solução de Realidade Aumentada para monitorar e controlar sistemas microfisiológicos através do Google Glass. O conjunto de *software* e *hardware* criado permite realizar experiências remotamente, quando as condições experimentais representam um perigo para o investigador. A ferramenta visa também ser um ponto de partida para futuras aplicações de realidade aumentada em ambientes laboratoriais.

Os dispositivos criados nesta tese visam fornecer uma plataforma para ser implementada na descoberta de novos fármacos, permitindo o controlo e análise em escala de várias condições de teste num modelo de envelhecimento e doenças vasculares.

Palavras-chave: sistemas microfisiológicos, microfluídica, sensores, cardiovascular, progeria.

Acknowledgments

As soon as I experienced the scientific and entrepreneurial spirit of Boston I knew I had to be in this amazing city. I am truly grateful to all the learning and mentorship I got from Prof. Ali Khademhosseini. It has been an incredible journey and I learned how to be a full stack scientist/engineer: I learned how to do science, how to write papers, how to finish things (!), how to write grants and how to be better leader. The mantra “full speed ahead” truly resonates with the ability I acquired to get things done in an efficient, structured, and scientific way. I also want to acknowledge my co-supervisor Dr. Lino Ferreira, for inspiring me to work hard, aim high, ask deep questions, and also for being confident on my capabilities to lead the project. The quality of my work is a mirror of his dedication to outstanding science. I will be ever grateful to Prof. João Ramalho-Santos for believing in my capabilities, and giving me the opportunity to be part of this big scientific family of the Doctoral Programme in Experimental Biology and Biomedicine – you have taught me how to think critically, which is my most valuable asset.

To my class, Joana, André, Sara, Dominique, Nina, Mariline, António, Tânia, Marcelo, Patrícia, and Sofia, it was a fantastic ride. Thank you for teaching me so much, for all the crazy parties, hard work, and lasting friendship. Together, we shook the entire center, and we showed that our capabilities go beyond scientist to leaders.

To all the great people that has taught me so much during my stay in Boston, specifically Yu Shrike Zhang, Seila Selimovic, Jeroen Roukema, Jorge Uquillas, Jeroen Leijten, Gaurav Kaushik, Su-Ryon, and Shabir. I am forever grateful.

To all the fantastic lab mates I have had through my stay in the lab, which are too many to name, but I will try: Solange, Nupura, Mario, Serena, Peter, Preethi, Jessi, Carol, Julio, Cristina Colosi, VJ, Mattia, japanese duo Shuichiro and Koji, Andrea, Alejandro, Ljupcho, Ludovic, Antonia, Pip, Laura, Haelin, Claudio, Settimio, Queralt, Jeremy, Federica,

Adam, Zaya, Vanessa, Antea, Amir H., Gyan, Alessio, Aditya, James, Marco, Sara Kashaf, Shivesh, Claudia Del Toro, Valeria, Beatrice, Anna P., Sofia Pando, Inés, Daniel, Arianna, Guillermo, Ricardo Medina, Wanjun, Simone, Francesco, Marcel, Martina, Chiara, Parastoo, Kimia, Razieh, Amir Nasajpour, Daniel Hosseini, Yinan, Illaria, Gita, Federico, Jacopo, Xuan, Parissa, Xiaofei, Aaron, Ram, Jana, Laurie, Fatemeh, Mohsen, Yi-Chen, Saghi, Mehmet, Amir Manbachi, Ali Tamayol, Qingmeng, Praveen, Jin, Jungmok, Cha, Luiz, Samaneh, Andrea Vegh, Emal, Camilla, Nadia, Alessandro Polini, Ryan, Kan, Grissel, Mario, Iman Noshadi, Akhtar Nazman, Ayça, Poh, Huanan, Juliana Cardoso, Wojciech, Juliane, Ana, Julia, Lara, Courtney, Luisa, Giovanni, Anna Desalvo, Reggie, Mansi, Jessica, Arushi, Nonni, Irene, Fabio Busignani, Tugba, Moritz, Fabio de Ferrari, Vinicius, Arameh, Mahwish, Raquel, Nuno, Silvia, among many many others! The super lab managers Brett, Wesley and Vinny, and my favorite MIT UROP, Nancy Hung. In memory of a good scientist and friend, Masoumeh Ghaderi.

To the entire Portuguese community in Boston, New York and entire United States. Most of you have contributed to a continuous feeling of home away from home. Thank you for all the good moments, support, and friendship. It would have not been the same without you, Ana Tellechea, Catarina Seabra, Mariana Oliveira, João Neto, Joana Abreu, Mariana Silva, Inês de Sousa Lima, João Ricardo Santos, Catarina Nogueira, Francisco Feijó Delgado, Joana Nunes, Paulo Martins, João Caixinha, Patrícia Amaro, Ana Metelo, Paulo Gameiro, Ângela Crespo, Sofia Ribeiro, André Soares, Dário, Ana Cadete, Elsa Abreu, João Íncio, Bruno Oliveira, Inês Andrade, Madalena Barroso, Catarina Costa, Inês Tenente, Ivana, Nuno Martins, Sílvia Curado, Raúl Saraiva, Ana Rita Moreira, Luís Miguel Oliveira, Irina Ramos, Joana Ricou, Andreia Gomes, Luís Barros, among so many others.

A very special acknowledgment to Daniel Santos (the greatest flat mate ever!), Sofia Ribeiro (first hosted me in Boston), Ângela Crespo, Joana Guedes, for helpful scientific discussions and lending me some much needed reagents. Patrícia Pitrez, thank you so

much for your help, advice, and availability in sending me some of the cells you developed. This would not have been possible without your contribution and ground-breaking work.

To the entire MIT Hacking Medicine team, especially Chris, Tatyana, Hari, and Zen. Your advice transformed me, and what I experienced organizing hackathons around the world was priceless. Thank you for welcoming me in this big healthcare hacking fam.

To my parents and brother, whose strength, love, and character have shaped me to become what I am today.

CHAPTER I

GENERAL INTRODUCTION

Adapted from João Ribas, et al., and Ali Khademhosseini, “Cardiovascular Organ-on-a-Chip Platforms for Drug Discovery and Development”, Applied In Vitro Toxicology, 2(2): 82-96 (2016); and Nupura Bishe, João Ribas, et al., and Ali Khademhosseini, “Organ-on-a-chip platforms for studying drug delivery systems”, Journal of Controlled Release, 190: 82-93 (2014).

CHAPTER 1 – General Introduction

Cardiovascular diseases (CVDs) are the most frequent causes of death in the United States (US) (1). In 2011, 800,000 people were killed by CVDs; approximately 60% of those deaths were attributable to coronary heart disease (such as myocardial infarction [MI]) and hypertensive heart disease (1). CVD also includes atherosclerosis and other vascular cell dysfunctions that can result in occlusion and thrombosis, leading to several complications, and, in severe cases, to acute MI (2). Over the years, heart failure has been treated with numerous interventional (3) and pharmacological agents (4-6). Among these approaches, the control of blood pressure with lipid lowering drugs and other pharmacological agents such as angiotensin-converting enzyme inhibitors and beta-blockers may limit myocardial remodeling, slow down the progression of heart failure, and decrease heart failure associated mortality (4-7). Despite these surgical and pharmacological interventions in the treatment of end-stage heart failure and associated co-morbidities, there is still a strong need for new and improved treatments. However, drug discovery and development has seen a decline each year in approved drugs.

The cost of developing a new drug varies approximately between $0.8-$1.2 billion US dollars (8). After an intensive and costly research period, new drug candidates are subjected to clinical trials to assess safety and efficacy, prior to regulatory decision by the US Food and Drug Administration (FDA). However, despite extensive preclinical laboratory and animal testing, high rates of potential drug candidates still fail in clinical trials, especially during later stages of development (9, 10). For instance, in 2000, clinical safety (such as toxicity) and efficacy issues accounted for approximately 30% of drug project failures (11). Between 1991 and 2000, the rate of clinical trial success in cardiovascular drug development was as low as 20% (11). Moreover, over the past five decades, cardiovascular safety issues and cardiotoxicity have been a major reason for drugs being rejected or retracted from the market (12-14). This can be partially attributed to the lack of effective and predictive preclinical models. Although conventional two-dimensional (2D) cultures and animal (disease) models

have successfully contributed to the development of a wide range of therapeutics, many of these models do not adequately mimic human *in vivo* conditions. For example, there are essential genetic and metabolic differences between human and animals that can lead to significant pharmacokinetic differences (15). As a result, limiting factors in drug development such as toxicity and inefficacy require the development of better, more predictive and more human-like *in vitro* models to assess the safety and efficacy of potential new drugs. Ideally these models should consist of platforms in which biochemical, physical and electro-chemical factors can be integrated and controlled in order to recapitulate the dynamic microenvironment of tissues *in vivo*.

Several studies have been able to microengineer biologically relevant heart and vascular tissue models *in vitro* (16, 17). The development of these three dimensional (3D) tissue engineered micro-tissues can potentially be used for *in vitro* drug testing, disease modeling and biological mechanistic studies (18-20). Moreover, these models exhibit the physiological characteristics of myocardium and blood vessels due to the presence of tissue-like properties such as multiple cell interaction (eg. paracrine signaling and cell-cell signaling), cell-extra cellular matrix (ECM) interactions and mechanical stimulation. More interestingly, in the past few years, novel microfluidic platforms have been introduced and have led to the creation of biomimetic cardiovascular tissue *in vitro* (21-25). These microfluidic organs-on-a-chip can recapitulate important organ-level functions, multicellular micro-architecture and environment dynamics, thus providing a technological platform capable of accelerating cardiovascular drug development. Therefore, these engineered and novel heart- and vasculature-on-a-chip systems could contribute to the development of suitable high-throughput platforms for drug development and disease modeling of major CVDs such as MI, hypertension, heart failure and atherosclerosis.

Here, we describe and discuss the advances in the past decade in the development of heart- and vasculature-on-a-chip platforms to study cardiovascular physiology and disease, pinpointing their successes and shortcomings. Additionally, we identify opportunities for *in vitro* disease modeling and drug development. Lastly, we discuss the challenges for the

validation of such platforms and potential applications on the pharmaceutical industry drug development pipeline.

1.1. Heart-on-a-chip platforms in drug discovery

1.1.1 Mimicking cardiac environment

Cardiac tissue contractile function is mediated through cardiomyocytes (CMs) that are organized in parallel arrays of myofibril bundles. The contractility of CMs is mediated through chemical, mechanical and electrical stimuli (26, 27). In addition to CMs, cardiac tissue is composed of fibroblasts and microvessels, which consist of endothelial cells (ECs) and vascular smooth muscle cells. Cellular composition and anisotropic organization, together with continuous exposure to multiple dynamic stimuli plays a critical role in maintaining cardiac physiological function (28-30). Microfluidic *in vitro* heart-on-a-chip platforms can provide precise individual control over each these essential factors, allowing for novel opportunities to study cardiac physiology, pathology and pharmacology. In particular, these platforms may hold great promise for the development of high-throughput assays that could be valuable in drug screening and toxicity studies (21, 22, 24, 25, 31).

Recent advances have enabled the engineering of physiologically relevant micro-scale myocardial tissues by using microfluidic organ-on-a-chip systems. Such systems are often fabricated using poly(dimethyl siloxane) (PDMS) due to its biocompatibility, non-toxicity and low cost (32, 33). In addition, PDMS is an elastomeric and transparent material that can be rapidly prototyped and customized into a microfluidic system by using soft and photolithography techniques (32). However, the hydrophobic nature of PDMS limits the attachment and spreading of cells (33). This challenge can be addressed by treating the PDMS surface with proteins (e.g. fibronectin) that facilitate cellular attachment (33). Recently, Annabi *et al*. (34), developed a technique to overcome this challenge by coating microfluidic channels with hydrogels (Figure 1A), which provided a suitable environment for on-chip cardiac cell culture. Specifically, methacrylated tropoelastin (MeTro) and gelatin methacryloyl (GelMA) facilitated cellular adhesion inside the microfluidic channels (34), which was also

reported in other cell types (35, 36). The seeded CMs revealed not only an increased attachment, but also proliferation and beating rate on MeTro hydrogels compared to GelMA (Figure 1B) (37). This was mainly attributable to the presence of cell-interactive amino acid sequences and the more elastic nature of tropoelastin compared to GelMA. In addition, continuous perfusion of medium though the heart-on-a-chip platform provided the possibility to mimic blood flow-induced shear stress on myocardial tissue. Therefore, this platform could potentially be useful to study biomimetic cues on cardiac function. The results of this study suggest that tropoelastin-based hydrogels might offer a suitable microenvironment for proper functioning of CMs *in vitro*. Important properties of tropoelastin that support this are the tunable elasticity and biocompatibility. Moreover, this microfluidic system could be used to study safety and efficacy of drugs under physiologic-like conditions (37).

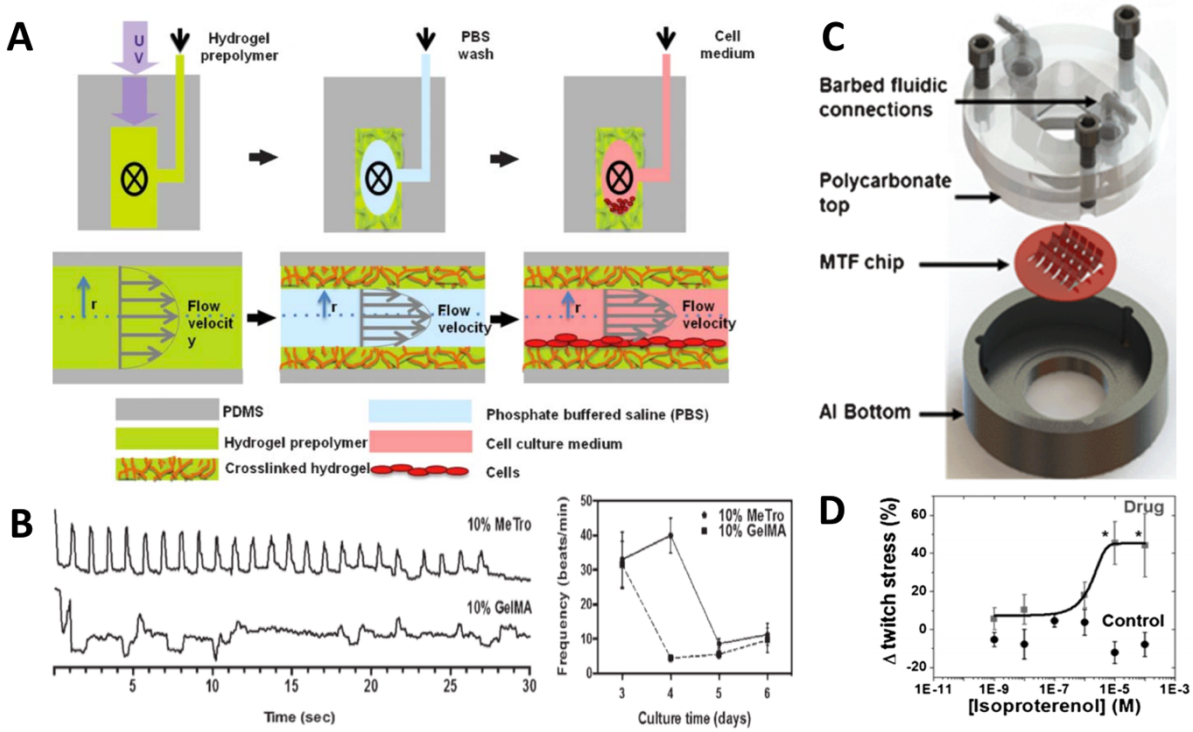

Figure 1.1 – (A) Schematic of a PDMS-based microfluidic heart-on-a-chip model developed to culture cardiomyocytes. These microfluidic channels were coated by gelatin and tropoelastin-based hydrogels to induce cellular attachment. (B) The effect of (10% (w/v) tropoelastin and (10% (w/v) gelatin-based hydrogels on the beating pattern (left) and beating frequency (right) of cardiomyocytes (CMs) inside microfluidic microchannels. (C) The schematic of a heart-on-a-chip microdevice designed for pharmacological testing. (D) The effect of isoproterenol on the contractility of CM-seeded muscular

thin films, showing an increase in beating rate compared to control. Adapted from Khademhosseini *et al*. (34) and Parker *et al*. (38)

Although native myocardial cells, scaffold elasticity, and (natural) ECM proteins are critical to engineering biomimetic cardiac tissues *in vitro*, additional components of native heart tissue are required to recapitulate proper cardiac tissue function. Here, we will highlight some of these factors and discuss their use and application in the fabrication of heart-on-a-chip devices.

One of the factors important for the fabrication of heart-on-a-chip devices is electrical stimulation and CM anisotropy. *In vivo*, myocardial pumping arises from the electrical stimulation of CMs by automated pacemaker cells in the sinoatrial node. These electrical signals propagate through the left and right atria to go to the atrioventricular node and eventually reach the right and left ventricles. As a result, the anisotropic and elongated CMs are depolarized, which results in regular and synchronized cardiac muscle contraction. Consequently, external electrical stimulation and an anisotropic organization of CMs may contribute to the development of more physiologic *in vitro* heart tissue. Anisotropic alignment of CMs and ECM significantly affects electrical and mechanical functioning of cardiac tissue (39, 40). Integrating structural and functional anisotropy used in cardiac tissue engineering (41) into heart-on-a-chip devices could result in better contractile force generation and better electrical propagation of action potentials (41). Grosberg *et al. (42)* used a muscular thin film (MTF)-technique to design a heart-on-a-chip with anisotropically organized CMs. MTF platforms were created by microcontact printing fibronectin patterns on a thin, deformable PDMS film, later seeded with primary neonatal rat ventricular CMs. Additionally, the self-organized CMs on the functionalized surface were electrically stimulated by platinum electrodes. By electrically stimulating CMs on the chip, the *in vivo* generation of electrical signals by pacing cells could be recapitulated. Moreover, electrical stimulation of cells increased the cellular alignment, differentiation and functionality of engineered cardiac tissue (43). This study showed that contractile behavior and electrophysiological properties such as the action potential morphology of MTFs could be measured successfully. Consequently,

these measurements could be used in the evaluation of pharmacological intervention on the contractile function of multiple cardiac microtissues. Using a dose-range experiment the effect of epinephrine concentration on the frequency of contractions was calculated based on the MTF contractility stress profiles. This demonstrates that MTFs in a microfluidic chip can be used to assess contractility in the presence of drugs or physiologic-like cues such as hydrodynamic, mechanical and electrical stimuli. Although this 2D monolayer of CMs provides an opportunity to analyze deformation of cardiac microtissue in a 3D manner, it is not able to recapitulate the 3D microenvironment of myocardial tissue. A solution to this challenge could be found by combining cellular encapsulation and microengineering strategies to form aligned 3D microtissues (44).

A similar MTF approach was used to create an aluminum based microdevice for high-throughput pharmacological testing of isoproterenol (Figure 1C) (38). This platform provided the advantage of a semi-automated fabrication method that could be scaled-up and automated for higher throughput screening of drugs. Moreover, a metallic heating element, electrodes, and a transparent top were incorporated in the device for simultaneous temperature control, electrical field stimulation and optical contraction analysis respectively. The microfluidic device's high throughput capacity was leveraged to test the effect of isoproterenol on the contractile stress of MTF's (Figure 1D). In this experiment, a series of increasing drug concentrations were tested within the same microdevice. The MTF's showed an increase in contractility stress when compared to control. Furthermore, by using this system, authors were able to show the same level of isoproterenol potency *in vitro* compared to reported values for rat hearts.(38) This microdevice enabled the incorporation of an MTF-based heart-on-a-chip and allowed automatic fluidic control, wash-in and washout after each drug dosage. In addition, this system was shown to be suitable for simultaneous analysis of cardiac tissue contractility during drug compound testing. Thus, demonstrating its ability to perform rapid and accurate drug analysis. Consequently, this microdevice could potentially improve pharmacological *in vitro* studies on a higher throughput.

A cell culture chip to form *in vitro* cardiac microtissues through the application of

electrical stimulation and topographical cues was created by Heidi Au and colleagues (45). Here, neonatal rat CMs were seeded and cultured onto polystyrene cell culture chips with integrated topographical microgrooves. CMs showed attachment and alignment along the grooves. In addition, electrical stimulation of the CMs increased the cellular maturation in terms of sarcomeric protein (such as sarcomeric alpha-actinin) and gap junction protein expression.

Another factor important for the fabrication of heart-on-a-chip device is cardiac tissue perfusion. The complex architecture of myocardial tissue, consisting of cardiac bundles and associated micro-vessels, can be more accurately recreated by fabricating *in vitro* systems that can recapitulate cardiac tissue perfusion. Xiao *et al. (46)* designed a more physiologically relevant heart-on-a-chip by creating a perfusable cardiac micro-tissue with a poly(tetrafluoroethylene) micro-tubing to induce CMs to align and elongate along the tubing template. This system demonstrated the feasibility of mimicking cardiac tissue by showing spontaneous beating, expression of sarcomeric troponin-T and gap junction markers (Connexin-43). In addition, the functionality of this system as a platform for pharmacological studies was examined by testing the system with nitric oxide (NO). After exposure to NO for 24 hours, the beating rate of the CMs was significantly decreased in comparison with the untreated control. These results indicate that this platform could serve as suitable biomimetic *in vitro* system for both drug development and drug-induced changes in beating behavior.

1.1.2 Cardiac disease models

Many stem cell-based, tissue engineered and organ-on-a-chip systems for *in vitro* modeling of cardiac disease have been developed. Cardiac diseases such as rhythm disorders (47, 48) and dilated cardiomyopathy (49) have been studied by using induced pluripotent stem cells (iPSCs) in monolayer disease models. In addition, cardiac conditions including myocardial infarction (MI) and re-entry arrhythmia have been successfully re-created in 2D tissue engineered heart models (50). Although these models were able to represent specific phenotypic disease characteristics, they still lack the incorporation of

proper environmental factors such as 3D cell-ECM and cell-cell interactions. To overcome this hurdle, several biomaterials have been mixed with different cell sources (eg. iPSCs, rat neonatal ventricular cells) toward the development of 3D structures of cardiac disease models (51-54). Recent advances in the field of microfluidics have allowed researchers to construct novel heart-on-a-chip systems for disease modeling and drug testing. Next, we will summarize some of the recent findings on the development of these microfluidic systems.

Several chronic CVDs, such as hypertension and aortic valve stenosis, can cause pressure overload in the left ventricle and lead to cardiac hypertrophy and fibrosis (55). Increased mechanical stress during disease is a critical factor that drives the initiation of hypertrophy, fibrotic remodeling and heart failure (56, 57). These dynamic changes are partly attributable to mechanotransduction, a process in which external mechanical forces are translated into internal chemical and electrical cellular responses.(58) Therefore, it is important to develop an *in vitro* heart-on-a-chip model that can provide insight into the pathophysiology of this phenomenon. McCain *et al.* (59) successfully applied a MTF platform towards the creation of a failing myocardium on-a-chip (60). Mechanical cyclic stretch of the MTFs resulted in pathological tissue remodeling, with several genetic indicators of pathological remodeling being up regulated. Furthermore, by the application of transverse stretch, structural organization of micropatterned CMs was disrupted, resulting in disorganized cardiomyocytes similar to hypertrophic cardiomyopathy (Figure 2A) (59, 60). Further development of similar heart failure on-a-chip models could potentially aid in a better understanding of cardiac remodeling.

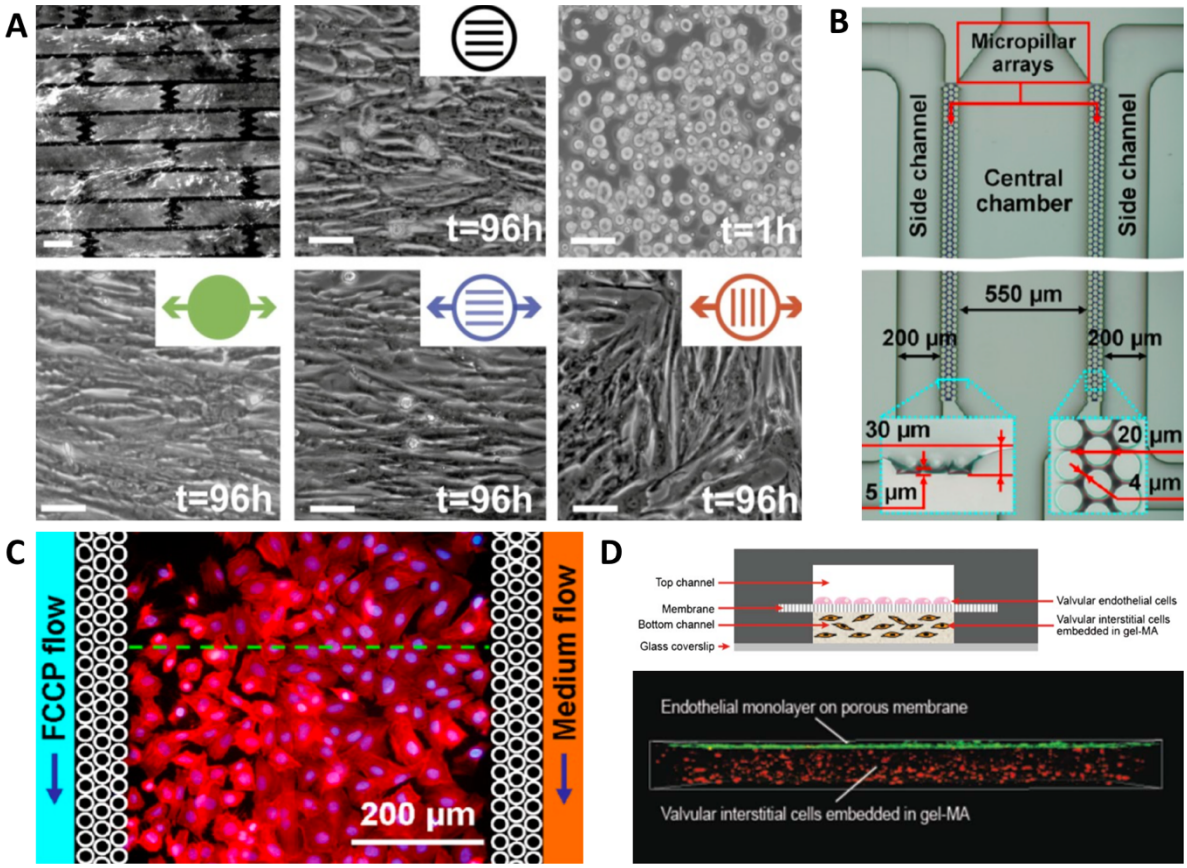

Figure 1.2 – (A) The effect of transverse mechanical stretch showing a disorganized architecture of cardiomyocytes cultured on muscular thin films (scale bar 50µm)(59). (B) Schematic illustration of a microfluidic heart-on-a-chip model that resembles the native interface of myocardial cells and microcapillaries. Reprinted with permission from Wang *et al*.(61) (copyright 2013 American Chemical Society). (C) Representation of fluorescence images of cytoskeletal changes in cardiomyocytes under hypoxic conditions, which were induced by the introduction of an oxygen consumption blocker in one of the microfluidic side-channels. Reprinted with permission from Wang *et al*.(61) (copyright 2013 American Chemical Society). (D) Schematic representation of a bi-compartmental co-culture of valvular endothelial (VEC) and valvular interstitial cells (VIC) (top panel). VECs were embedded on a thin and porous membrane on top of a VIC loaded gelatin methacryloyl (GelMA) (bottom channel)(62).

Ren *et al. (61)* fabricated a heart-on-a-chip to study hypoxia-induced myocardial injury. By designing a PDMS-based microfluidic device with four functional units, the interface of myocardial tissue and microcapillaries was mimicked *in vitro*. The four units consisted of a central cell culture chamber and two lateral channels that were separated from each other by micropillar arrays, representing the interface between the blood vessel and cardiac tissue (Figure 1.2B). To mimic hypoxia-induced conditions, a specific oxygen consumption blocking reagent, FCCP (cyanide *p*-trifluoromethoxyphenylhydrazone), was

introduced in one of the side channels (Figure 1.2C) (61). CMs presented normal attachment, spreading and proliferation under normoxic conditions, but underwent morphological changes such as shrinkage and disassembling of intracellular actin bundles after induction of hypoxia. During myocardial ischemia (or MI) there is an increased CM apoptosis, a feature that was accurately recapitulated within this device.

Various (stem) cell transplantation therapies for cardiac repair after MI have gained considerable attention in the past several years (63). Many groups have explored the potential of numerous cells types such as embryonic stem cells, cardiac progenitor cells, skeletal myoblasts and induced pluripotent stem cells (iPSC) (63). To study the interactions as well as the potential role of skeletal myoblasts in the repair of hypoxia-injured CMs, a comparable microfluidic device was created in a follow-up study by He *et al*. (64) in this system, skeletal myoblasts and rat CMs were co-cultured in separate chambers that were connected through permeable micro-valves. The results of this study demonstrated that skeletal myoblasts were capable of repairing the hypoxia-injured CMs through cell-cell interactions.

Hydrogels and microfluidic systems that are developed to mimic myocardial tissue could also be leveraged to mimic valvular tissue and disease (62). Chen *et al. (62)* used a multi-compartmental approach to design a valvular and vascular compartment in a 3D microenvironment, allowing cells to communicate through paracrine signaling (Figure 2D). The cells were separated by a thin porous membrane that enabled the paracrine communication of valvular endothelial cells (VECs) and valvular interstitial cells (VICs). Fibroblast-like VICs were encapsulated in GelMA hydrogels and VECs seeded on fibronectin coated PDMS microchannels. In addition, VECs could be stimulated physiologically by the introduction of flow induced shear stress. Activation of quiescent VICs into alpha smooth muscle actin (α-SMA) expressing myofibroblasts are thought to be one of the hallmarks of valvular pathological remodeling, due to their increase in ECM synthesis and contractile features (65, 66). Myofibroblasts also have the ability to increase calcium deposition by differentiating into osteoblast-like cells (67). Consequently, myofibroblasts play an important

role in calcific aortic disease and valvular fibrosis (68, 69). A study by Chen *et al. (62)* showed that VECs are able to inhibit VIC activation under both static and dynamic fluid flow, which is in line with *in vivo* conditions. This biomimetic microfluidic system could be used to study biological and pathological VEC-VIC interaction, as well as drug-associated toxicity. In addition, this platform may be an appropriate testing model for potential drug candidates in treatment of aortic valve disease.

Recent developments in stem cell biology have further enabled the use of patient specific iPSC-derived CMs for generating *in vitro* models of cardiac disease (70). These advances may lead to the creation of physiologically and genetically relevant models of cardiac disease for drug discovery and drug toxicity (71). By using iPSCs, MTF and microfluidic technologies, Wang *et al. (72)*, successfully engineered the cardiomyopathy of Barth syndrome (BTHS) in an *in vitro* disease model (72). iPSCs were generated from patients with BTHS and subsequently differentiated into patient specific iPSC-derived CMs. In this study, the pathophysiology of BTHS cardiomyopathy was demonstrated by seeding iPSC-derived CMs on MTF's. The BTHS derived cardiac microtissues were shown to have impaired sarcomeric structures as compared to control. Additionally, MTF's from BTHS iPSC-CM revealed a significantly lower contractile performance compared to controls under the same conditions. Moreover, this Barth syndrome on-a-chip was used to test potential therapeutic options (e.g. pharmacological and genetic modifications), indicating its suitability for identifying new therapeutic targets.

All together, these studies point towards a better understanding of CM physiology under a range of dynamic conditions. The new *in vitro* models of heart-on-a-chip present a strong step towards testing cardiotoxicity in human-relevant models, but models of disease are still an area with challenges and opportunities.

1.2. Blood vessel-on-a-chip platforms in drug discovery

1.2.1 Mimicking vascular environment

It is challenging to mimic the vascular environment of the human body *in vitro.* Arteries, arterioles, veins, venules, and capillaries are all part of the vascular system, but differ in the structural and cellular compositions. In addition, blood vessels are subject to a range of biophysical stimuli due to the pulsatile nature of blood flow. ECs lining the lumen of vessels experience flow-induced pulsatile wall shear stress and transmural pressure. ECs and vascular smooth muscle cells (VSMCs) both experience cyclic mechanical stretching, which causes the vessels to increase in diameter in response to blood flow. Hemodynamic parameters contribute to the maintenance of homeostasis in the vessel wall, with several microfluidic models studying the effects of hemodynamics *in vitro* (73-75). Since the vascular system is constantly under these biophysical stimuli, microfluidic technologies are an advantageous way to model these forces. Recently, microfluidic-based platforms have been described for several vascular applications (75), including the formation of tissue engineered vascular networks, angiogenesis and vascular disease models. The end goal of such models is to gain mechanistic and contextual insight on the vascular biology processes, while providing a superior platform for drug discovery and development.

The use of hydrogels in microfluidics is a simple platform to provide relevant 3D matrixes to vascular cells, while maintaining the ability to apply shear stress. Kim et al. used the flexibility of PDMS to generate a microfluidic device (Figure 1.3A) capable of containing fibrin matrices (76). The multi-channel device enabled the study of vasculogenesis and angiogenesis, and the fibrin matrix was able to support cell growth. Kim and colleagues were able to show the formation of a perfusable vascular network, and the maintenance of barrier function. Additionally, the vascular networks under flow exhibited an increased nitric oxide production compared with static conditions (76) (Figure 1.3B-C). Similar methodologies have been used with different hydrogels (77-80) with the end goal of creating vascular networks *in vitro* to study different aspects of vascular biology. Morgan et al. (79) used Type I collagen gels with embedded cells and hollow channels that were later seeded with ECs. This simple

system allows for the creation and design of defined microvascular endothelialized geometries that are useful for the study of permeability and blood-vasculature interactions in a tissue-engineered construct (79). In another example, Wang et al. (80) utilized sodium alginate as artificial templates to cast a hydrogel mixture containing gelatin, agarose and collagen. The resulting matrices were seeded with HUVECs, and displayed good barrier properties and response to flow. Other fibrin-based approaches have been pursued in combination with other cell types (78, 81). Hasenberg et al. (78) aimed to incorporate capillary networks in fibrin gels for multi organ-chip constructs; these vascular network were stable in serum-free media, which is an important aspect to in designing such systems for drug development. Schimek et al. (82) designed a similar microfluidic chip; however, they focused on designing an on-chip peristaltic micropump to provide the vascular network with pulsatile shear stress.

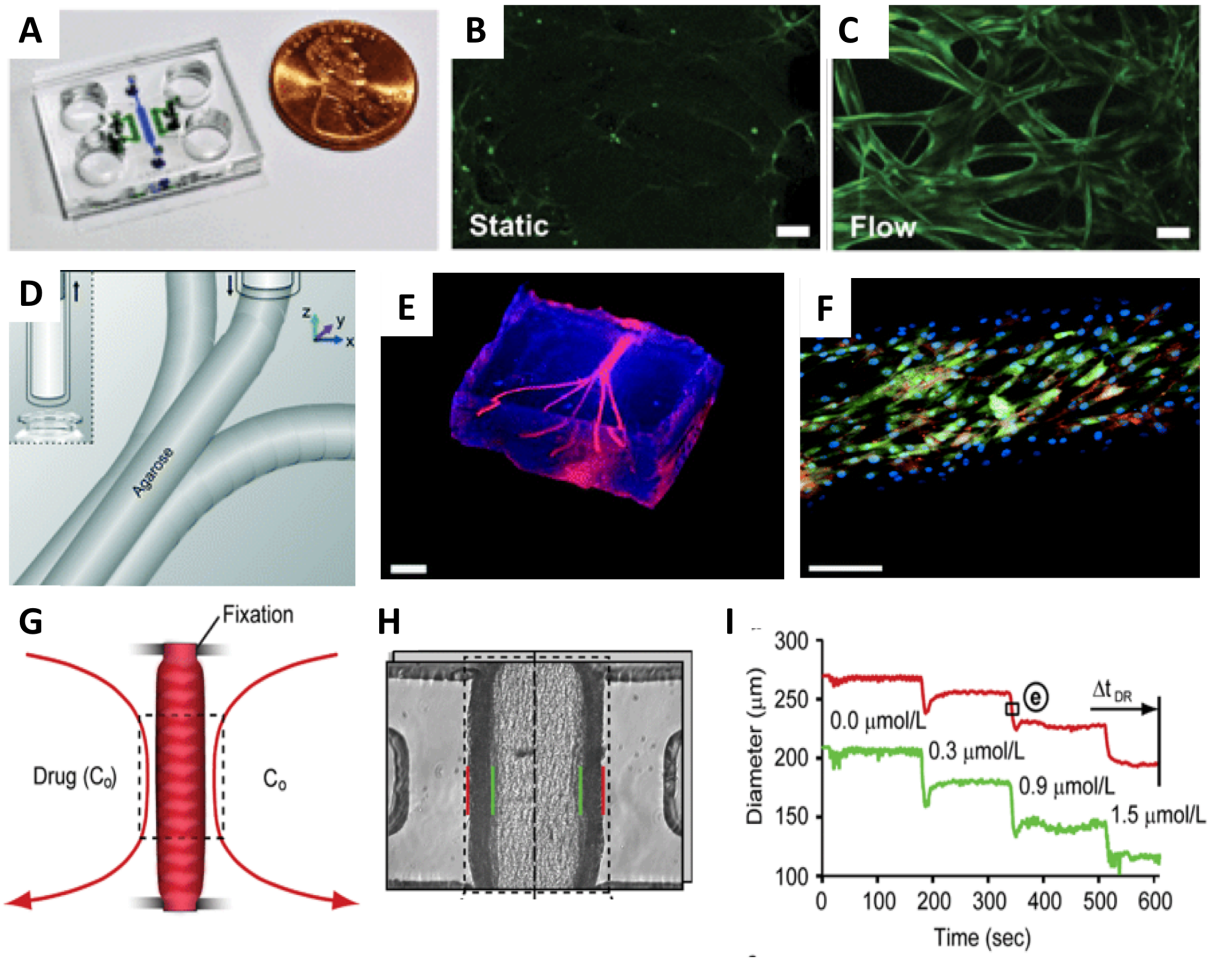

Figure 1.3 – In vitro microfluidic models to study vascular networks and vascular functions. (A) Microfluidic chip for forming vascular networks and to study angiogenesis; (B-C) nitric oxide production in static and flow conditions inside the device A (scale bar 50μm); (D) bioprinting methodology to produce vascular networks with agarose sacrificial layers; (E) bioprinted network (scale bar 3mm); (F) bioprinted vascular network with ECs (green: GFP; blue: DAPI; red: CD31; scale bar 250μm); (G) artery-on-a-chip model where a small mouse artery segment is held in place and perfused through the lumen and outside walls; (H) microphotograph of artery-on-a-chip model (red, outer side wall; green, inner side wall); (I) response of the artery-on-a-chip to phenylephrine. [(A-C) adapted from Jeon *et al*. (76); (D-F) adapted from Khademhosseini *et al*. (77); (G-I) adapted from Bolz *et al*. (83).]

Others have used different fabrication techniques such as bioprinting to achieve these vascular networks (77). In one example, Khademhosseini et al. utilized bioprinting of template sacrificial layers to generate vascular networks in hydrogels (Figure 1.3D). Combined with UV-crosslinkable GelMA hydrogels, this bioprinting methodology allows an on-demand precise control of micro-architectures, yielding potentially complex structures that can mimic different vascular regions (Figure 1.3E-F) observed in the human body (77). This bioprinting approach can generate 3D constructs in a fast, controllable and inexpensive way, which can be useful for testing drug compounds in a wide range of vascular flow settings and on a large scale. These technologies (84) aim to create 3D vascular beds utilizing a wide range of hydrogels. This allows the fine-tuning of mechanical properties and ECM cues to target the specific regions of interest in the vascular system. The potential of such systems can have a direct impact in drug discovery by mimicking *in vitro* vascular tissue microenvironments.

Conversely, some studies have used microfluidics in combination with *ex vivo* vascular segments (83, 85). Günther et al (83) generated a small but complex microfluidic device that captures a mouse mesenteric artery segment and holds it in place. Once this segment is fixed, it can be imaged and exposed to drugs through the lumen or external wall (Figure 1.3G-H). The contraction or dilation of the artery segment can be imaged upon drug exposure. The exposure to phenylephrine in this system resulted in a segment contraction in a dose-dependent way (Figure 1.3I). Although this represents a major step forward in

microfluidics for vascular drug discovery and development, the usage of animal vessels limits its application and translational relevance to humans.

1.2.2 Vascular platforms for probing drug delivery carriers

Novel tools allow new ways to manufacture and test drug delivery systems. This section will emphasize particularly on how can vascular platforms leverage in vitro testing, design and efficacy of drug delivery carriers.

Some studies have already reproduced geometric features of vasculature, including straight channels (86-89), bifurcations (90, 91), and a mixture of more complex features (92). By mapping and replicating a microvascular network from a hamster muscle, a small microfluidic platform was created, reproducing several geometric features including bifurcations and tortuosities, as well as accounting for different shear stresses along the branches (92). Such models acquire extreme importance to evaluate drug delivery carriers, especially when these carriers are to be injected in the blood stream. Interactions of those with the vasculature can be studied with microfluidic models, observing the influence of activated cell-populated surfaces or interactions with blood components. For instance, using microfluidic models *versus* static conditions provides better nanoparticle homogeneity, and reduces the effect of sedimentation observed in the latter (93). Particle size also plays a role. Another microfluidic vascular model showed differences in margination between micro- and nanospheres. Nanospheres show less propensity to locate to the margins, which contrasted with microspheres (94). This important factor, as well as hemodynamics and hemorheology, should be taken into account when designing drug delivery carriers targeted for vascular diseases and cancer. These carriers can also interfere and interact with blood components. Interestingly, in one study, despite no changes in platelet viability, high concentrations of mesoporous silica nanoparticles greatly increased platelet aggregation and adhesion to endothelium (87), emphasizing other parameters apart from viability.

One key aspect that vascular models are able to mimic is the influence of shear stress (88, 90, 95). It influences the endocytic uptake of nanoparticles by endothelial cells,

putatively *via* cytoskeleton reorganization (95), being an important factor in the designing of drug delivery carriers. Narrowing in particular regions of the vascular system exhibit increased shear stress, which becomes important in the development of thrombosis setting. The design and use of shear-sensitive particles, in a model mimicking a vascular narrowing, allowed the usage of 100-fold lower dose of tissue plasminogen activator to observe the same effects (88). Smart particles, which respond to biophysical cues, can target drugs more efficiently, reduce dosage and concomitantly undesired secondary effects (88).

Further vascular microfluidic models consider other aspects, such as particle functionalization (86, 90). Platforms can model the influence of particle functionalization combined with either shear stress (86) or geometric features as straight versus bifurcating channels (90). Some studies highlight the role of particle shape (91, 96). In fact, shape can regulate adhesion to endothelium: comparing to sphere-shaped, rod-shaped nanoparticles show high specific targeting and lower non-specific accumulation (96). When engineering and designing novel carriers, one should take these shape effects into consideration.

Microfluidic technologies have the potential for scalability and high throughput analysis. In the context of analyzing and evaluating drug delivery carriers, current models could be combined with existing technological platforms. Such platforms can, for instance, characterize populations of nanoparticles in a quick and low cost manner (97), or even evaluate endothelial permeability (89). Moreover, characteristics of microfluidics, such as hydrodynamic focusing (98), can make the models more powerful. Integration with vascular microfluidic platforms can give rise to new and improved tools for the assessment of drug delivery systems.

Several of the discussed models have the potential to leverage drug delivery by probing the efficacy and mode of action of its carriers. A future challenge that still remains to elucidate is the prioritization of parameters, and, perhaps, how to combine several (to all) features in a single, high throughput capable, device. Finally, when considering the targeting of vascular diseases, angiogenesis in cancer and usage of injectable drug delivery systems, the relevancy of vasculature models is assuredly recognized.

1.2.3 Vascular disease models

Animal models can sometimes provide insights on the structure of vascular networks. Rosano et al. (92) mapped a mouse cremaster muscle and used it to build a PDMS mold of the vascular network. This biomimetic vascular model can be analogous to human vascular structures, possessing different geometries and regions with different shear stresses. Such models can comprise complex bifurcation and geometric intricacies inherent to vascular networks that change the way cells interact with drugs. Importantly, they can potentially be applied to generate individualized vascular networks and simulate scenarios of thrombus formation or atherosclerosis formation.

Besides recreating vascular structures *in vitro*, researchers have also pursued models to study angiogenesis (99, 100). Galie et al. (100) highlighted the influence of shear stress in angiogenic sprouting. Both wall shear stress and transmural flow in the endothelium above a certain threshold (>10 dyne/cm^2) induce endothelial sprouting. Local narrowing of blood vessels induces high shear stress regions, which can trigger further sprouting. Such information can be valuable in the context in pharmacological interventions that promote or inhibit angiogenesis. In a cancer setting, vascular microfluidic tools can help identify molecules inhibiting tumor angiogenesis and help elucidate the relationship of tumor extravasation in the vasculature. In order to better understand the early phase of metastatic processes, some microfluidic models have been designed to study the process of tumor extravasation (101-103). Buchanan et al. (101) used co-cultures of MDA-MB-231 and ECs to study tumor angiogenesis. Interestingly, high wall shear stress had protective effects, down-regulating several genes important for tumor angiogenesis such as MMP9, HIF1 and VEGFA. Jeon et al. (102) used a microfluidic device to develop a 3D model of metastatic breast cancer extravasation in different environments. Using a bone and muscle-mimicking environment, extravasation rates were found significantly increased in the bone-mimicking models. This microfluidic model elucidated the effects of different microenvironments and their effect in cancer cell extravasation. Additionally, the blockage of A_3 adenosine receptors

in cancer cells resulted in increased extravasation, enabling a deeper mechanistic insight into cancer extravasation, while also providing a valuable platform to test new pharmaceutical agents.

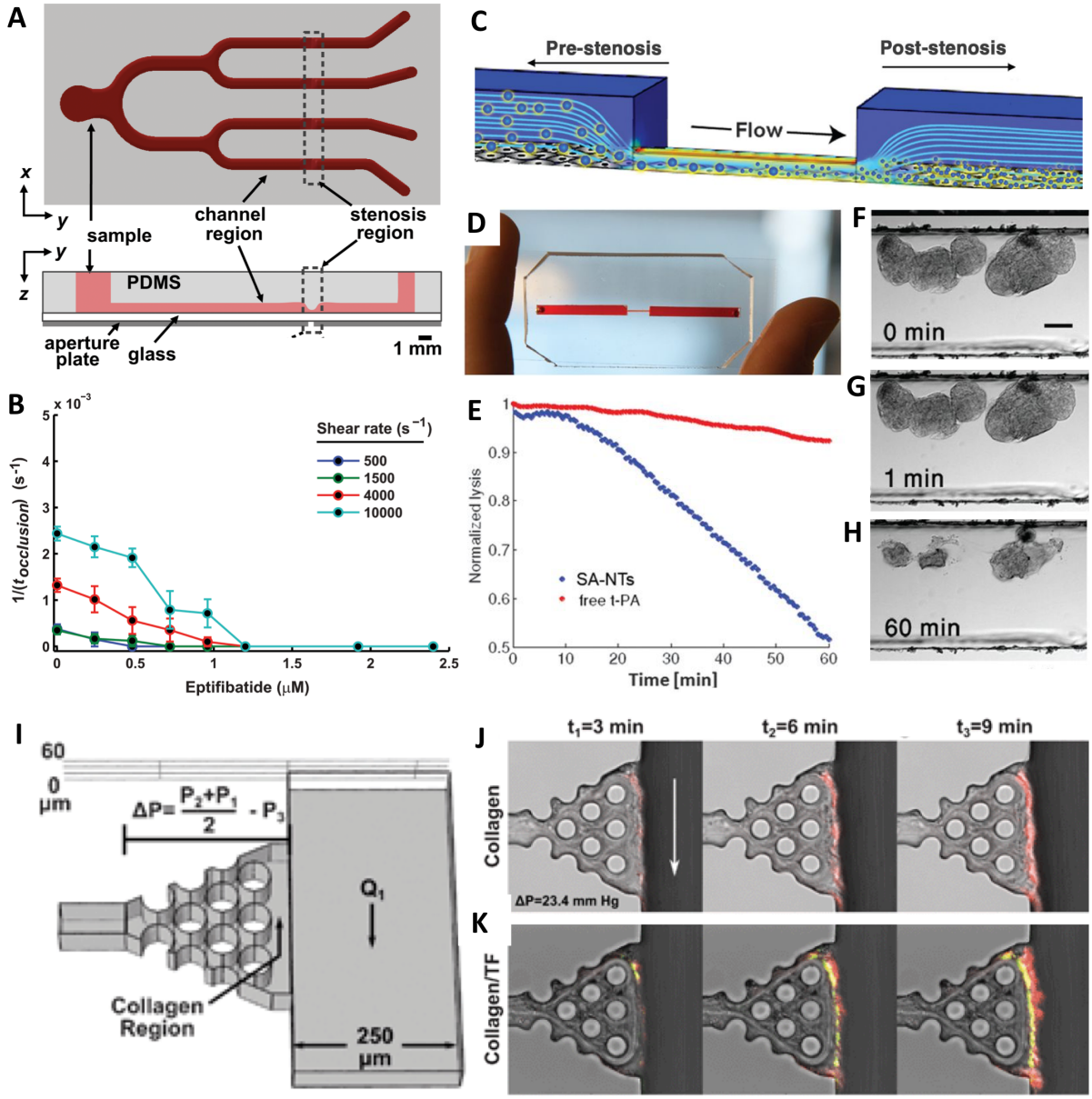

Figure 1.4 – Vascular models to study stenosis and thrombosis *in vitro*. (A) Microfluidic model of stenosis to study the effect of drugs on occlusion; (B) effect of drug epitifibatide concentration on dissolving clots over time; (C) Microfluidic stenosis model used to test shear-activated microparticle formulation; (D) photograph of the microfluidic device; (E) exposure of clots to free or encapsulated t-PA (shear-activated microparticles); (F-H) time dependent thrombolysis of clots upon exposure to encapsulated t-PA; (I) microfluidic device to study thrombosis *in vitro* containing a flow region (Q1) and a collagen region were pressure gradient is varied (ΔP); (J-K) thrombus formation on collagen and collagen/TF hydrogels (white arrow indicates flow direction). [(A-B) adapted from Forest *et al*. (104); (C-H) adapted from Ingber *et al*. (88); (I-K) adapted from Diamond *et al*.(105).]

Several microfluidic platforms have been used for *in vitro* drug screening (106) and for the development of drug delivery systems (24). Microfluidic models can be applied to study thrombosis (104, 105), occlusion (107) and stenotic regions (88). Li et al. (104) designed a microfluidic system (Figure 1.4A) to study stenotic regions and thrombus formation under different shear rates. Low shear rates lead to longer occlusion times. However, the administration of increasing concentrations of the antiplatelet eptifibatide (Figure 1.4B) in high shear stress did not reduce the occlusion times compared to no drug. This highlights the need of studying drug effects, *in vitro*, together with relevant biophysical stimuli such as shear rates. Another system mimicking a stenotic region (Figure 4C-D) was used to design a “smart” drug (88). Blood vessels are often narrowed in thrombotic regions. At this site, wall shear stress can rapidly increase by two orders of magnitude. Korin et al. (88) engineered microparticles that were responsive to shear stress that would thus breakup into smaller nanoparticles when exposed to the shear stresses observed in stenotic regions. By incorporating tissue plasminogen activator (tPA) in the nanoparticles, Korin et al. were able to show local delivery and rapid thrombolysis (Figure 1.4E, F-G). This innovative platform illustrates how microfluidic biomimetic vascular systems can be used in the context of drug development. In this field, researchers have used the physical properties of the stenotic regions to target drugs, thus avoiding the need for systemic delivery of tPA and the resultant adverse side effects. Other vascular models have been used to study drug carriers and physical characteristics (24, 91, 108). Thrombotic and stenotic models are closely related; Muthard et al. (105) engineered a microfluidic system (Figure 1.4I) to probe the effects of wall shear stress and trans-thrombus pressure gradients in the thrombogenesis. In this system, a side flow region was filled with collagen gel with the pressure across it controlled by computer. The collagen area was exposed to the main fluidic channel and visualized directly on the device. As expected, the perfusion of whole blood induced thrombus formation at the collagen site (Figure 1.4J-K). Interestingly, by varying the pressure gradient in the trans-thrombus collagen area, the authors observed a decrease in thrombin

with higher pressure-gradients. This device is an extremely useful tool to assess thrombotic areas and the hemodynamics of pressure gradients in the vessel wall.

1.2.4 Vascular permeability and dynamic condition models

Studies have also been conducted to evaluate the involvement of ECs in wound healing (109). In order to better understand the vascular wound healing processes, Franco et al. (109) focused on the combined effect of flow and topographical cues on endothelial migration. A device was fabricated combining 1 μm-grated surfaces and a fluid flow parallel to these gratings. Interestingly, ECs cultured in such surfaces exhibited a much faster migration velocity compared to flat surfaces under the same flow rate. The research highlights the role of surface modifications and topographical microarchitectures, particularly ones mimicking the basal matrix, in wound healing. Therefore, in certain settings, wound healing might benefit from approaches to change topography, in addition to pharmacological interventions.

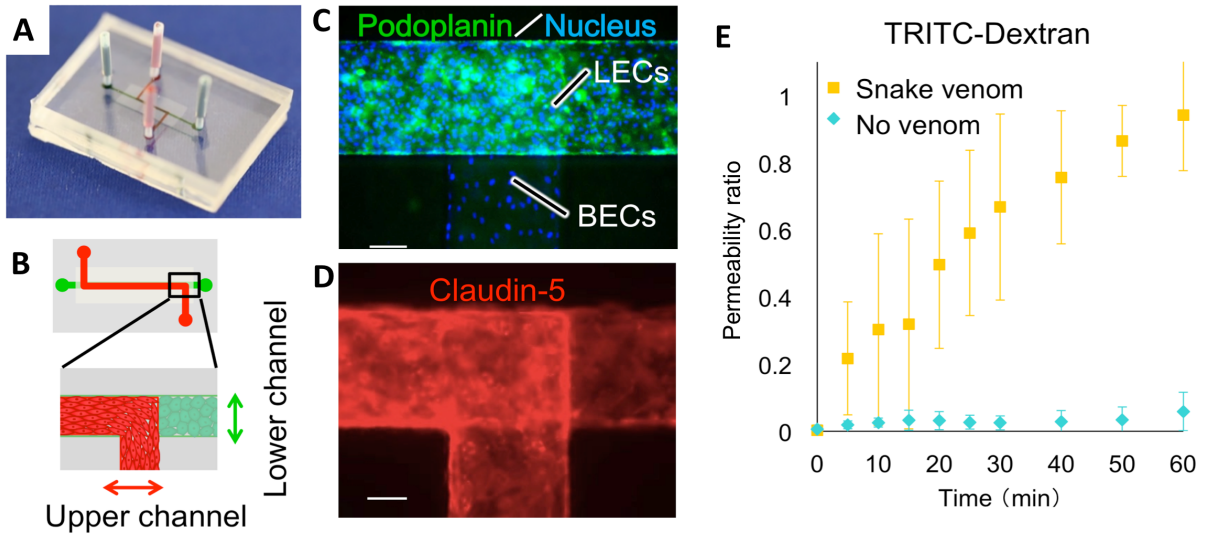

Figure 1.5 – Microfluidic model to study vascular permeability. (A) photograph of microfluidic dual-channel model to study permeability under shear stress; (B) schematic of the microfluidic device with the upper channel containing blood endothelial cells (BECs) and the lower channel containing lymphatic endothelial cells (LECs), separated by a porous membrane; (C) immunostaining for LECs marker podoplanin (green) and DAPI (blue); (D) immunostaining with endothelial specific marker claudin-5; (E) changes in permeability induced by exposure to habu snake venom. (Adapted from Sato *et al.*(110))

In a recent study by Arends et al. (111), the authors developed a microfluidic device to probe the diffusive transport of analytes through basal lamina interfaces. By using ECM gels made from Engelbreth–Holm–Swarm sarcoma of mice, the authors were able to study permeability and the accumulation of different molecules at the interface. The accumulation of molecular at the ECM gel interface was charge-selective, and the results were corroborated *in vivo*. The system provides a platform to screen drugs and evaluate how changes in properties can affect interactions with the vascular basal lamina. Several other systems have been developed to study the permeability changes in the vasculature (89, 110, 112-114). Microfluidic collagen gels were fabricated (112, 114) and seeded with ECs to study barrier functions and permeability. Chrobak et al. (112) showed that cells formed a strong barrier in these gels and responded to inflammatory stimuli by rapidly decreasing barrier permeability and increasing leucocyte adhesion. Price et al. (114) demonstrated that low flows were related to higher permeability whereas higher flows promoted a stronger barrier function, while increasing the lifespan of the endothelial constructs *in vitro*. This demonstrates the effects of biophysical parameters such as shear and transmural pressure in mediating barrier functions. Additionally, Lee et al. (113) designed a simple microfluidic device to generate a tubular, perfusable microvessel network. Similarly, Chrobak et al. (112) found that microvascular networks were responsive to inflammatory stimuli such as histamine and TNFα (113). Furthermore, U87MG cancer cells were used to mimic high permeability conditions seen in neoplastic settings. A drug administered *in vivo* – bevacizumab – was able to reinstate permeability and improve barrier functions in agreement with other *in vivo* data (113). A more complex system envisioned by Sato et al. (110) focused on barrier function and the vascular permeability of ECs and lymphatic ECs (LECs). The microfluidic chip (Figure 1.5A) consisted of two channels separated by a porous membrane (Figure 1.5B). LECs (Figure 1.5C) and ECs (Figure 1.5D) were cultured and maintained in different channels. With flows mimicking that of blood and lymphatic vessels, transport across and from EC channel to LEC channel was observed. In accordance to the aforementioned reports, histamine stimulated also the increase in permeability, and the

authors further tested the system with habu snake venom (Figure 1.5E), showing its effect on the barrier function (110). With the development of vascular permeability assays, it is essential to track changes in permeability and other parameters in real-time. Young et al. (89) developed a microfluidic system and technique to measure real-time endothelial permeability by using-laser induced fluorescence. Additional work developed by Li et al. (115) generated a vascular lumen integrated with a nanowire array that was capable of measuring nitric oxide produced by ECs. Such systems could pave the way to the application of different permeability and barrier function assays within ECs.

In addition to a considerable amount of research on vascular networks and fluid flow, some studies incorporate further biophysical hemodynamic parameters (116, 117). Shao et al. (116) generated a microfluidic chip that applied pulsatile and oscillatory shear stress to ECs and Zheng et al. (117) focused on the combined effects of shear and stretch. Together, these works highlight the need to incorporate complex dynamic conditions in order to fully mimic the vascular microenvironment.

There has been an increasing amount of work developed to recreate vascular networks *in vivo*. By combining biomaterials, microfluidics and microarchitectures, we expect to be able to mimic the vascular wall in different settings, modeling disease and ultimately generating better *in vitro* models for drug discovery and development.

1.3 Vascular aging, inflammation and disease

Vascular diseases such as hypertension and atherosclerosis affect more than 972 million people worldwide (Centers for Disease Control and Prevention data). Age is a key factor contributing to the development of several vascular diseases (118, 119). Although numerous studies have investigated them, the role of biomechanics has remained poorly understood, especially in relation to inflammation and other pathology markers. In this section we highlight some of the key aspects involving inflammation in vascular disease and aging.

1.3.1 Inflammation in vascular aging

Hypertension and atherosclerosis are diseases related to vascular aging. Hypertension (120) and atherosclerosis (Ref) are increasingly prevalent in aging population. Importantly, both diseases have a clear link with vascular inflammation (121) (122). Alterations in redox state, expression of pro-inflammatory enzymes and cytokines, NF-KB activation, increased expression of adhesion molecules, and hypoxic markers are biological events that occur during vascular aging and vascular inflammation (123). Aorta tissue samples from aged subjects were found to have enhanced expression of an array of inflammatory cytokines, IL-1B, IL-6, TNFα, and MCP-1 (124). Of these, IL-6 was found to play a crucial role in aging (125). Interestingly, in one study, serum levels of patients with severe pulmonary hypertension showed increased levels of IL-6 and IL-1 (126). Another study demonstrated that hypertensive patients had higher levels of IL-6 compared to normotensive patients, and IL-6 increased in response to administration of angiotensin II (127). In addition, angiotensin II was able to induce activation of vascular smooth muscle cells, with increased levels of IL-6 and activation of NF-KB (128). IL-6 and TNFα, as well as C reactive protein serum plasma levels, correlate with elevated blood pressure, with IL-6 and TNFα shown to be independent predictors of high blood pressure (129). IL-17, a novel pro-inflammatory cytokine, was also found to be implicated in hypertension, with IL-17$^{-/-}$ mice not sustaining hypertension, failing to show increase in superoxide and retaining endothelium-dependent vasodilatory capacity (130). Another study using aged and young mice has demonstrated that IL-18 was an aged-related inflammatory marker of vascular remodeling (131). Most importantly, the inflammatory signatures observed in vascular disease and aging seem to share a common activator: NF-KB. Zampetaki and co-workers have studied the effect of strain in normal smooth muscle cells, and specifically demonstrated a role for NF-KB (132). Firstly, Zampetaki has demonstrated that cell elongation induced expression of IL-6 in a magnitude dependent way, with 7% resulting in the lowest production of IL-6, and 20% the maximum. A time-scale study showed a rapid increase of IL-6 at 2h of stimulation followed

by a slight decrease afterwards. Interestingly, by using two NF-KB inhibitors (PDTC and SN50), Zampetaki was able to show a decrease in IL-6 levels of cells stressed for 8h (132). It was further pinpointed that IL-6 increase was likely due to signaling pathways involving Ras/Rac1/p38 MAPK/NF-KB, and that IL-6 secretion from VSMC to the extracellular spaces in the blood vessel could initiate or aggravate the inflammatory response (132). Multiple lines of evidence establish a connection between inflammation and age-related vascular dysfunction in humans, mediated through NF-KB, and involving oxidative stress and pro-inflammatory cytokines (133, 134).

Multiple studies have also highlighted a role for ROS in the inflammatory state of vascular disease (119, 135-143). Normal aging processes result in increased ROS in the blood vessel, more specifically, increases in superoxide and hydrogen peroxide that can lead to reduced bioavailability of NO and increased in inflammation (137). Superoxide generation from both the mitochondria and NAPDH oxidases have been implicated in age-related changes, and to a smaller extended superoxide derived from xanthine oxidase. Several NAPDH oxidase isoforms have been shown in ROS-derived vascular disease and inflammation, such as NOX1, NOX2 and NOX4 (135, 136, 139-141), and a few studies have also pinpointed a role for mitochondrial superoxide generation (119, 143, 144). For instance, NOX4 modulates the expression of pro-inflammatory genes in aged mice (139). In addition, TGFβ1 appears to induce higher expression of NOX4, thus propagating a chain of events that results in a continuous increase in inflammation (139). Interestingly, a mouse model of chronic inflammation showed increase in superoxide via the mitochondria and NAPDH oxidase, while showing a simultaneous decrease in superoxide dismutase 2 (SOD2) (144). It was found that the interplay between inflammation and ROS could further lead to increased telomere dysfunction and senescence, accelerating the aging process (144). Importantly, all these studies highlight a role for ROS and low grade inflammation in the development of vascular disease and aging (137).

Several strategies are being pursued to combat vascular disease and aging based on the molecular pathways discussed above, further highlighting and validating their importance

in the disease pathology and aging process. Statins have shown tremendous potential (145). Treatment with statins can result in reduction of NF-KB activation and prevent the initiation of disease by reducing the pro-inflammatory cytokines TNFα, IL-6, IL-1, IL-8, IL-12, and by increasing the anti-inflammatory cytokines IL-4 and IL-10 (145). Lonafarnib, a farnesyl-transferase inhibitor, was demonstrated to inhibit cytokine secretion on a mevalonate kinase deficiency model (146). Novel strategies against "inflammaging", such as caloric restriction, have also shown potential to inhibit inflammation in vascular aging. Csiszar and colleagues showed that aged rats were associated with impaired vascular oxidative stress and increased NF-KB activity (147). Interestingly, rats undergoing caloric restriction showed improved endothelial function, attenuated vascular ROS production, inhibited NF-KB activation and downregulation of inflammatory genes. Serum from aged rats induced NF-KB activation and inflammatory gene expression in coronary artery endothelial cells, while serum from caloric restricted rats prevented it (147).

Overall, studies indicate a role for inflammation and ROS in the initiation, development, and progression of vascular disease and aging. There is, however, a strong need for novel *in vitro* models of vascular aging that also take into account the dynamic environment observed in blood vessels.

1.3.1 Hutchinson Gilford Progeria Syndrome: a vascular aging disease

Hutchinson Gilford Progeria Syndrome (HGPS) is a rare and heritable autosomal dominant human syndrome that results in accelerated and premature aging (148). Patient's life expectancy is typically 13 years old, and the disease generally leads to death due to myocardial infarction. Patients exhibit signs of advanced aging, with complications such as bone abnormalities, alopecia, growth impairment, elevated blood pressure, reduced vascular compliance, and hearing loss (148). A point mutation in the lamin A gene activates a cryptic splice donor site (Figure 1.5), producing an abnormal protein—progerin—that accumulates in the cell's nuclei (149-151). Lamins have an important role in regulating the nuclear shape,

stability, and structure (152), which can affect chromatin organization, gene expression, DNA replication, transcription, and aging (153, 154). In HGPS, accumulation of progerin leads to nuclear morphology abnormalities, increased cell senescence, increased reactive oxygen species, DNA damage, among others (153, 155).

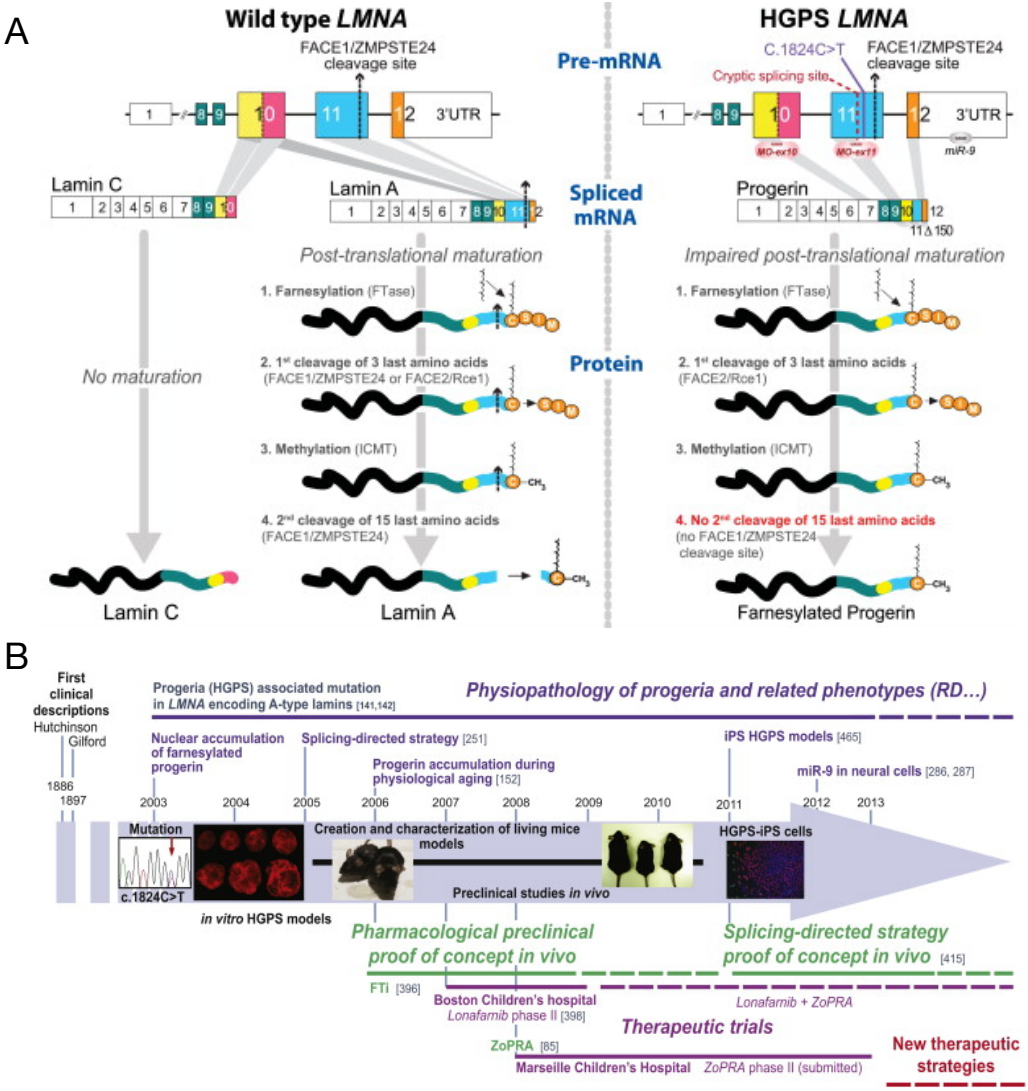

Figure 1.5 – Lamin A processing and timeline of progeria research advances. (A) A point mutation on the lamin A gene impairs downstream post-translational modifications resulting in a mutated protein termed progerin. (B) Timeline of research advances and important hallmarks in the study of HGPS. Adapted from Cau et al.(154)

The most affected tissues in HGPS are load-bearing ones, such as bone, cartilage and cardiovascular (152, 156, 157). Indeed, progerin seems to primarily target vascular cells

(156), and an iPSC model of HGPS reveals the highest levels of progerin accumulation in MSCs, VSMCs and fibroblasts (157). Interestingly, lamin A is known to scale with tissue stiffness (158), and a parallel can be hypothesized for the influence of mechanical stretching. Due to the intimate relation between nuclear mechanical changes during HGPS and the targeting of load-bearing tissues, it is crucial to study the influence of mechanical stretching on disease progression and pathology.

Recently, stem cell technologies have facilitated the generation of disease models, either in static or dynamic conditions (159), with potential applications in personalized medicine. Induced pluripotent stem cells (iPSCs) generated from HGPS fibroblasts (Figure 1.5) have been used to recapitulate aging in an accelerated fashion (160-164). There are several phenotypic similarities between HGPS and vascular aging, namely increased arterial stiffness, decreased VSMC number, increased expression of pro-inflammatory molecules, increased risk of atherosclerosis, increased ECM deposition, increased calcification, and increase in systolic and pulse pressure (165). Due to the similarity of HGPS with physiological aging, HGPS-based models have been proposed as a tool to study vascular aging and thus facilitate the discovery of novel treatments (165). Despite all of the advances in the field, to the extent of our knowledge, there is only one report on the influence of mechanical strain in HGPS. Fibroblasts from HGPS skin exhibit increased nuclear stiffness with cell passage, and also show decreased viability and increased apoptosis under mechanical strain (166).

Similar to inflammatory changes mentioned in the sub-chapter above, two mouse models of accelerated aging have shown increase in pro-inflammatory cytokines. Osorio and co-workers have used two mouse models, Zmpste24$^{-/-}$ and Lmna$^{G609G/G609G}$, and showed in both increased activation of NF-KB (167). The activation was followed by secretion of pro-inflammatory cytokines IL-6, TNFα, and CXCL1. Similar to a previous study (132), inhibition of NF-KB, either pharmacological of genetic, prevented the age-associated events in the mouse models (167).

The combination of patient-derived and disease-specific cells with organs-on-chips technologies could drive forward the understanding of vascular disease and aging. Vascular cells are constantly under dynamic stimulation, which can influence their behavior, especially during disease progression. In particular, these new models can address questions related to the influence of biomechanical (shear stress, strain, trans-endothelial flow, stiffness) and electrical signals in the beginning and development of vascular disease and vascular aging.

1.4. Future challenges and translational opportunities

1.4.1 Need for cardiovascular organ-chip models

CVD is the leading cause of death in the United States (1, 168). Approximately 85.6 million people suffer from a CVD, resulting in 2,150 deaths per day in the US alone and costing annually $320 billion and predicted to continue to rise (1). As a result, there is a need for development of novel drugs either for prevention (169) or treatment of CVD (170). Despite such a demand, the number of new pharmaceutical compounds approved per amount spent on research and development (R&D) has halved approximately every 9 years since 1950 (171). While most of the scientific and technological fields have seen exponential advances, the past 60 years of drug development has not followed that trend (171). However, spending continues to increase, with a reported $40B expenditure in 2014 in pharmaceutical R&D (172). These numbers suggest that there is room for a disruptive technology allowing for a more predictive and efficient drug discovery/development process (10, 173, 174). Such technology would have the potential to lead to the discovery of new and improved drugs to treat CVD, while reducing the current patient-burden.

Some of the key challenges current drug discovery models face have been summarized by Pound and colleagues (175). Most of these fall into one main problematic – positive/negative findings in animals do not necessarily link to positive/negative findings in humans.[73, 74] Below, we have listed some of the shortcomings associated with the current paradigm of drug development, as appeared in the literature:

(1) CVD animal models are poor predictors of human responses (176);

(2) Adverse effects due to systemic toxicity or toxicity of metabolites are organism-dependent (177);

(3) Some drugs can benefit a certain group of ethnicity, sex, age and/or genotype. Such phenomenon is not necessarily captured in a limited clinical trial study. For example, it is known that the average volunteer for clinical trials is a mid-aged, female (178, 179). This does not recapitulate the multitude of possible users of a particular drug;

(4) The current paradigm is lengthy and costly (180).

For all of the reasons mentioned above and others discussed in the literature, the process of drug development in the cardiovascular arena, obtaining regulatory approval and its introduction to the market is becoming less efficient and costlier. In fact, industry faces an increasing FDA regulatory scrutiny[9], while less drugs are being allowed to the market. However, this is not unfounded: regulatory agencies are requiring more evidence of safety to avoid post-market issues, since clinical trials do not offer a complete measure of protection (181, 182). Together, the above-described reasons highlight the role of new models to better predict safety in humans.

Some researchers underscore that inefficiency in the drug discovery pipeline could perhaps be attributed to current cardiovascular models. In fact, these models are not entirely capable of mimicking human conditions and dynamics. For example, in a recent study, a survey showed industries were interested in adopting safety practices with human tissue-based approaches, despite the fact that they were not widespread (Figure 1.6A) (173). Interestingly, costs were not seen as a major issue towards adopting such models, whilst 50% reasoned that human models were more relevant (173). A study analyzing AstraZeneca's drug pipeline from 2005-2010 showed that 82% of drug project closures in the preclinical phase was due to safety issues.

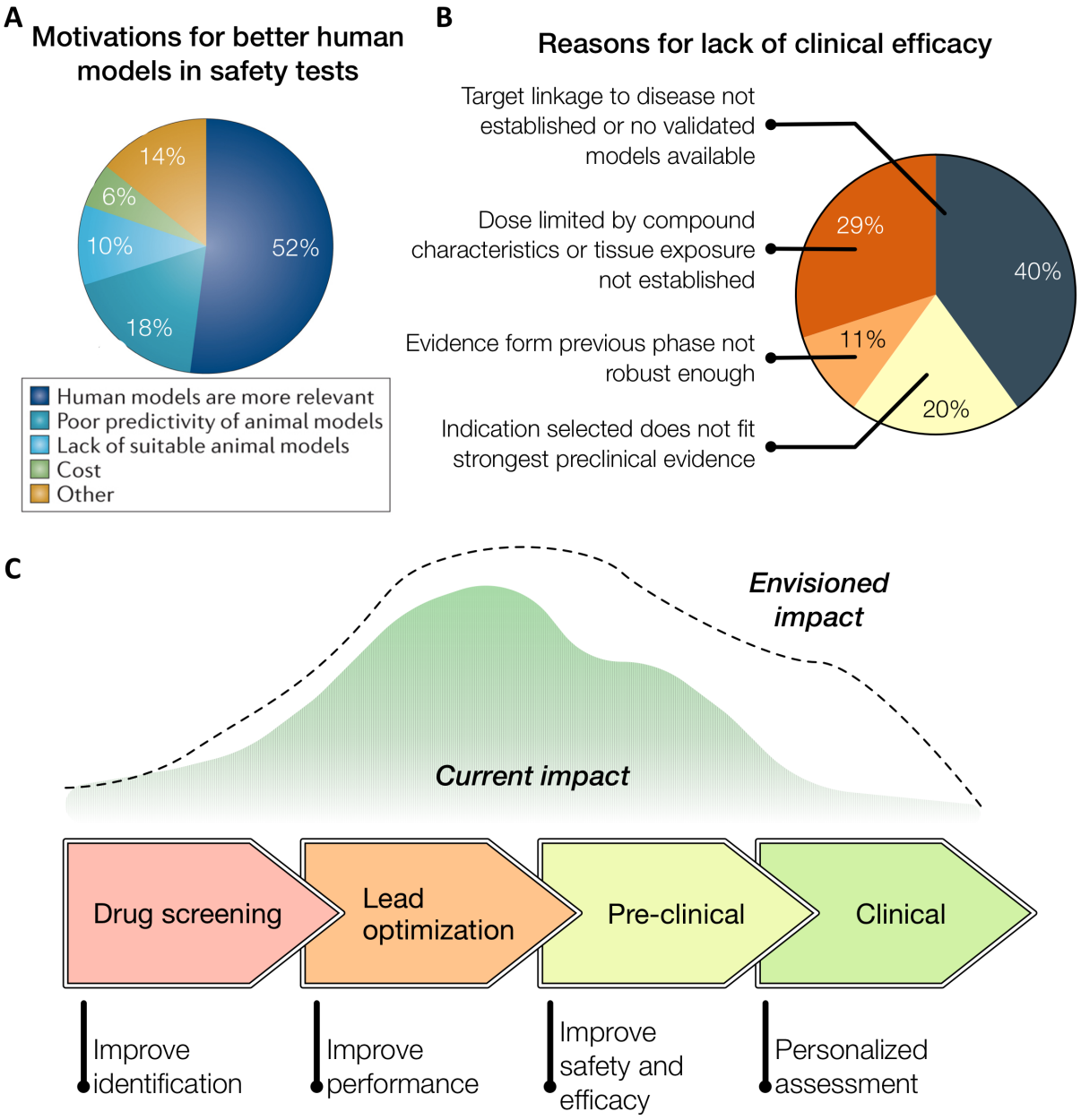

Figure 1.6 – (A) Survey on the motivations behind adopting human tissue-based approaches for safety pharmacology studies (173); (B) AstraZeneca's small-molecule projects from 2005 to 2010, the terminated projects were analyzed to understand the causes for failure and identify potential predictors of success (total of 28 projects) (10); (C) Impact of organs-on-a-chip technologies on the drug development pipeline. [(A) adapted from Jones *et al.*(173); (B) adapted from Pangalos *et al.* (10)]

Interestingly, among the organ systems involved in the safety failures, the cardiovascular one accounted for as much as 17% failures, the highest of all the organ systems analyzed. The solution could be the introduction of a paradigm shift using a disruptive technology that presents a physiologically relevant *in vitro* model of the human cardiovascular system (183). In contrast to preclinical stages, the project closures in clinical phase are mainly due to

efficacy issues. Remarkably, in 40% of the cases of lack of clinical efficacy (Figure 1.6B), the reason is due to no target linkage to disease or no validated models available, while other aspects are related to results not fitting preclinical evidence.

Organs-on-a-chip platforms gained wide scientific attention due to their potential in achieving a physiological resemblance *in vitro*, with a hope to potentially change the way scientists and industry can test the effect of drugs on human cells and organs. Indeed, pioneering work has been done to mimic cardiovascular tissue *in vitro* (184-186). These organs-on-a-chip platforms have thus far been able to make interesting additional *in vitro* models. However, to date, it is still difficult to claim that the associated studies have created examples easily adaptable by industry, as means toward cost-effective development of new drugs that would not have been possible otherwise. In order to maximize the impact, the technology has to provide a unique advantage over current technologies/models. Even though such models have produced exciting scientific studies, there has not been a major reception for them by the industry. Such adaption may be a matter of time, while scalability and simplicity over current methodologies is tackled.

The needs of the industry can broadly be divided in a need for better *in vitro* models predicting the behavior of animal and human organs (ex: heart), and human organ systems (ex: heart-vascular interactions). While actual proof of clinical predictability is necessary to make an impact and engage with regulatory agencies, scientific studies to date have demonstrated that their platforms could indeed perform a screen. In the path towards achieving broad application by the pharmaceutical industry are two key challenges: guaranteeing clinical relevancy and, importantly, reproducibility.

1.4.2 Translating cardiovascular organ-chip models

Once the advantages over current technologies/models are proven, the following step is to have a commercialization strategy. Aside from the academic examples mentioned above, it is also worthwhile considering some of the ventures established towards commercializing and implementing the associated technologies. There are a number of

enterprises aiming at commercializing products that encompasses single and multiple organs-on-a-chip. These companies have mainly developed products for research laboratories, but ongoing efforts are being made to apply such technologies at a broader scale in the pharmaceutical industry.

Market reception from pharmaceutical industry is expected to be high, mainly due to the ever-decreasing number of new drug approvals and the challenges faced with preclinical models. However, these *in vitro* platforms would require regulatory approval for cardiovascular applications, either for heart- and vasculature-on-a-chip systems alone, or for a potential combination of both. An opportunity in this arena is to show comparable results to animal tests, followed by a strong demonstration of reproducibility and statistical significance. Another path for application of cardiovascular organs-on-a-chip could be direct regulatory endorsement. The current platforms required by FDA for such assessments have remained limited to petri dish, animal studies and limited clinical trials – models still lacking the level of accuracy and predictability desired. Here, the dialogue with regulatory agencies such as FDA would be a starting point, in order to establish standards expected for such platforms from the regulatory point-of-view.

Some of the open challenges research teams and companies are tackling are related to standardization, optimization, and scaling up for manufacturing (discussed in detail by Kobayashi et al. (187)). While the scientific community is geared towards innovating and creating new platforms, the growth of companies in this area could lead to their optimization for standardization, reproducibility and scaling-up. This key challenges, once tackled, will allow the wide-spread usage of cardiovascular organ-on-a-chip for drug discovery, while securing regulatory endorsement. The impact of such technologies for drug discovery and development is vast (Figure 1.6C). Current opportunities exist for improving performance at later stages of lead optimization, and safety and efficacy at early stages of preclinical studies. We envision the impact of such technologies to increase at an early future for preclinical stages, and later one for personalized medicine approaches in the clinical fields.

CHAPTER II

AIMS

CHAPTER II – Aims

This thesis begins by generating a novel blood vessel-on-a-chip supported by the need for vascular models of aging and disease that take into account the effects of biomechanical stimulation. The lack of *in vitro* microphysiologic systems that meet this need motivated the work developed here. During the generation of the blood vessel-on-a-chip, two more needs were identified, (1) ways to monitor and sense directly organs-on-a-chip and (2) ways to precisely control organs-on-a-chip in a wide range of experimental conditions. These motivated the creation of a mini-microscope and different sensing modalities to pair with organ-on-a-chip devices, and the creation of an actuator platform operated remotely to allow control of such devices. Accordingly, the thesis experimental work was divided into chapters consisting of making the blood vessel-on-a-chip, monitoring through imaging, and controlling through software/hardware.

The goals of each chapter are:

- **Chapter 1** overviews the landscape of cardiovascular organs-on-a-chip and reflects on challenges and applications in different stages of the drug development pipeline. It focuses particularly on biomechanical forces actuating in blood vessels, and progeria as a model for vascular aging.
- **Chapter 2** (current chapter) lays out the key goals of the thesis and each chapter.
- **Chapter 3** builds on the need for new vascular aging and disease models, and presents experimental data on the generation of a blood vessel-on-a-chip system to evaluate the responses to normal and pathological levels of strain in healthy and progeria-derived SMCs.
- **Chapter 4** builds on the need for new sensing tools to combine and take advantage of organs-on-a-chip, and presents experimental data on the generation of an imaging tool to monitor organs-on-a-chip, via brightfield or fluorescence analysis with different sensing modalities.

- **Chapter 5** builds on the need for new tools to control organ-on-a-chip devices in a range of experimental conditions, and presents experimental data on the generation of a control system that integrates microfluidic valving and sensing in microfluidics through software and hardware.
- **Chapter 6** builds on the collective experimental results, and discusses the relevance and key points of the thesis and directs future work based on standing questions and new avenues of research opened by this thesis.

CHAPTER III

BLOOD VESSEL- AND PROGERIA-ON-A-CHIP MODEL

Adapted from João Ribas, et al., and Lino Ferreira and Ali Khademhosseini, “Biomechanical Strain Exacerbates Inflammation on a Progeria-on-a-Chip Model”, Small, 13: 1603737 (2017).

Ribas devised the concept, performed experiments, and wrote the paper. Mario Miscuglio helped with simulations. iPS cells were provided by Patrícia Pitrez.

CHAPTER III – Blood vessel- and progeria-on-a-chip platforms

3.1. Introduction

The naturally occurring biomechanical strains in blood vessels translate via mechanotransduction into behavioral changes of vascular smooth muscles (SMCs) and endothelial cells (ECs). Whereas ECs are primarily exposed to fluid shear stress, SMCs are mainly exposed to cyclic biomechanical strain, which plays a key role in controlling the tone of the vessel and concomitant blood pressure (188). In a healthy arterial wall, SMCs experience cyclic biomechanical strain of 9% (189), while SMCs under pathological conditions experience strains of up to approximately 15% (190). *In vitro*, several studies conducted have utilized uniaxial strain values in the order of 5-25% (191). These studies revealed that cyclical biomechanical strain in SMCs is transduced by integrins (192) and results in the acquisition of a contractile phenotype reminiscent of the *in vivo* phenotype (191, 193, 194). Pathologic levels of biomechanical strain can increase reactive oxygen species (ROS) levels as well as induce expression of vascular injury and inflammation markers (191, 195). Accumulated levels of such markers are hallmarks of vascular disease and progressively increase during aging (125, 196), leading to further worsening of pathology.

Currently there is no dedicated *in vitro* microfluidic system with SMCs to study the impact of biomechanics in aging and vascular diseases such as hypertension. In the past few years, the lack of appropriate *in vitro* models has motivated the need for the development of microfluidic organ-on-a-chip models (197-199) that are able to recapitulate the complex *in vivo* biological parameters. Integration with microfluidic devices makes these platforms uniquely suited to apply physiologically relevant biomechanical strain, shear stress, transmural pressure, and/or provide three-dimensional (3D) environments. To date, some microfluidic models have been developed to apply biomechanical strain mimicking the lung (200-202), gut (203-205), and blood vessels (206-210), but have not been applied in the context of human vascular aging.

Recently, stem cell technologies have facilitated the generation of aged cells (157). Hutchinson-Gilford progeria syndrome (HGPS) is a rare genetic disorder caused by a mutant

form of the nuclear protein lamin A – progerin (149, 150). HGPS patients suffer from premature and accelerated aging (148, 157, 161, 162, 211), while accumulation of progerin also occurs during physiological aging. Notably, HGPS targets primarily vascular cells (156), which are mechanically active tissues. Induced pluripotent stem cells (iPSCs) generated from HGPS fibroblasts have been used to recapitulate normal aging in an accelerated fashion (160-164), proving to be a valuable tool to study vascular aging and thus facilitate the discovery of novel treatments (165, 212). However, accurate *in vitro* models must take into account the interplay between biomechanical strain and the behavior of aged cells.

Here, we set out to develop a novel progeria-on-a-chip model that would capture blood vessel biomechanical dynamics on-chip. Within this device, we exposed healthy iPS-SMCs and HGPS iPS-SMCs to normal and pathological strains to study the interplay between biomechanical strain and vascular aging. Models that combine biomechanics and vascular aging are crucial tools towards understanding vascular disease/aging and developing new therapies.

3.2 Materials and Methods

3.2.1 Device fabrication

The microfluidic device was made with PDMS (Sylgard, Dow Corning) at a ratio of 10:1 (w/w) monomer to curing agent. Hard molds of the device were custom-made by laser cutting (VersaLaser) 800-µm polyoxymethylene (DuPont) sheets and glued to the bottom of petri dishes. PDMS was cast onto the molds and cured for 24 hours at 80 ºC (Figure 3.1). PDMS membranes were produced by spin-coating PDMS 20:1 (w/w) on silanized silicon wafers at 950 rpm for 20 seconds, and cured at 80 ºC for 24 hours. The bottom layer PDMS slab was bonded to the PDMS membrane with oxygen plasma (Plasma Etch PE-25), and the resulting set was peeled from the wafer. The top PDMS slab was then bonded to the set of bottom-membrane with oxygen plasma and aligned manually under a microscope. The surface of the fluidic channel was treated with fibronectin (Sigma-Aldrich) at a concentration of 50 µg mL^{-1} to allow for cell attachment.

3.2.2 Computational simulation

Computational finite-element models were developed using COMSOL® to simulate the experimental results and to represent the mechanical deformation and allow for stress analysis of the PDMS membrane. The device structure was modeled as two PDMS flexible bodies sandwiching a flexible PDMS membrane with a thickness of 100μm. The Young's Moduli used were 2.5 MPa for the flexible bodies and 500 kPa for the membrane respectively, as determined from mechanical characterization by Instron® tensile mechanical measurements. The Poisson's ratio used for both PDMS compositions was 0.49 (213). The interfaces between the different PDMS layers were modeled as a bonded contact. The base of the model was constrained as fixed and a linearly increasing pressure increase, to a value of 0, 10, 20, 30, or 50 kPa, was applied to the top surface of the PDMS membrane. The simulation took into account the presence of SMCs, which were uniformly distributed along the top surface of the PDMS membrane. The interfaces between the cells and the PDMS membrane were modeled as bonded contact. The cells were shaped according to a morphological evaluation of *in vitro* studies through confocal imaging (214). For the cells, literature values for the Elastic modulus (100 kPa) and the Poisson's ratio (0.49) were used (215). The strains generated on the top surface of the membrane, as well as on the cells attached to the membrane surface, were analyzed.

3.2.3 Mechanical stimulation

Cells were stimulated for 24 hours with different percentages of cyclic strain. To ensure media exchange, the fluidic channel was perfused with cell culture media at a flow rate of 100 μL $hour^{-1}$. To stimulate the cells, the vacuum inlet of the microfluidic pump was connected to a computer-controlled solenoid system and stimulated at a frequency of 0.5Hz. The vacuum pressure was adjusted with a pressure regulator and used in the range of 0 kPa (=0% strain), 10 kPa (=9% strain), and 20 kPa (=16% strain).

3.2.4 Cell culture

Aortic SMCs (Lonza) were grown in Smooth Muscle Growth Media-2 BulletKit (SmGM-2; Lonza) at 37 ºC and 5% CO_2 in a humidified incubator. Cells were trypsinized from cell culture flasks and seeded in the microfluidic channels at a density of 1.6 million cells mL^{-1}. Prior to the start of strain experiments, cells were maintained in media containing DMEM/F12 1:1 mixture (Thermo Fisher Scientific) supplemented with Insulin-Transferrin-Selenium (ITS; Thermo Fisher Scientific) (216). iPS generated from healthy and HGPS donors were kindly provided by Xavier Nissan and previously characterized (164). Differentiation was performed according to a previously described protocol (217). At the end, 95% of both differentiated cells express a-SMA, SMMHC and calponin proteins. Moreover, HGPS-iPSC SMCs express progerin protein (15% of the cells). Healthy and HGPS iPS-derived SMCs were grown in SmGM-2 media at 37 ºC and 5% CO_2 in a humidified incubator. Due to the smaller size, iPS-SMCs were seeded in the microfluidic device at a density of 3.2 million cells mL^{-1}, which yielded a cell confluence that was identical to those used for the SMCs. Treatment with 10μM lovastatin (Sigma-Aldrich) was administered 2 hours before the start of mechanical stimulation and continued through the 24 hours of cyclic strain. Treatment with 2μM lonafarnib (Sigma-Aldrich) was administered together with mechanical stimulation and continued through the 24 hours of cyclic strain.

3.2.5 Gene expression

Cells were trypsinized from the microfluidic devices 24 hours after mechanical stimulation. RNA was extracted using an RNeasy Micro kit (Qiagen). cDNA was synthesized from a total of 500 ng of RNA using the QuantiTec Reverse Transcription kit (Qiagen) following the manufacturer's protocol. qRT-PCR was performed in an iQ5 thermocylcer using SYBR green probe (Biorad). Gene expressions were normalized using housekeeping *GAPDH*. All used primer sequences are listed in **Table 3.1**. Results follow the $2^{-\Delta\Delta Ct}$ method and are reported as fold change as compared with the no strain (0%) control, unless otherwise indicated.

Table 3.1. Primer sequences used for qRT-PCR.

Primer	Sequence
SOD1 Fw	5'–GAGCAGAAGGAAAGTAAT–3
SOD1 Rv	5'–GATTAAAGTGAGGACCTC–3
SOD2 Fw	5'–CTGGAACCTCACATCAAC–3'
SOD2 Rv	5'–CTGTAACATCTCCCTTGG–3'
p22phox Fw	5'–AAGTACATGACCGCCGTG–3'
p22phox Rv	5'–CACCGAGAGCAGGAGATG–3'
CAV1 Fw	5'–TAGACTCGGAGGGACATCTC–3'
CAV1 Rv	5'–TACACTTGCTTCTCGCTCAG–3'
IL6 Fw	5'–CACTCACCTCTTCAGAACGAAT–3'
IL6 Rv	5'–GCAAGTCTCCTCATTGAATCCA–3'
IL1B Fw	5'–AACAGATGAAGTGCTCCTT–3'
IL1B Rv	5'–CTTGCTGTAGTGGTGGTC–3'
JUN Fw	5'–GAGACTGTAGATTGCTTCTGTAG–3'
JUN Rv	5'–CTCACAAACCTCCCTCCT–3'
TAGLN Fw	5'–TTCCTTCGTTACTACTGCTGAG–3'
TAGLN Rv	5'–AGGCAACTCGTAACTCTTCTC–3'
ITGB1 Fw	5'–GGCTTAATTTGTGGAGGAAATGGT–3'
ITGB1 Rv	5'–TGTCCGTTGCTGGCTTCA–3'
GAPDH Fw	5'–ACAGTTGCCATGTAGACC–3'
GAPDH Rv	5'–TTTTTGGTTGAGCACAGG–3'

3.2.6 Immunocytochemistry

Cells were immediately fixed in 4% paraformaldehyde (Sigma-Aldrich) for 15 minutes at room temperature. Cells were then permeabilized with 1% (v/v) Triton X-100 (Sigma-Aldrich)

for 10 minutes, followed by blocking with 1% bovine albumin serum (Sigma Aldrich) for 45 minutes at room temperature. Primary antibody against lamin A/C (Santa Cruz, sc-20681; 1:50; reacts against both lamin A/C and progerin) was incubated at room temperature for 1 hour. Primary antibody against the phosphor-histone H2A.X (Cell Signaling Technology, 9718, 1:400) was incubated overnight at 4ºC. The channels were washed with phosphate buffer saline (PBS; Thermo Fisher Scientific) five times and solutions of fluorescently labeled secondary antibodies were introduced (Alexa 546 anti-mouse, Thermo Fisher Scientific; Alexa 594 anti-rabbit, Thermo Fisher Scientific). Secondary antibodies were incubated for 1 hour and nuclei counterstained with DAPI (Thermo Fisher Scientific) for 5 minutes. F-actin staining was achieved by incubating cells with Alexa 488 phalloidin solution according to manufacturer's protocol. Images were acquired with a Zeiss Observer D1 microscope.

3.2.7 Cell senescence

Senescent cells (*n* = 3 experiments) were detected through histochemical staining of β-galactosidase (Senescence Cells Histochemical Staining Kit, Sigma-Aldrich) according to the manufacturer's protocol. Briefly, after 5 days of cyclic mechanical stimulation, cells were washed with PBS and fixed with 1X fixation buffer for 7 min at room temperature. The staining 5-bromo-4-chloro-3-indolyl-β-D-galactopyranoside (X-Gal) solution was prepared accordingly and the cells were incubated for 24 hours at 37 ºC. Stained cells were washed in PBS and imaged on an inverted brightfield microscope.

3.2.8 Image quantification

Cell orientation, length and width were determined from *n* = 3 experiments of f-actin stained cells. Three microscopic images for each *n* were analyzed in ImageJ to determine angle of orientation, length, and width. Nuclei images obtained after computer simulations were used to determine the vector displacement maps upon strain, using the Particle Image Velocimetry (PIV) plugin of ImageJ.

3.2.9 Statistical analysis

Results are presented as mean ± standard deviation (SD) unless otherwise indicated. Group data analysis was performed with one-way ANOVA and a Tukey's post hoc test against control group. Comparison between two groups was performed using a *student t* test.

3.2.10 Vacuum controller

A custom made vacuum controller (Fig. M3.1) was built using a microcontroller (Teensy 2.1). The controller was programmed in Arduino (see *subchapter 3.2.11*), and controlled the on/off of a solenoid valve (The Lee Co.) Briefly, a circuit was engineered connecting the microcontroller to a small screen (128x32 OLED display, Adafruit), the solenoid valve and pushup buttons to control the cyclic frequency. The controller was able to operate continuously at room temperature, applying cyclic strain to the microfluidic device.

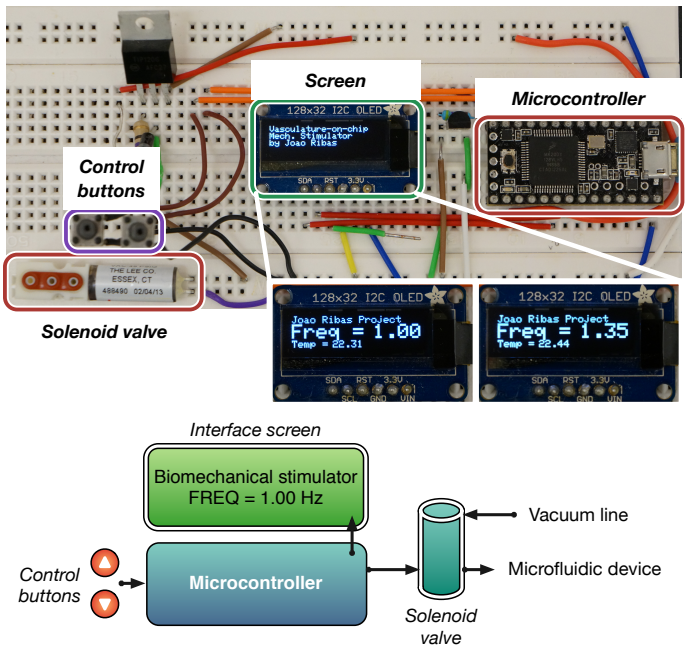

Figure M3.1. Device to control the cyclic strain applied to cells a microfluidic device. The device consists of a microcontroller programmed to turn on/off a solenoid valve. The valve is connected to a vacuum source and the user can control the frequency of cyclic strain via the user interface.

3.2.11 Controller code

```
/************************************************************************
      _  ____          ____    _____  _____ ____        _____
     | |/ __ \   /\   / __ \  |  __ \|_   _|  _ \   /\    / ____|
     | | |  | | /  \ | |  | | | |__) | | | | |_) | /  \  | (___
 _   | | |  | |/ /\ \| |  | | |  _  /  | | |  _ < / /\ \  \___ \
| |__| | |__| / ____ \ |__| | | | \ \ _| |_| |_) / ____ \ ____) |
 \____/ \____/_/    \_\____/  |_|  \_\_____|____/_/    \_\_____/

  Vasculature-on-a-chip Project (C) Joao Ribas January 2014
  Mechanical stimulator and temperature sensor with pushup buttons
  Libraries:
  OneWire for Temperature Sensor
  Adafruit_SSD1306 for OLED 128x32 I2C

************************************************************************/
//OLED screen
#include <Wire.h>
#include <Adafruit_GFX.h>
#include <Adafruit_SSD1306.h>

//temp sensor
#include <OneWire.h>
#include <DallasTemperature.h>

// OLED Screen
#define OLED_RESET 4
Adafruit_SSD1306 display(OLED_RESET);

#define NUMFLAKES 10
#define XPOS 0
#define YPOS 1
#define DELTAY 2

#define LOGO16_GLCD_HEIGHT 16
#define LOGO16_GLCD_WIDTH  16
static unsigned char PROGMEM logo16_glcd_bmp[] =
{ B00000000, B11000000,
  B00000001, B11000000,
  B00000001, B11000000,
  B00000011, B11100000,
  B11110011, B11100000,
  B11111110, B11111000,
  B01111110, B11111111,
  B00110011, B10011111,
  B00011111, B11111100,
  B00001101, B01110000,
  B00011011, B10100000,
  B00111111, B11100000,
  B00111111, B11110000,
  B01111100, B11110000,
  B01110000, B01110000,
  B00000000, B00110000 };

#if (SSD1306_LCDHEIGHT != 32)
#error("Height incorrect, please fix Adafruit_SSD1306.h!");
#endif

// temperature sensor
#define ONE_WIRE_BUS 10
```

```
#define TEMPERATURE_PRECISION 12
OneWire oneWire(ONE_WIRE_BUS);
DallasTemperature sensors(&oneWire);
float celsius;

// solenoid control buttons
const int upbutton = 5;
const int downbutton = 6;
const int outputsolenoid = 14;

int outputstate = LOW;
long previousMillis = 0;
long interval = 1000; //time to turn on/off solenoid
int freqinterval = 0.5; //defines freq intervals up or down
float freq;

void setup()   {
Serial.begin(9600); //debuger

sensors.begin(); //temp sensor

//solenioid pins mode:
pinMode(upbutton, INPUT_PULLUP);
pinMode(downbutton, INPUT_PULLUP);
pinMode(outputsolenoid, OUTPUT);
float freq = 1.0;
//end

  // by default, we'll generate the high voltage from the 3.3v line
internally! (neat!)
  display.begin(SSD1306_SWITCHCAPVCC, 0x3C);  // initialize with the I2C
addr 0x3C (for the 128x32)
  // init done
  display.display();
  display.clearDisplay();   // clears the screen and buffer

  // text display tests
  display.setTextSize(1);
  display.setTextColor(WHITE);
  display.setCursor(0,0);
  display.println("Vasculature-on-chip");
  display.println("Mech. Stimulator");
  //display.setTextColor(BLACK, WHITE); // 'inverted' text
  //display.println(3.141592);
  display.setTextSize(1);
  display.setTextColor(WHITE);
  display.print("by Joao Ribas");
  display.display();
  delay(5000);
}

void loop() {
  //getting temperatures
  sensors.requestTemperatures(); // Send the command to get temperatures
  celsius = sensors.getTempCByIndex(0);

  // display setup
  display.setTextColor(WHITE);
  display.setCursor(0,0);
  display.clearDisplay();
  display.setTextSize(1);
```

```
  display.println("Joao Ribas Project");
  display.setTextSize(2);
  display.println("Freq = ");
  display.setCursor(80,8);
  display.println(freq); // prints current frequency
  display.setTextSize(1);
  display.setCursor(0,24);
  display.println("Temp = "); // prints current temperature
  display.setCursor(40,24);
  display.println(celsius);
  display.display();
  delay(10);

// PUSHBUTTONS defining up/down actions
if(digitalRead(upbutton) == LOW ) {
  freq = freq + freqinterval;
  interval = 1 / freq;
  if(freq > 4)
  freq = 4;
// interval = interval + freqinterval; // msec
// freq = 1.0/(interval/1000.0); // in hertz
delay(50);
}
if(digitalRead(downbutton) == LOW) {
  freq = freq - freqinterval;
  interval = 1 / freq;
  if(freq < 0.5)
  freq = 0.5;
// interval = interval - freqinterval;
// freq = 1.0/(interval/1000.0);
delay(50);
// if(interval < 0)
// interval = 0;
}
// OUTPUT SOLENOID CONTROLLER
  unsigned long currentMillis = millis();
  Serial.println(previousMillis);

  if(currentMillis - previousMillis > interval) {
    // save the last time you blinked the LED
    previousMillis = currentMillis;

    // if the LED is off turn it on and vice-versa:
    if (outputstate == LOW)
      outputstate = HIGH;
    else
      outputstate = LOW;

    // set the LED with the ledState of the variable:
    digitalWrite(outputsolenoid, outputstate);
  }
}
```

3.3 Results

3.3.1 Recapitulating blood vessel dynamics on-chip

Blood vessels are constantly exposed to cyclic mechanical stretch (Figure 3.1A) varying from the normal 9% relative strain in healthy individuals (189) to the pathological

15% relative strain (190). Studies conducted in vitro used values in the order of 5-25% (191), with the range of 5-10% considering physiological and >15% pathological strain. To recapitulate the cyclic mechanical deformation experienced by SMCs in the arterial wall of blood vessels we have developed a novel microfluidic polydimethylsiloxane (PDMS) device (Figure 3.1B-E; medium-through version Fig. S3.1). The device consists of a top fluidic channel with an underlying vacuum channel that is separated by a 123.5 ± 3.0 μm PDMS membrane (Figure 3.1B; Figure 3.2). The fabrication process is simple (Figure 3.1C-D) and relies on the creation of a three-layer device, the top fluidic channel, a middle thin PDMS membrane and a bottom vacuum channel. Cells are cultured on top of the membrane (Figure 3.1F), which is deformed by applying different pressure drops on the bottom channel. Previous approaches used pressure drops on side channels to stretch a membrane over a central post (208, 218, 219), or positive pressure to bulge a membrane (220, 221). The device measures 40 mm by 18 mm (Figure 3.1E), is optically transparent, and fits a standard glass slide for easy microscopic visualization. The fluidic channel has a straight region measuring 25 mm by 1 mm. To facilitate channel alignment during assembly of the PDMS layers, the bottom layer was made 0.2 mm wider. The device was designed to be usable in any laboratory setting: pressure drops used are obtained from a laboratory vacuum line, and cell seeding onto the device can be achieved by manually pipetting a cell suspension inside the fluidic channel. We have used this novel device to characterize the vascular response of healthy and HGPS iPS-SMCs to different levels of biomechanical strain (Figure 3.1G).

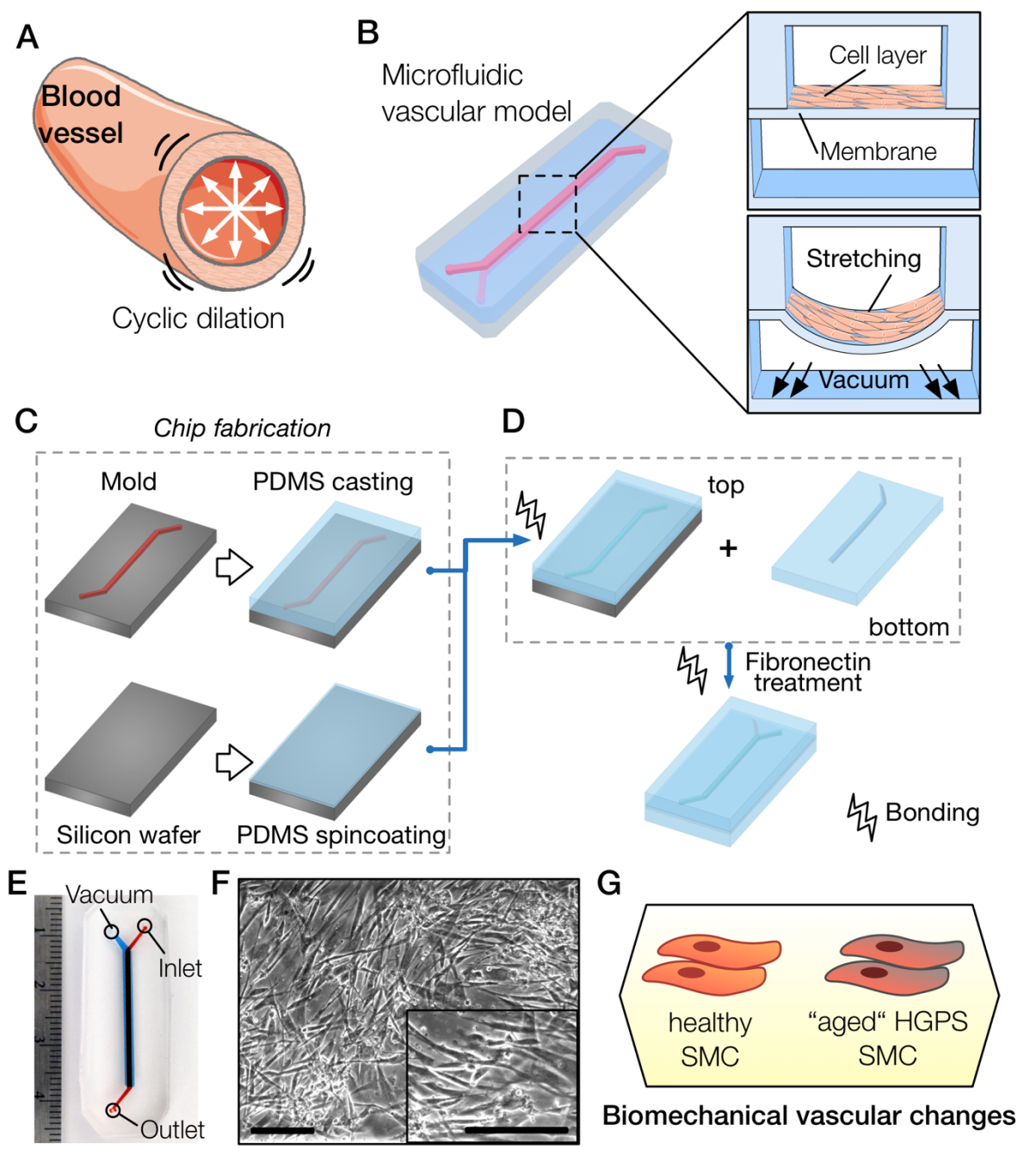

Figure 3.1 – Recapitulation of blood vessel dynamics on chip. (A) Blood vessels experience cyclic strain due to the pulsatile nature of blood flow. (B) Biomimetic microfluidic vascular model containing two overlapping channels. A cross-sectional view of the microfluidic device shows the cell layer cultured on top of the PDMS membrane and a view during vacuum stimulation shows the downward membrane deformation. (C) The first step of the chip fabrication containing the casting of PDMS (10:1 ratio) on an acetal resin mold and the spin coating of PDMS (20:1 ratio) to generate a thin membrane on top of a silicon wafer. (D) The top slab and membrane portions of the PDMS device are bonded using oxygen plasma and then peeled off the silicon wafer. The top part is then bonded to the bottom PDMS slab molded previously, and treated with fibronectin solution to allow cell culture. (E) Photograph of the microfluidic channel showing the media inlet, outlet and the vacuum port. (F) Micrographs of SMCs cultured in the microfluidic chip (scale bar represents 250μm). (G) Proposed

methodology to unveil strain-related vascular changes in iPS-derived SMCs from healthy and HGPS donors.

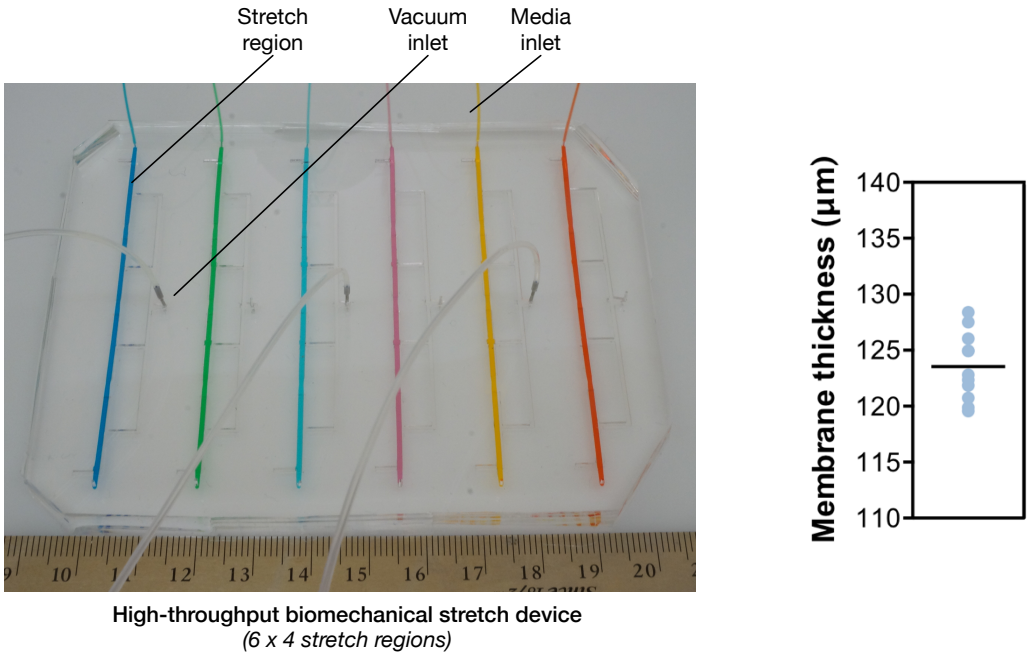

Figure 3.2. Prototype device of a scaled up high-throughput microfluidic device and PDMS membrane thickness. Left - Each color represents a different channel containing 4 vacuum actuation regions. Pressure drops can be applied through vacuum inlets, controlling each 4 vacuum regions; Right - Thickness of the spin coated PDMS membrane (*n*=12).

To characterize the device, we determined the membrane deformation in situ and in silico. Cross-sectional views of the microfluidic device under different amounts of vacuum pressure ranging from 0 kPa to 50 kPa demonstrated a pressure-dependent increase in membrane deformation (Figure 3.3A). The approach used to show in situ membrane deformation has not been demonstrated before and allows immediate and direct visualization of membrane deformation. The thickness and mechanical properties of the device's membrane were tailored to function under low pressures while achieving the required strains. A pressure drop of 10 kPa was found to average to 9 ± 2% strain, 20 kPa to 16 ± 1%, and 30 kPa to 24 ± 2 % (Figure 3.3B). In silico modeling of the membrane deformation demonstrated similar results in the range of 0 kPa to 30 kPa (Figure 3.4). Indeed, a strong correlation was found between cross-sectional measurements and simulation data (Figure 3.3B; Pearson's correlation of r = 0.9825). Moreover, we mapped the variability in mechanical strain by

characterizing the surface strain (Figure 3.4). Additionally, we have simulated the effect of this spatial strain distribution on cells attached to the membrane using micrographs of nuclei within our devices (Figure 3.3C). In line with our modeling, we observed a gradient strain similar to other reports for microfluidic strain devices (200). Importantly, we have also verified that the strain applied was mostly uniaxial (Figure 3.3D). We used the average strain values and analyzed the entire cell population inside the microfluidic device.

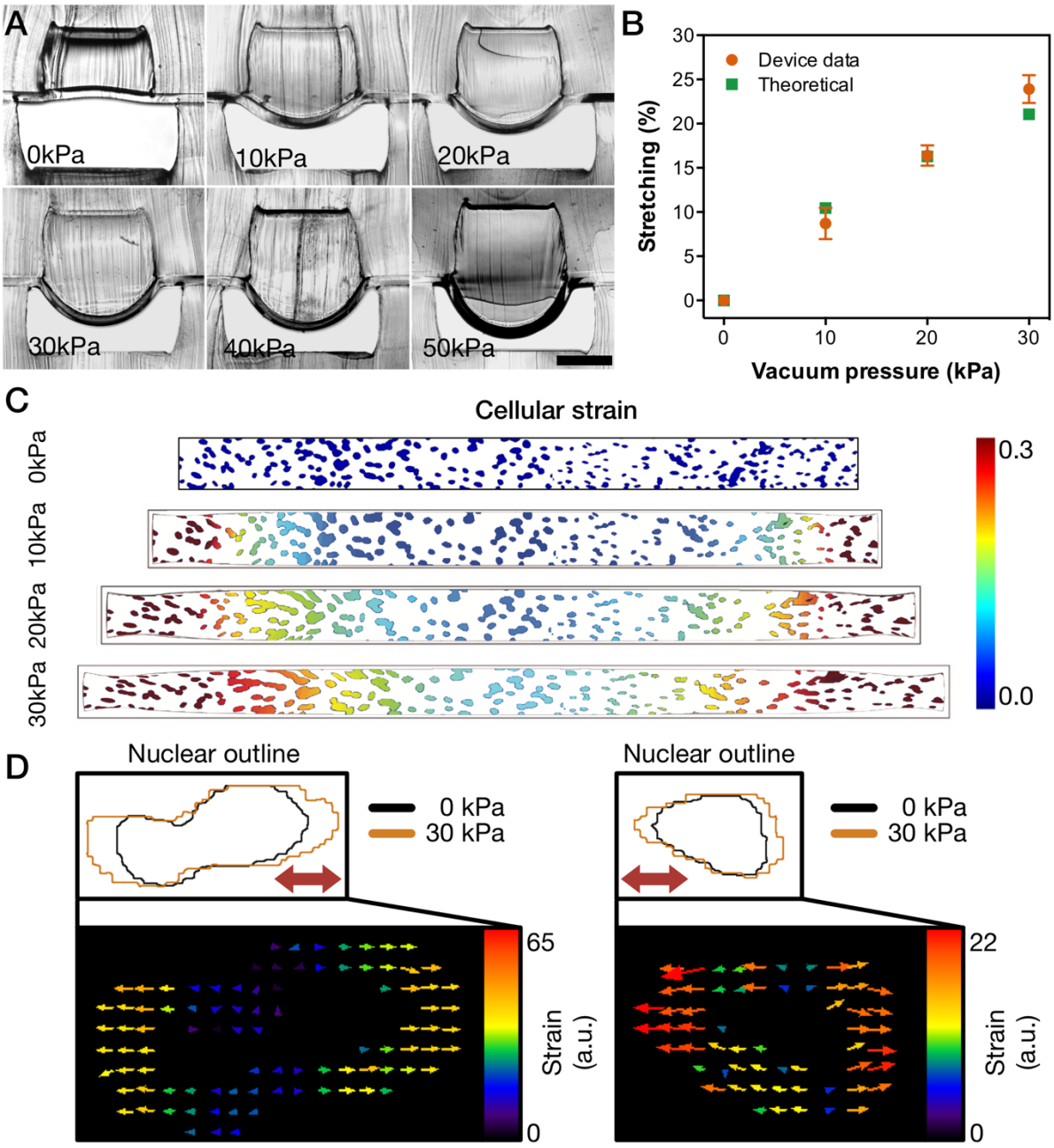

Figure 3.3 – Characterization of stretch capabilities of microfluidic device. (A) Cross-sectional view of microfluidic device and membrane deformation under different amounts of pressure drop

(scale bar represents 500 μm). (B) Comparison of the overall strain on the y-axis between cross-sectional measurements and theoretical computational simulation (results represent mean ± SD of *n*=5). (C) Computational simulation of the strain on a 1 mm x 0.1mm membrane section overlaid with a representative nuclei image under different levels of pressure drop. (D) Two representative nuclear outlines of cells under 0 kPa and 30 kPa and respective vector displacement maps (thick red arrows in the top panels indicate strain direction).

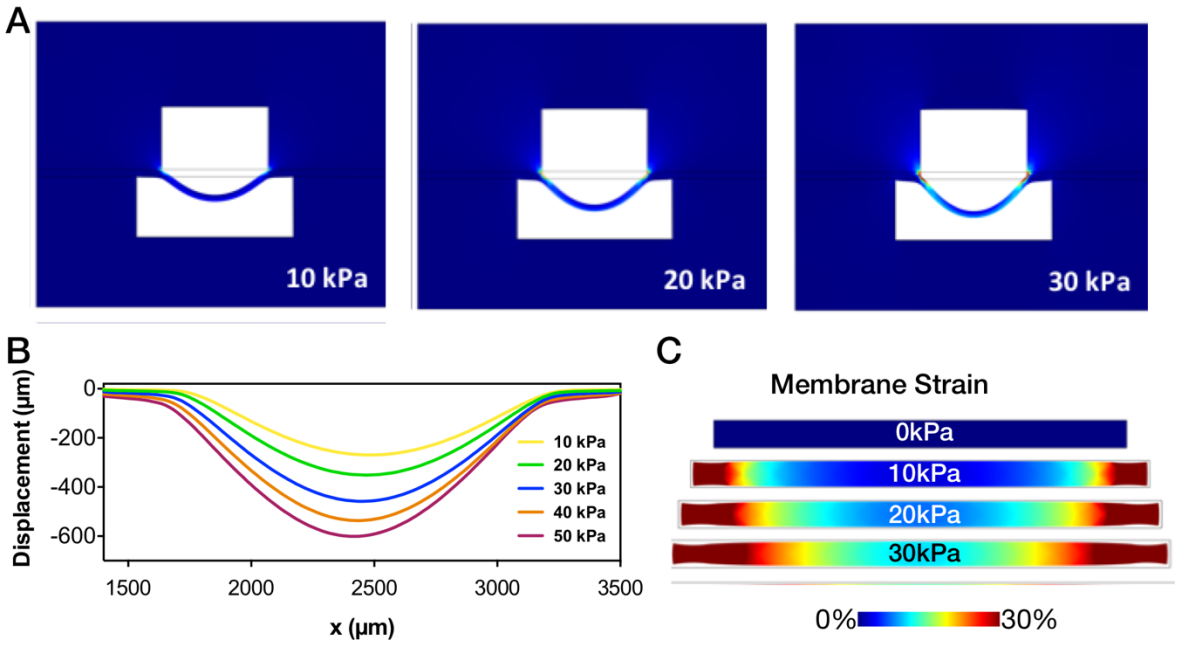

Figure 3.4. Computational simulations of the device. (A) Surface plot of the Von Mises stress distribution at different loads, (B) membrane displacement, and (C) membrane surface strain.

3.3.2 Biomechanical strain induced cell re-orientation and a contractile phenotype in SMCs

Mechanical stimulation regulates morphology and function of SMCs (190). The lack of mechanical strain in static cultures induces SMCs to shift towards a dedifferentiated phenotype, which is characterized by a higher proliferative state, higher protein synthesis, and relatively circular cell shape (190, 191, 222). Upon mechanical stimulation, cells acquire a contractile phenotype that is reminiscent of the *in vivo* state. SMCs under cyclic mechanical strain reorient perpendicular to the strain direction (223, 224). We examined the morphology, orientation, and expression of contractile markers by SMCs under normal and hypertensive mechanical strains. Cells were cultured for 24 hours under cyclic mechanical strain in a microfluidic channel coated with fibronectin. This coating was chosen because SMCs are

more responsive to the cyclic strain on fibronectin-coated substrates rather than other ECM proteins (222). We cultured cells for 24 hours to observe early effects of strain, whereas other studies cultured cells under 48 or 72 hours (222, 225). SMCs under no mechanical strain exhibited a random angle orientation distribution (Figure 3.5A). Strained cells reoriented perpendicular to the direction of strain and increased their aspect ratio (Figure 3.5B-C), with a magnitude-dependent effect. Indeed, the angle orientation distribution of SMCs became narrower and closer to 0º as the stretch was increased from 9% to 16% strain (Figure 3.3D-F). Cell shape analysis revealed a decrease in cell width (Figure 3.5G, Figure 3.6), while no change was observed in cell length (Figure 3.6), resulting in an overall increase in the aspect ratio of the cells (Figure 3.5H). SM22α and β1-integrin are enriched in contractile SMCs (193). Besides, β1- and α5-integrins mediate intracellular signal mechanotransduction *via* adhesion to fibronectin (190-192, 222). Therefore, to evaluate the impact of cyclic stretching in the phenotype of SMCs and their mechanotransduction responsiveness, we measured the expression levels of *TGLN* (encoding SM22α), *ITGB1* (encoding β1-integrin) and *ITGA5* (encoding α5-integrin) gene transcripts by real-time quantitative polymerase chain reaction (qRT-PCR). We found *TGLN, ITGB1* and *ITGA5* mRNA upregulated under 9% and 16% strain (Figure 3.5I). Overall, we confirmed that using our on-chip system SMCs responded to mechanical strain by acquiring a more differentiated contractile phenotype.

3.3.3 Hypertensive strain recapitulates angiotensin II induced phenotype

To evaluate whether a threshold pathological strain induced vascular damage, we analyzed gene expression in cells cultured under strain as compared to static conditions treated with angiotensin II treatment. The renin-angiotensin-aldosterone system is implicated in the development of hypertension and regulates blood pressure *in vivo* by controlling the vascular tone of SMCs (226). In this context, angiotensin II has been demonstrated to generate a hypertensive phenotype in SMCs (226). Caveolin-1 (*CAV1*), a component of caveolae, is an important mediator of signal transduction (227) and plays a role in mechanotransduction in endothelial cells (228). Microarray profiles of vascular tissues have

identified caveolin-1 as a potential target marker of hypertension, showing overexpression in both spontaneous and adrenocorticotropic hormone–induced hypertensive rats (229).

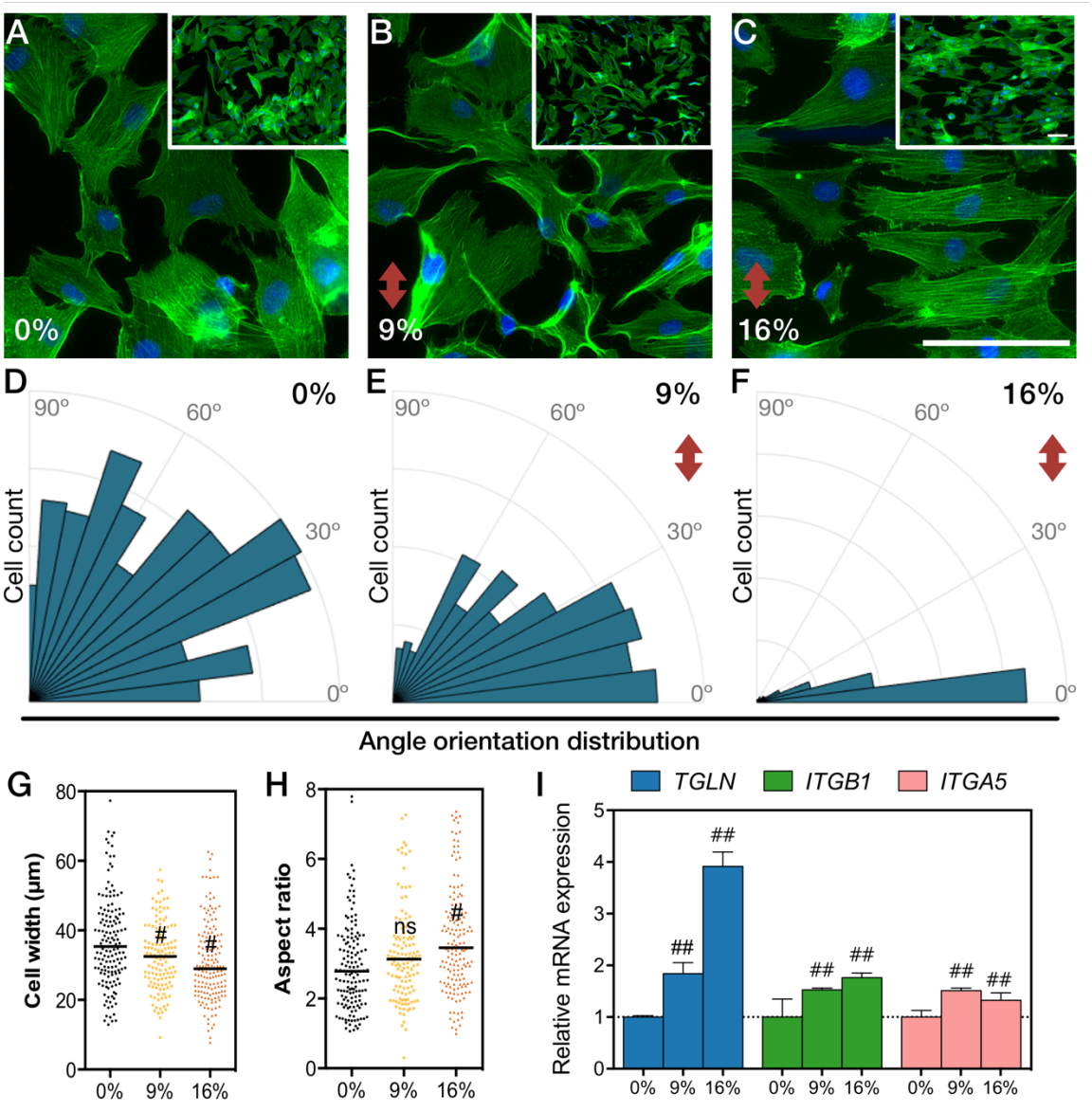

Figure 3.5 – Strain induces cytoskeletal reorientation and contractile phenotype markers on chip. (A-C) Micrographs of f-actin stained cells under different amounts of strain for 24 hours. Cells exposed to different amounts of strain were quantified on (D-E) angle orientation distribution, (G) cell width and (H) aspect ratio (#, P<0.01; ns, not significant; scale bars represent 100 μm and red arrow indicates direction of strain). Relative mRNA expression levels of *TAGLN* (SM22α gene), *ITGB1* (β1-integrin gene) and *ITGA5* (α5-integrin gene) (I) [bars represent mean ± SD of *n*=5; ##, P<0.01].

Similarly, increased expression of caveolin-1 and caveolae has been reported in human pulmonary artery hypertension (230, 231). IL-6 is a major pro-inflammatory cytokine that has

been associated with essential hypertension (129), which is overexpressed in human serum of pulmonary hypertension patients (126) and induces hypertension in mice (232).

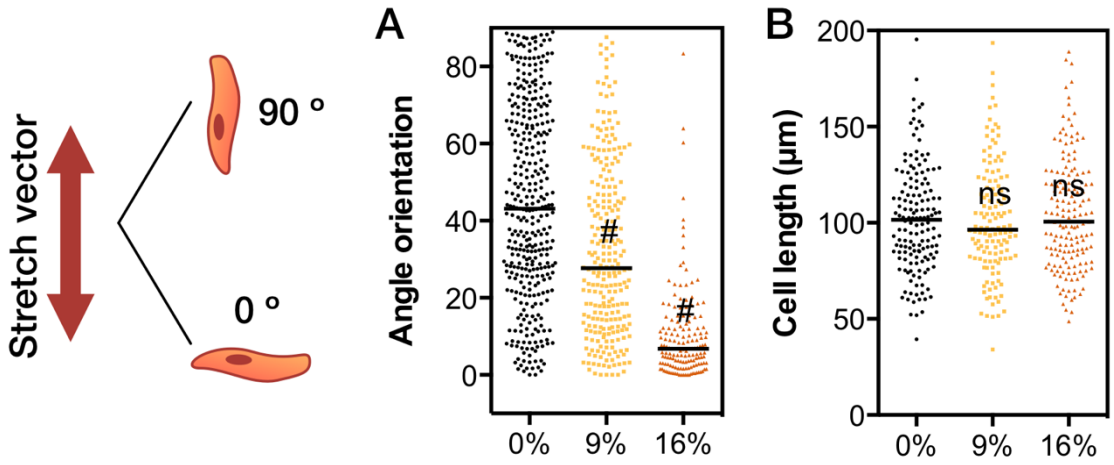

Figure 3.6. Angle orientation and cell length. (A) Plot of angle orientation and (B) cell length of SMCs after 24 hours of exposure to different levels of mechanical strain (#, P<0.001; *ns*, not significant).

Our results showed that culturing SMCs under 9% strain led to minor changes of mRNA expression levels (Figure 3.7A; Figure 3.8), with an increase in the cytosolic superoxide dismutase (*SOD1*) and decrease in mitochondrial one (*SOD2*). Importantly, ROS has been implicated in vascular diseases, and angiotensin II is known to increase mitochondrial ROS (128, 233-235). Both pathological strain (Figure 3.7B) and 100 nM of angiotensin II treatment (Figure 3.7C; Figure 3.9) showed a marked increase in mitochondrial *SOD2*, with a smaller increase in *SOD1*. Interestingly, this observation suggested that under physiological strain ROS was primarily produced in the cytosol. Using the NADPH oxidase inhibitor VAS2870 (20µM) (236) we showed downregulation of the NAPDH oxidase subunit *p22phox* and restoration *SOD1* levels, while no change was observed for *SOD2* (Figure 3.10).

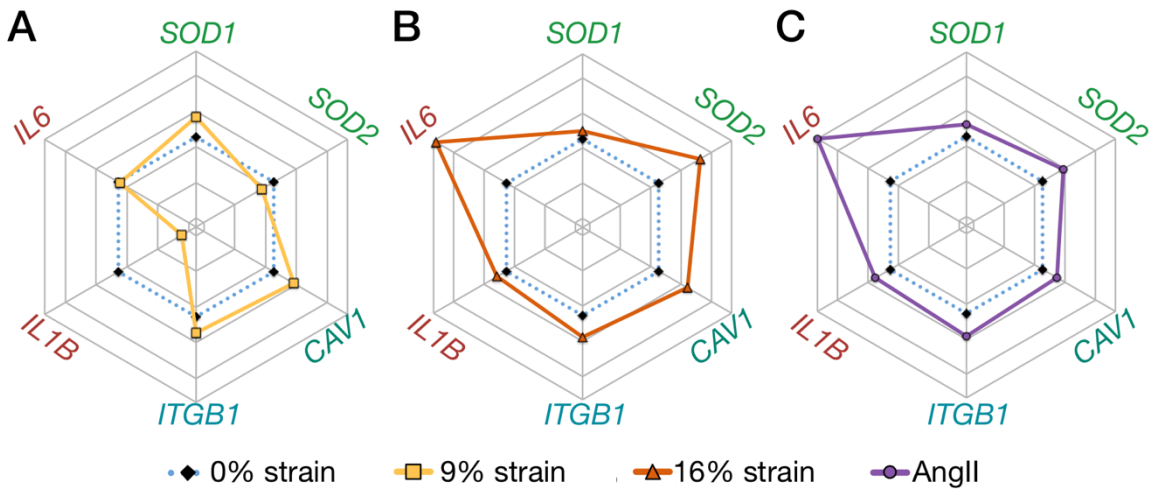

Figure 3.7 – Strain-dependent activation of SMCs recapitulates angiotensin II vascular gene fingerprint. Rose plots of the mRNA expression profiles of SMCs treated for 24 hours under (A) physiological strain (9%), (B) pathological strain (16%), or (C) 100 nM of angiotensin II [AngII] (mean values of *n*=5 for 9% and 16% strain, mean values of *n*=3 for AngII treatment; see Figures S4 and S5 for the bar plots and statistical significance).

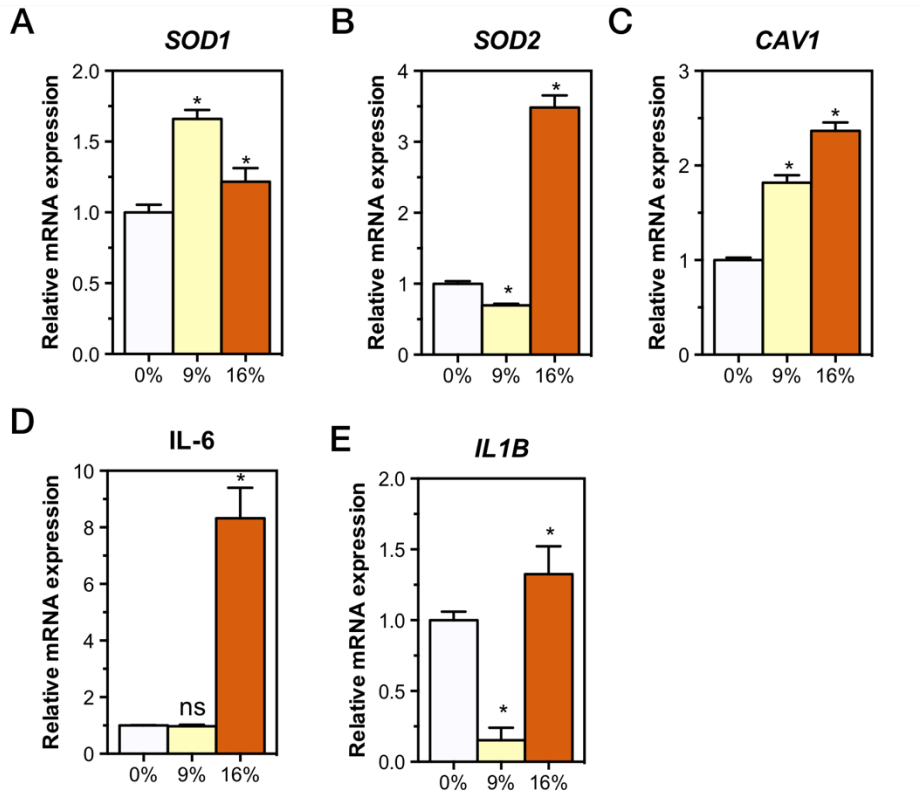

Figure 3.8. Gene expression profile of SMCs under biomechanical strain. Relative mRNA expression levels of (A) *SOD1*, (B) *SOD2*, (C) *CAV1* and (D) *IL6* and (E) *IL1B* in SMCs after 24 hours of exposure to different levels of mechanical strain (bars represent mean ± SD; *, P<0.01 compared to 0% strain).

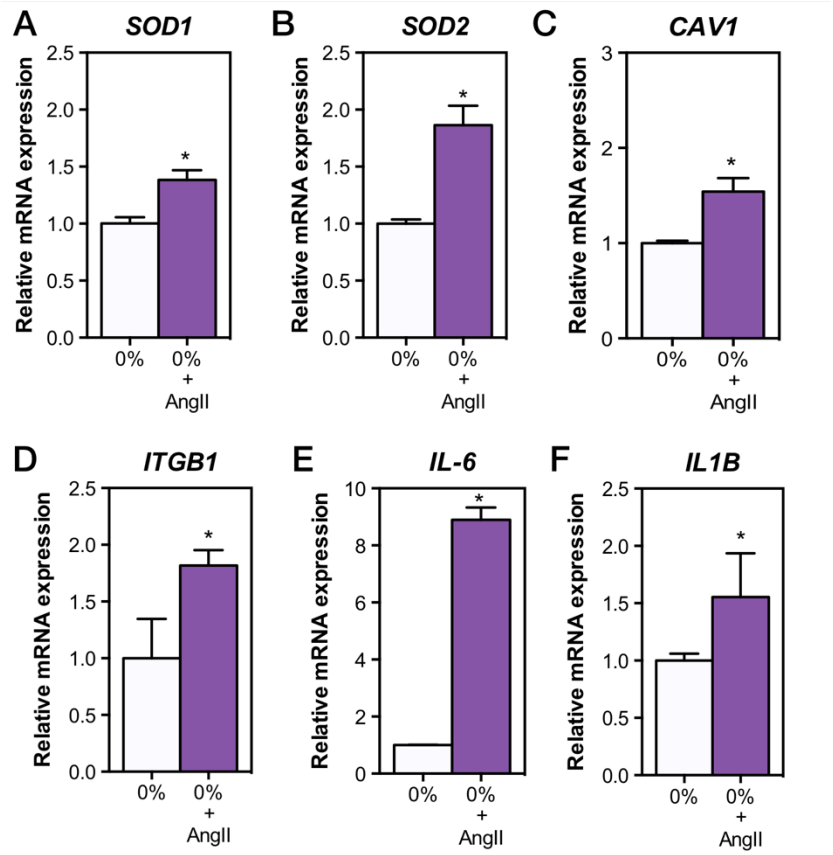

Figure 3.9. Gene expression profile of SMCs under angiotensin II stimulation. Relative mRNA expression levels of (A) *SOD1*, (B) *SOD2*, (C) *CAV1*, (D) *ITGB1* and (E) *IL6* and (F) *IL1B* in SMCs after 24 hour treatment with angiotensin II (AngII; 100nM) (bars represent mean ± SD; *, P<0.01 compared to 0% strain).

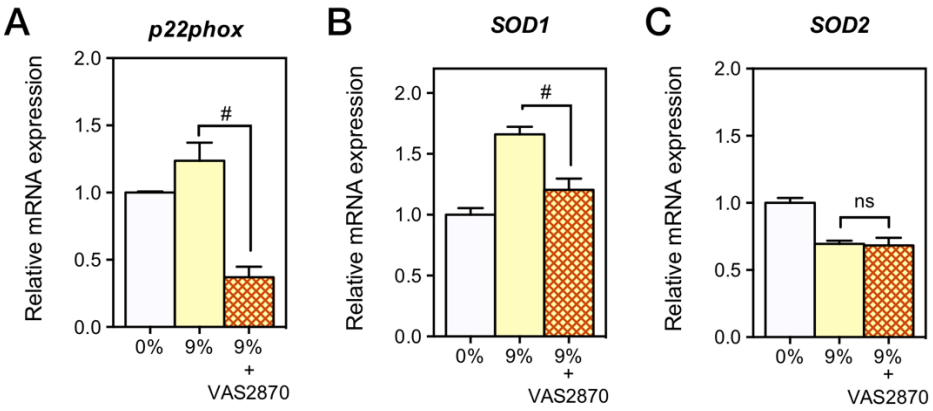

Figure 3.10. Inhibition of ROS via NAPDH oxidase inhibitor under strain. Relative mRNA expression levels of (A) *p22phox*, (B) *SOD1* and (C) *SOD2* in SMCs treated with NADPH oxidase inhibitor VAS2870 under 9% strain for 24 hours (bars represent mean ± SD of *n*=5; #, P<0.002; ns, not significant).

Our results further showed that *CAV1* was upregulated in a strain magnitude-dependent way (Figure 3.8), and a similar increase was shown with angiotensin II treatment (Figure 3.8C; Figure 3.10). Moreover, we showed increase in *ITGB1* with strain and angiotensin II (Figure 3.8) similar to previously reported results (237). The pro-inflammatory markers *IL6* and *IL1B* were significantly increased with hypertensive strain (Figure 3.8B) and angiotensin II (Figure 3.8C), but not with physiological strain. Such difference suggested the existence of a strain-dependent threshold that gates the biomechanically induced upregulation of IL-6 expression in SMCs.

Overall, SMCs under pathological strain conditions exhibited a gene expression pattern similar to angiotensin II treatment, with similar responses of ROS, inflammation, and vascular injury genes, although strain alone may not fully recapitulate the effects of angiotensin II. Further studies are required to understand the regulatory pathways of strain and angiotensin II in SMCs, both alone and in combination.

3.3.4 Healthy and HGPS iPS-SMCs undergo cytoskeletal remodeling upon biomechanical strain

Vascular diseases and aging are intimately linked (238) yet rarely studied in an integrated approach. Due to the relation between vascular disease and aging, we examined the influence of biomechanics in an iPS-derived progeria-on-a-chip model. Stem cell-based models represent ideal candidates to study human diseases due to the practical capability of large scale expansion and differentiation (159). HGPS patients exhibit premature aging, with increased arterial stiffening, expression of pro-inflammatory markers, the risk of atherosclerosis, calcification, and changes in systolic and pulse pressure (165). HGPS and other accelerated aging syndromes have been established as aging models that recapitulate several aspects of cellular aging (154, 162, 163, 165). In HGPS, both progerin and lamin A accumulate in the nucleus (165). We generated SMCs through differentiation (217) of iPS cells derived from HGPS donors (and healthy controls) (164), and evaluated the interplay between biomechanical strain and aging (Figure 3.11A) (165). The generation of iPS cells

from HGPS fibroblasts was previously shown to be similar to healthy fibroblast (164). Importantly, we have characterized the differentiated SMCs derived from HGPS iPS cells, and showed that iPS-SMCs from HGPS donors express significantly higher levels of *progerin* mRNA (Figure 3.11B).

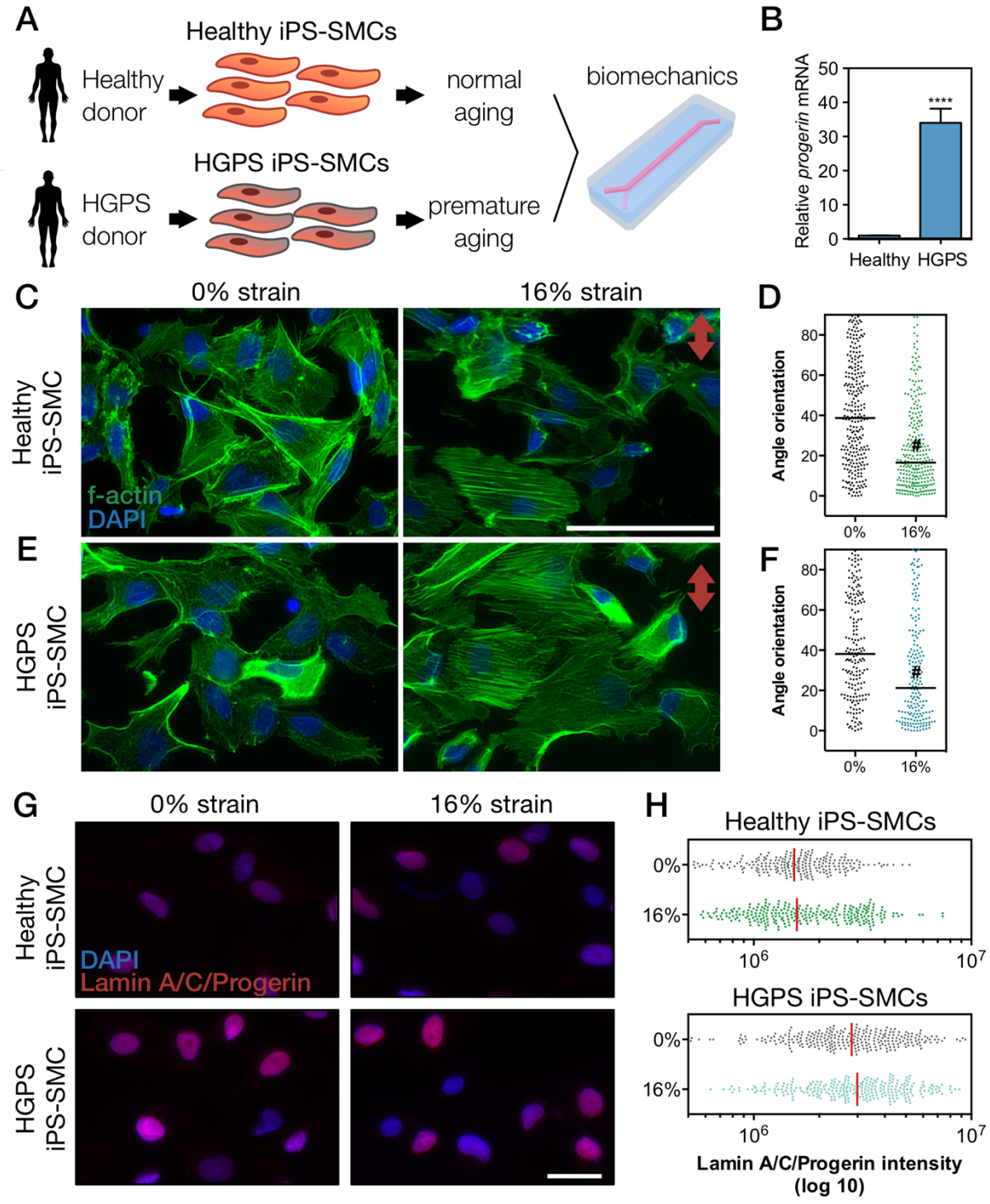

Figure 3.11 – Biomechanical strain induces cytoskeletal reorientation of iPS-SMCs from healthy and HGPS donors. (A) Schematic of the methodology used to explore biomechanical

changes in a context of vascular aging. (B) mRNA expression levels of *progerin* confirmed its overexpression HGPS cells (bars represent mean ± SD of *n*=5). F-actin was stained for (C-D) healthy or (E-F) HGPS iPS-SMCs under 0% and 16% strain for 24 hours and the corresponding angle orientation distribution was determined (#, P<0.0001; scale bars represent 50 μm; red arrow indicates direction of strain). (G) HGPS iPS-SMCs showed increase levels of lamin A/C/progerin (antibody against epitope corresponding to aminoacids 231-340). (H) Quantification of lamin A/C/progerin levels.

Concordant with the alignment results from SMCs (Figure 3.5), iPS-derived SMCs from healthy and HGPS donors showed cytoskeletal reorientation upon mechanical stimulation, while non-stimulated cells showed a random distribution (Figure 3.11C-F).

The accumulation of nuclear lamins and progerin occurs naturally during aging, leading to stiffer and less compliant nuclei (152, 162, 166). Besides promoting nuclear architecture changes (151), this accumulation can further result in alterations in transcription, changes in chromatin structure, and epigenetic changes (152). However, the mechanism and effects of biomechanical strain in a context of lamin/progerin accumulation are still poorly understood. Using the same approach as Cao *et al.* (239), we distinctly evaluated the mRNA levels of *LMNA* and *progerin* with specific primers by qRT-PCR (Figure 3.12).

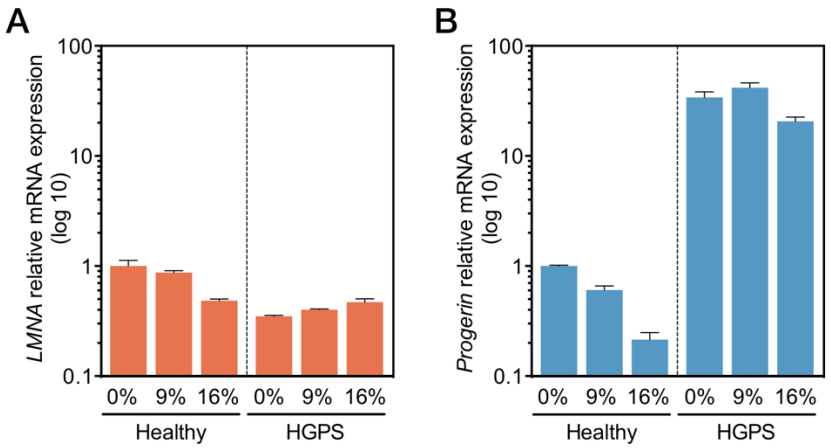

Figure 3.12. Gene expression of *LMNA* and *progerin* in healthy and HGPS iPS-SMCs. Relative *LMNA* (A) and *progerin* (B) mRNA expression levels in healthy and HGPS iPS-SMCs. (bars represent mean ± SD of *n*=5; results are normalized to healthy iPS-SMCs under 0% strain conditions.)

Interestingly, in HGPS iPS-SMCs, physiological strain slightly increased level of *progerin* while pathological strain decreased *progerin* and increased *LMNA*. Healthy iPS-SMCs showed an opposite trend with reduced levels of *LMNA* with physiological or pathological strain. We then used an antibody recognizing both lamin A/C and progerin (epitope

corresponding to aminoacids 231-340) to immunostain (Figure 3.11G) and quantify (Figure 3.11H) the combined protein levels of lamin A/C and progerin. Similar to mRNA levels, we verified also lamin A/C/progerin accumulation in HGPS iPS-SMCs as compared to healthy iPS-SMCs (Figure 3.11G-H). The specific accumulation of lamin A/C/progerin in the nucleus can lead to changes in the mechanical properties (151, 153), having implications for the cell response to strain.

3.3.5 Lovastatin and lonafarnib mitigated the inflammation response of HGPS iPS-SMCs

Several cellular pathways are shared between aging and hypertension, resulting in vascular alterations such as remodeling, stiffness, inflammation, and oxidative stress (119). In particular, HGPS fibroblasts are mechanically sensitive, and under conditions of mechanical stimulation show decreased viability and increased apoptosis (166). We used iPS-SMCs derived from healthy and HGPS donors, and compared the biomechanical response to strain.

The markers *CAV1*, *IL6, IL1B*, and *JUN* drastically increased in HGPS iPS-SMCs under 16% strain (Figure 3.13A-D). This observation demonstrated that pathological strain elicited an exacerbated inflammatory response in HGPS iPS-SMCs that did not occur in healthy iPS-SMCs. However, we showed increased *IL6* mRNA expression in primary SMCs, but have not in healthy iPS-SMCs. One possible explanation for such are the different cell culture medias used; whereas SMC experiments are conducted under serum-free media, iPS-SMCs ones are conducted with smooth muscle growth media. *CAV1* has been identified as a marker of hypertension across different animal models (229, 240) and is elevated in human serum of patients with vascular hypertension (126, 231). The increased expression of the transcriptional factor *JUN* (Jun Proto-Oncogene) suggested further activation of cytokines, beyond the increases in *IL6* and *IL1B,* and has been highlighted as a potential target for anti-inflammatory therapies (241).

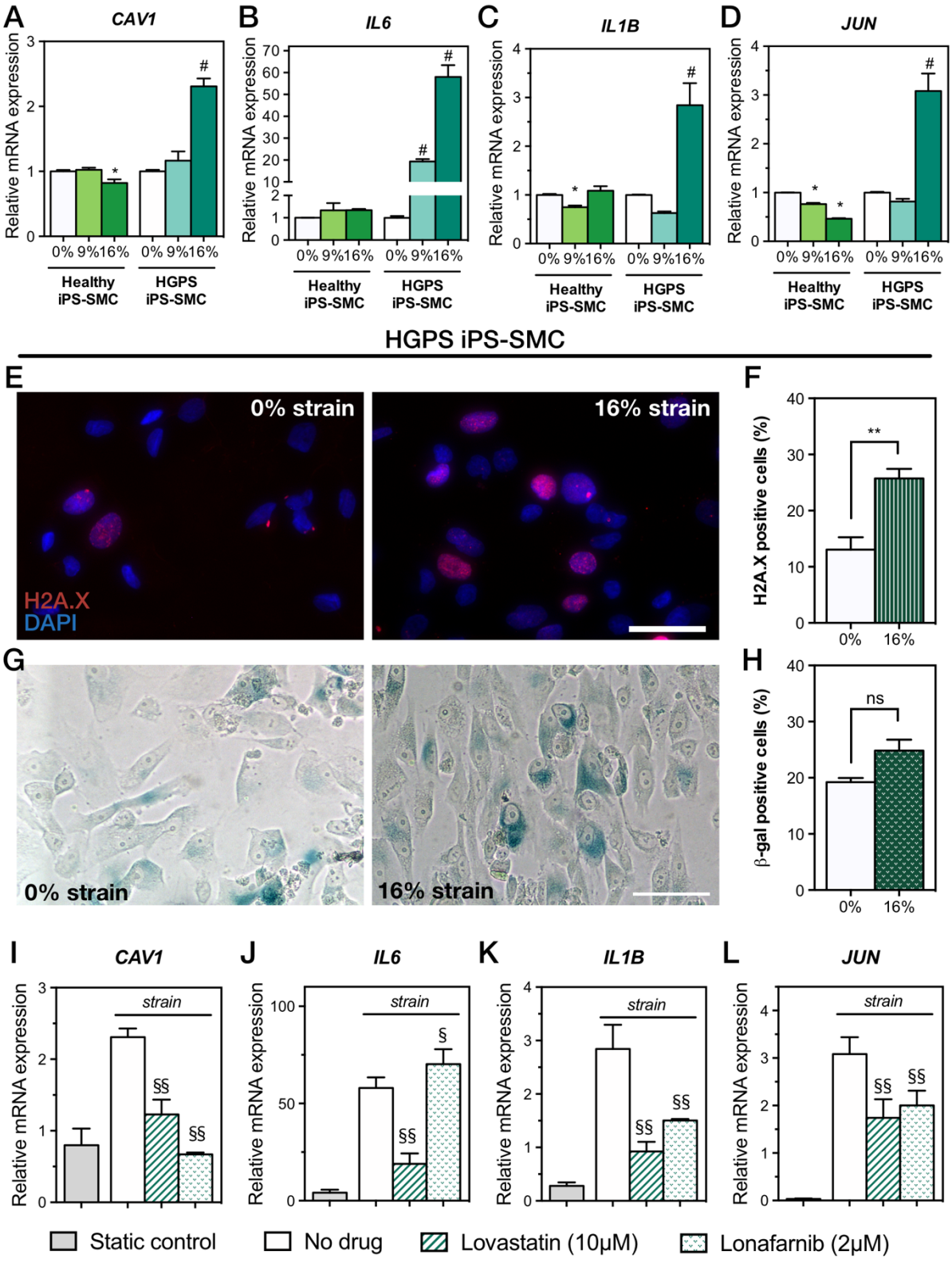

Figure 3.13 – Exacerbated response to biomechanical strain in HGPS iPS-SMCs is rescued by lovastatin and lonafarnib. Relative mRNA expression levels of healthy and HGPS iPS-SMCs cultured under 0%, 9%, and 16% biomechanical strains for 24 hours. Injury marker (A) *CAV1* and inflammation markers (B) *IL6*, (C) *IL1B*, and (D) *JUN* (* P<0.01 against 0% healthy iPS-SMCs, and # indicates P<0.01 against 0% HGPS iPS-SMCs; bars represent mean ± SD of *n*=5). DNA damage was

evaluated in HGPS iPS-SMCs with H2A.X immunostaining (E) and quantified (F) (mean ± SD of *n*=3; **, P=0.0039). Senescence was measured in HGPS iPS-SMCs *via* β-galactosidase activity staining (G) and quantified (H) (mean ± SD of *n*=3; ns, not significant [P=0.0532]). Treatment of HGPS iPS-SMCs under 16% mechanical strain with lovastatin or lonafarnib prevented increased injury and inflammatory markers (I-L), while static control on a Petri dish failed to trigger a response [(§§, P<0.001; §, P=0.04; compared to no drug treatment; bars for lonafarnib and lovastatin represent mean ± SD of *n*=4; bars for static control represent mean ± SD of *n*=3].

Together, evidence suggested that progerin accumulation in HGPS might result in increased mechanosensitivity to pathological strain and led to an exacerbated inflammatory response. The combined action of transcription factor upregulation (*JUN*) and increased pro-inflammatory cytokines (*IL6* and *IL1B*) suggested a cycle of propagation of inflammation that might occur in the vascular wall in HGPS patients and, at a slower pace, in physiological vascular aging. Furthermore, the observation of increased *IL6* expression, together with similar observations in two mouse models of progeria suggested the potential role of the cytokine as a biomarker of disease. We then investigated whether exposure to pathological strain would induce further cellular damage in HGPS iPS-SMCs. DNA damage and cellular senescence have been established as hallmarks of aging (196, 242), and are upregulated in HGPS (154, 155, 160, 243). In our experiments, HGPS iPS-SMCs showed increased DNA damage after 24 hours of biomechanical stimulation (Figure 3.13E-F; P=0.0039). We additionally stimulated cells for 5 days under strain and observed a small increase in senescence (Figure 3.6G-H; P=0.0532). This suggested that HGPS under dynamic pathological strain conditions altered their mRNA expression levels in favor of inflammation and vascular injury. In addition, cells presented endpoint markers of aging such as DNA damage and senescence. Importantly, chronic inflammation, which is observed in HGPS (162), can lead to increased senescence and DNA damage (244, 245) and ultimately accelerate aging (144).

Drug treatments for HGPS primarily aim to reduce levels of progerin. These include inhibitors of the lamin-processing pathway such as 3-hydroxy-3-methylglutaryl coenzyme A (HMG-CoA; statins) (230, 246, 247), farnesyl transferase (FTI) (146, 247-249), and mechanistic target of rapamycin (mTOR) (250). In particular, lovastatin has been shown to

improve the nuclear shape abnormalities in progeroid fibroblasts and to disrupt caveolae and decrease caveolin in SMCs (230, 246). Additionally, statins have been shown to have anti-inflammatory effects (145, 251, 252). We then hypothesized that lovastatin treatment would mitigate changes in mRNA expression levels that were associated with strain in HGPS iPS-SMCs. Indeed, we revealed that administration of 10μM of lovastatin was able to rescue HGPS iPS-SMCs exacerbated injury response on the transcriptional level by preventing increases in *CAV1*, *IL6*, *IL1B,* and *JUN* (Figure 3.13I-L). Lonafarnib is a classic FTI shown to reduce levels of progerin, restore nuclear abnormalities and improve vascular stiffness (248, 249, 253). Treatment of HGPS iPS-SMCs for 24 hours under 16% strain with 2 μM of lonafarnib resulted in a reduction in the levels of *CAV1*, *IL1B,* and *JUN* (Figure 3.6I-L). However, lonafarnib failed to decrease the levels of *IL6*. This might be due to the low exposure time to lonafarnib (24 hours) in comparison to other studies that have treated cells for 72 hours (248). Overall, both lovastatin and lonafarnib were able to ameliorate the exacerbated inflammatory response to strain in HGPS iPS-SMCs, with lonafarnib being more efficient in downregulating the *progerin* mRNA levels. Importantly, culturing HGPS iPS-SMCs under conventional cell culture systems (Petri dish) failed to trigger inflammatory and vascular injury markers (Figure 3.13I-L).

3.4 Discussion

Here, we have developed a microfluidic device that is easy to manufacture and enables the characterization of cellular responses across a range of physiological and pathological strain levels. Besides a standalone progeria-on-a-chip model, the developed device could potentially be integrated in a multi-organ-on-a-chip system to provide a biomimetic vascular platform and detect system-wide effects on the vasculature. We have improved important aspects of the device design in comparison to other previously reported designs (206, 208, 219, 220). The fabrication methodology is simple, less expensive, and does not require highly trained operators. Our device can be conveniently scaled up to a large amount of parallel channels to serve as a high-throughput platform for vascular drug

development. Additionally, the strain levels are fully characterized *in situ* and *in silico*, allowing the application of strain in a wide range. Within the device, the entire cell population can be analyzed and visualized under any conventional fluorescence microscope, and the cells can be removed from the device via trypsinization for further assays.

Using our device, we showed that primary SMCs acquire a more contractile phenotype in vitro following exposure to strain, thus better recapitulating the *in vivo* phenotype. Morphological changes and higher expression of *TAGLN*, *ITGB1* and *ITGA5* suggested a more contractile phenotype and pointed towards higher mechanotransduction sensitivity via increased integrin expression (192, 222). These results are in agreement with previous reports (222, 224, 225) showing the alignment of SMCs under strain conditions. We next hypothesized whether a pathological strain level would induce cellular changes similar to hypertension. According to several studies, the hypertensive phenotype is characterized by an increase of mitochondrial ROS (128, 233-235), caveolin-1 (227, 228), IL-6 and IL1-β (126, 129) expression. The exploration of strain-magnitude unveiled a gene expression profile similar to treatment with angiotensin II, a compound known to be implicated in the development of hypertension. We indirectly assessed the levels of ROS through mRNA expression of cytosolic and mitochondrial superoxide dismutase (*SOD1* and *SOD2* respectively). We observed a distinct regulation of SOD1 and SOD2 depending on the strain amount. Whereas normal strain levels elicited increased expression of cytosolic superoxide dismutase, pathological strain levels elicited increased expression of mitochondrial one. By inhibiting cytosolic ROS increase with a NADPH oxidase inhibitor, we were able to specifically decrease *SOD1* under normal strain without affecting the levels of *SOD2*. This observation suggested that different strains might have distinct effects on ROS production, but further studies are required to elucidate the influence in vascular disease. Pathological levels of strain induced higher expression of vascular injury marker *CAV1*, which has been reported in patients with pulmonary hypertension (230, 231), identified in microarray screenings and proposed as a potential target marker of hypertension (229). Also, we observed an increase in the pro-inflammatory cytokine mRNA levels of *IL6* and *IL1B* under

pathological strain levels. These have been implicated additionally in hypertension and aging (126, 129, 232). Evidence suggests that pathological strain levels can indeed recapitulate some of the hallmarks observed in vascular disease and elicited by angiotensin II treatment. These alterations point to the existence of a threshold pathological strain that elicits an injury response. However, still more research is needed to understand the specific underlying pathways and potential identification of novel therapeutic targets, such as the Ras/MAPK/ NF-κB pathways (132).

There is a strong association between aging and cardiovascular diseases, and aging alone is the single most important risk factor for the development of cardiovascular diseases (162, 238). Additionally, inflammation is a potential mediator in the pathogenesis of several vascular diseases, including hypertension and atherosclerosis (125, 130, 195). Mouse models that phenotypically recapitulate HGPS show increased activation of NF-κB with a concomitant increase in IL-6 at the transcriptional and protein levels (167). Conversely, a mouse model of low-level chronic inflammation showed accelerated aging with increased expression of IL-6, IL1-β, and a decrease in SOD2 (144). Together, these findings highlight a potential role for inflammation and oxidative stress in the vascular wall during aging and vascular disease (233, 234). Our progeria-on-a-chip system is a crucial step towards the understanding of biomechanics of aging. HGPS targets primarily vascular cells, which are under constant mechanical stimulation. Due to lack of data specific for progeria blood vessel strain levels, we hypothesized an increase in pathological strain associated with premature aging. Here we explored a platform that combines both biomechanical stimulation and iPS-SMCs derived from HGPS patients. The HGPS iPS-SMCs expressed progerin in 15% of the cells, and were not further enriched. However, the pooled qPCR results indicated a ~30-fold increase in *progerin* mRNA levels in iPS-SMCs from HGPS donors. Additionally, artificially overexpressing progerin could result in a level higher than disease, resulting in higher cell death or an over response to strain, which could reduce the relevance of the work. We showed that iPS-SMCs from both healthy and HGPS go under cytoskeletal reorientation under mechanical strain. Furthermore, we showed that HGPS-derived vascular cells

demonstrated an exacerbated effect following biomechanical strain, which was unobserved using conventional planar cell culture methods (Petri dish). With this platform, we showed a unique exacerbated increase in inflammatory mRNA levels of markers *IL6*, *IL1B*, and *JUN*, as well as the vascular injury marker *CAV1*. Importantly, there is a strong link between inflammation and vascular diseases and aging, which is highlighted in the current work. We showed additionally that a statin (lovastatin) was able to prevent biomechanically induced inflammatory response, likely through anti-inflammatory effects and not directly by reducing progerin levels. Lonafarnib treatment was able to reduce levels of progerin and rescue the inflammatory and injury gene expression profiles of *IL1B*, *JUN*, and *CAV1*. However, the results suggested differences between healthy iPS-SMCs and primary SMCs, and a direct comparison might be hindered by several factors. One possible explanation for such is the different cell culture media used. The cell culture medium that maintained the iPS-SMC phenotype was smooth muscle growth medium (SmGM), being also used to expand primary SMCs. However, primary SMCs tend to dedifferentiate in culture with SmGM medium , thus requiring a starvation medium (216). The starvation medium used for primary SMCs is less rich, while iPS-SMCs experiments were performed in a richer media (SmGM). In addition, the primary SMCs used here were from aortic origin, and might have phenotypic differences compared to a generic SMC phenotype beyond the traditional SMC markers SM-MHC and calponin. Together, these factor could explain some of the differences observed, and more research is needed to shed light onto tissue-specific SMCs differences in mechanosensitivity.

The progeria-on-a-chip system allowed the unveiling of new strain-derived *in vitro* mechanism that leads to increased *IL6* mRNA levels. Although the increase in *IL6* mRNA has been reported for progeria models *in vivo*, we showed here similar responses *in vitro*. We highlight the potential role of the pro-inflammatory cytokine IL-6 as a marker of vascular disease and potentially useful in assessing progression of HGPS. Further studies are required for the validation of IL-6 as a potential marker of disease. We hypothesize that further utilization of this platform can lead to an improved understanding of biomechanics in vascular biology. In particular, the exploration of combined effects of strain frequency,

periodicity, and shear stress is expected to yield novel biological insights. Gaining deeper understanding of the molecular pathways regulating inflammation during vascular aging might pave the way for new strategies to minimizing cardiovascular risk with age. Finally, we expect the newly developed tool to serve as a standardized platform technology to study the effects of biomechanics in vascular biology, disease, and aging, while facilitating the discovery of new drugs.

CHAPTER IV

MONITORING ORGANS-ON-CHIPS

Adapted from Yu Shrike Zhang, João Ribas, et al., and Ali Khademhosseini, “A cost-effective fluorescence mini-microscope for biomedical applications”, Lab on a Chip,15: 3661-3669 (2015).

Ribas devised the concept, Zhang devised the oxygen sensing concept, Ribas wrote the paper, Ribas performed experiments to build the mini-microscope, create different magnifications, use fluorescence capabilities, monitor LIVE/DEAD, and analyze morphology and beating behavior.

Chapter IV – Monitoring organs-on-a-chip

4.1 Introduction

Optical microscopy has had a pivotal role in biology and medicine since the 16th century. For the past few centuries tremendous amount of advancements has been made in enhancing image resolution, improving multifocal imaging, and strengthening the instrumentation. For example, various modalities based on interference such as phase contrast microscopy and differential interference contrast microscopy were developed to inspect cellular structures at better contrast (254, 255). The invention of fluorescence microscopy in the 1910s further expedited the entire field at a faster-than-ever pace by introducing the capability to probe specific molecules/organelles of interest via targeted trackers instead of less specific observations obtained through optical imaging techniques (256). Several of the more recent advances were due to instrumentation, specifically super-resolution microscopy such as stimulated emission depletion (STED) microscopy (257, 258), as well as volumetric imaging modalities such as confocal and two-photon microscopy (259, 260).

Although these techniques provided and continue to provide high-end capabilities in probing biological processes, often times they cannot satisfy the need for high-throughput observations due to their bulky volumes. Additionally, current instrumentation available in the laboratory is difficult to mount inside an incubator, forcing one to transfer biological samples between the incubator and the microscope. Frequent disturbance of the cells may adversely affect their behavior and can be detrimental to certain cell types such as cardiomyocytes, which are highly sensitive to external perturbation and temperature alterations. Recent advances in device-based biological systems have further challenged the existing microscopy techniques where long-term, *in situ*, and simultaneous monitoring of parallel systems is required instead of extended resolution (261-263). As an example, microfluidic organ-on-a-chip platforms builds upon interconnected human organ models, which maximally recapitulate the biology of their *in vivo* counterparts and the physiology of the circulatory system (264-269). Due to its ability to simulate conditions of the human body, organs-on-a-

chip have been widely used as a platform to screen potential new pharmaceutical compounds, personalized medicine therapies, as well as antidotes against biological/chemical weapons (270-276). In order to take advantage of such technologies, a variety of biosensors needs to be embedded into the platforms to monitor in real-time the responses of individual organ modules and their microenvironment. However, the measurement of these parameters in complex microfluidic systems would be impractical using conventional bench-top microscopy. Therefore, there is a strong need to develop optical instrumentation that allows high-throughput application in organs-on-a-chip.

Several compact image sensors have become available based on the lens-free approach (277-280). For example, using a lens-free imaging system the beating behavior of neonatal cardiomyocytes upon treatment with drugs (doxorubicin and isoprenaline) was analyzed in real time (281). Recent advances in the field have further led to the development of an ultra-portable foldable origami microscope (282), as well as several mobile phone-based strategies that can even image DNA strands (283), fluorescent nanoparticles, and virus (284). Despite being attractive solutions, these miniature imaging systems are not optimized for long-term monitoring of device-based biological systems *in situ*.

Based on previous published work on a bright-field mini-microscope (281, 285) here we further developed a system with built-in fluorescence capability that can be universally mounted at the bottom of any microfluidic bioreactor and device. With a high resolution of <2 μm and adjustable magnifications of 8-60X, the mini-microscope could monitor in real time cellular behaviors including cell growth/doubling and beating analysis of liver- and heart-on-chips, respectively. The fluorescence capability further enabled *in situ* observation of hepatocyte viability stained with calcein/ethidium homodimer-1 (EthD-1; Live/Dead kit) prior to, and upon, treatment with acetaminophen. Finally, we demonstrated the possibility to use the fluorescence mini-microscope as an oxygen sensor for intra-organoid measurement of oxygen levels. This mini-microscope created here is miniaturized at a low-cost, allowing for simultaneous integration of multiple units for *in situ*, high-throughput imaging and analysis.

4.2 Materials and Methods

4.2.1 Designing and construction of the mini-microscope

A commercially available, off-the-shelf Logitech C160m USB web camera was dissembled to remove the plastic casing and expose the complementary metal-oxide semiconductor (CMOS) sensor. The base structure of the mini-microscope was fabricated from a 3-mm poly(methyl methacrylate) (PMMA) sheet by laser cutting (VLS 2.30 Desktop Laser System, Universal Laser Systems). Four rectangular PMMA frames were cut out, with circular holes near the edges for the assembling screws/bolts. The bottom PMMA frames held the CMOS unit and lens while the top frames held the sample to be imaged (e.g. a microfluidic bioreactor) and the light source. Four sets of screws/bolts were mounted at the edge between the base and the sample holder for convenient focus adjustment.

To convert the webcam into the mini-microscope, we inverted the lens to achieve magnification, rather than the de-magnifying mechanism adopted by the camera (285). To achieve different magnifications, cylinders of various heights were cut from 2.0-mL Eppendorf tubes to set desired distances between the objective and the CMOS sensor. The tubes were further wrapped in black tape to prevent ambient light from reaching the sensor. Images were acquired with a laptop computer by connecting the camera through the USB port using either the webcam program or a custom-written MATLAB (Mathworks) programs.

4.2.2 Quantification of resolution and field-of-view

A positive resolution target (R1DS1P, Thorlabs) was used to evaluate the resolution of the mini-microscope. Bright-field images were captured and the pixel intensities across the patterns on the resolution target were measured using ImageJ and plotted. Polystyrene microparticles of 16 μm in diameter were also used to qualitatively assess the magnification. Field-of-views were measured by imaging a hemocytometer and calculating the frame size based on the grids.

4.2.3 Digital channel separation with MATLAB

A custom-coded MATLAB script was used to split composite, as-captured images, into separate channels of red, green, and blue (RGB). Briefly, the obtained image was imported into the MATLAB program and the three co-registering two-dimensional (2D) arrays were extracted from the three-dimensional (3D) matrices that represented images for red, green, and blue channels, respectively. The selected channels were then pseudo-colored to render the colors of each channel.

4.2.4 Construction of bioreactors

Resealable microfluidic bioreactors based on polydimethylsiloxane (PDMS, Dow Corning Sylgard 184, Ellsworth) were fabricated by modifying our recently developed protocol. Briefly, the bioreactors had a dual-layer structure with the inlet and organoid culture chamber on the bottom layer while outlet on the top. The two PDMS layers could be separated for organoid seeding, after which closure and sealing were achieved by clamping the pieces using a pair of PMMA surfaces tightened by screw/bolt sets.

HepG2 human hepatocellular carcinoma cells (HB-8065, ATCC) were seeded onto the bottom of the bioreactors at a density of approximately 1000 cells mm^{-2}. Cultures were maintained at a flow rate of 200 µL h^{-1} in a Dulbecco's Modified Eagle's Medium (DMEM, Life Technologies) supplemented with 10% fetal bovine serum (FBS, Life Technologies) and 1% penicillin-streptomycin (P/S, Life Technologies). NIH/3T3 fibroblasts (CRL-1658, ATCC) were seeded onto the bottom of the bioreactors at a density of approximately 200 cells mm^{-2}. Cultures were maintained in the same medium with HepG2 cells at a flow rate of 200 µL h^{-1}. Neonatal rat cardiomyocytes were isolated from Sprague-Dawley rats of 2 days old following our established protocol approved by the Institutional Animal Care and Use Committee (286). The cardiomyocytes were then seeded onto gelatin methacryloyl (GelMA) hydrogel sheets (6 × 6 mm^2) containing 1 mg mL^{-1} carbon nanotubes (CNTs) at a density of 5 × 10^5 cells (287, 288). The cell-seeded GelMA-CNT mats were first cultured in a petri dish DMEM supplemented with 10% FBS, 1% P/S, and 1% L-glutamine (Life Technologies) for up to 3 days until consistent beating was observed. The constructs were subsequently transferred to

the bioreactors and maintained in the same medium at a flow rate of 200 μL h^{-1}.

4.2.5 Live/Dead cell viability assessment

Fluorescence cell viability analysis for liver-on-chips were performed using the Live/Dead kit (Life Technologies) according to manufacturer's instructions. When necessary, acetaminophen (Sigma-Aldrich) was added into the liver bioreactors at a concentration of 10 mM for 24 h of circulation prior to viability assay.

4.2.6 Oxygen measurements

PDMS microbeads with a uniform size of 30 μm were generated using a microfluidic flow focusing devices. Specifically, we used a three-to-one converging flow-focusing microchannel device to produce PDMS droplets, using uncured PDMS prepolymer (10:1) as the dispersive phase and 5 wt.% sodium dodecyl sulfate (SDS, Sigma-Aldrich) aqueous solution as the continuous phase. Obtained PDMS droplets were then cured at 60 °C before infusion with oxygen-sensitive dye, tris(4,7-diphenyl-1,10-phenanthroline) ruthenium(II) dichloride (ruthenium, Alfa Aesar) and oxygen-insensitive dye, Nile Blue (Sigma-Aldrich). Beads were incubated in a dichloromethane (Sigma-Aldrich) solution of ruthenium (5 mg mL^{-1}), which also served as the swelling agent of PDMS to facilitate the infusion of the dyes into the microbeads. The dichloromethane solution was removed, briefly rinsed with isopropanol containing ruthenium, and extensively washed with distilled water for at least five times to minimize the presence of solvents. The beads were then immersed in an aqueous solution of Nile Blue (1 μg mL^{-1}) for 24 h. The fluorescence of ruthenium was excited at 455 nm while that of Nile blue was excited at 591 nm. In order to improve the sensing resolution of the mini-microscope, a high-pass filter of >610 nm (common emission range of both dyes) was used.

Intra-organoid oxygen levels were measured by encapsulating the oxygen-sensing PDMS beads within a liver organoid made from HepG2 cells inside a GelMA hydrogel. A total of 2 μg of 5 wt.% GelMA prepolymer in phosphate-buffered saline (PBS, Life Technologies)

containing 2 × 10^6 cells mL^{-1} and 2 × 10^4 beads mL^{-1} was printed at the center of a bioreactor and UV-crosslinked for 10 s. Another layer of GelMA containing only the beads but no cells was further crosslinked on top to cover the inner organoid. The culture was maintained for up to 24 h in a closed loop driven by a peristaltic pump at a flow rate of 200 µL h^{-1}.

4.3 Results and Discussion

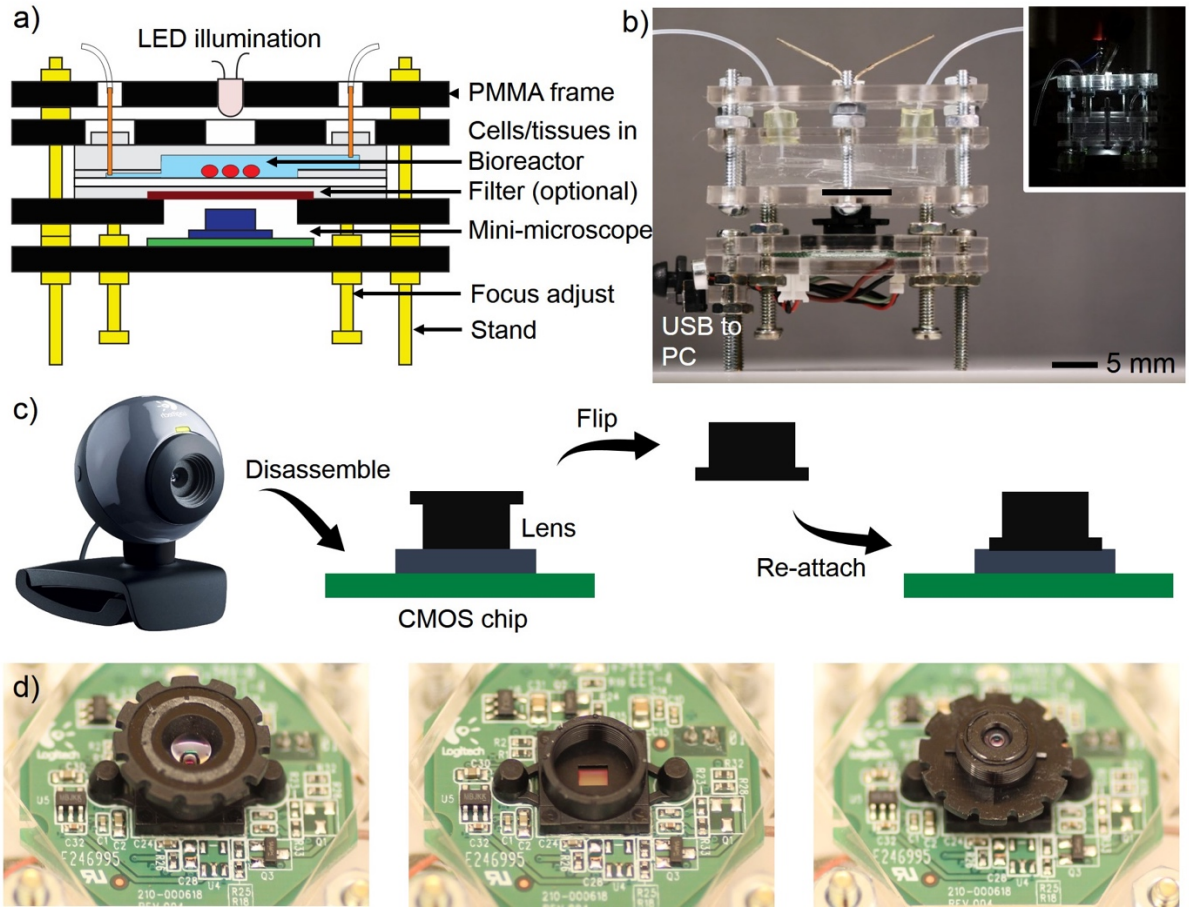

Figure 4.1 – a) Schematic showing the design of the mini-microscope integrated with a bioreactor. b) Photograph showing the actual device; the inset shows the device under LED illumination. c, d) Fabrication of the imaging unit of the mini-microscope: a webcam (Logitech C-160) is first disassembled to obtain the CMOS chip, after which the lens is detached, flipped, and then re-attached to the base to achieve magnification.

4.3.1 Design and characterization of a mini-microscope

Tracking cellular processes and tissue responses over time requires the use of specialized and expensive microscopes with a temperature-, humidity-, and CO_2-controlled chamber. Laboratories often have multiple users and/or limited access, which makes the

analysis of multiple samples in real-time challenging and time-consuming. To fulfil these needs, we have developed a fluorescence mini-microscope (Figure 4.1, a and b) with out-of-the-shelf components and encased it within a specially designed PMMA frame for easy integration with existing tissue culture devices such as microfluidic bioreactors. The mini-microscope has a small form factor (4.2 × 5.5 cm^2) and is highly portable (65 g). It has a series of applications comparable to a bench-top fluorescence microscope such as live cell imaging, long-term tracking of cellular processes, fluorescence analysis, and potentially biosensing. The reduced cost of each microscope (<$10), together with readily available off-the-shelf parts, enables researchers to manufacture several units in a laboratory setting with minimum investment. This is an ideal solution to economically track multiple samples at once. Additionally, using the mini-microscope directly inside the incubator avoids extra steps that can contribute to cell damage, including changes in temperature, pH, and increased chance of microbial/fungal contaminations. With the emergence of cell-based lab-on-a-chip applications, we highlight the nature of our modular plug-and-play mini-microscope, which is capable of connecting to different setups via screws and bolts.

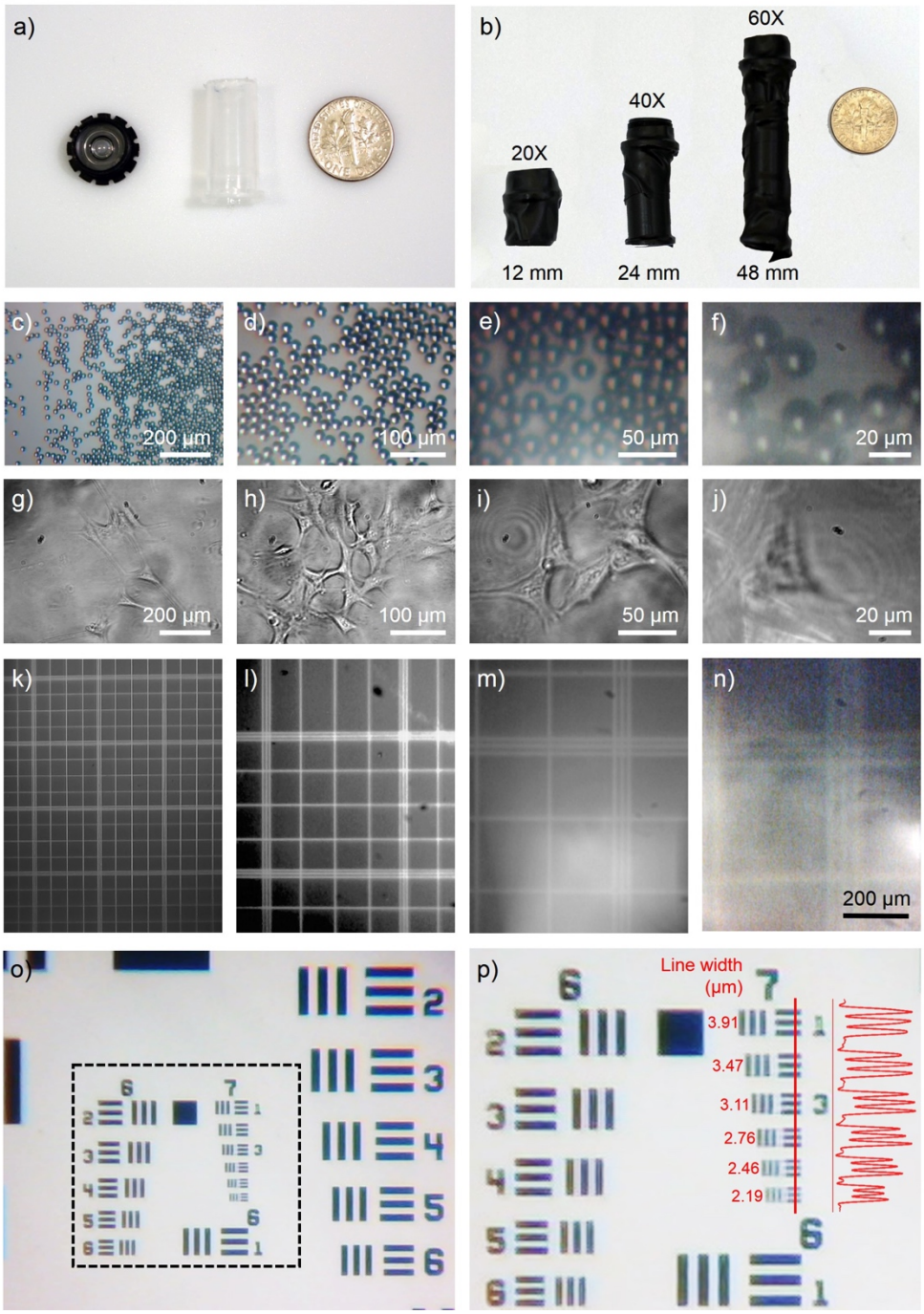

Figure 4.2 – a, b) Photographs showing the assembly of the objective with different magnifications by varying the height of the tubing. c-f and g-j) Mini-microscopic images of 16-µm polystyrene particles and NIH/3T3 fibroblasts at four different magnifications of 8X, 20X, 40X, and 60X. k-n) Full frame images of a hemocytometer captured from the mini-microscope at different magnifications where the field-of-views were calculated to be 1060 µm × 850 µm = 0.901 mm^2, 500 µm × 400 µm = 0.200 mm^2, 235 µm × 190 µm = 0.045 mm^2, and 130 µm × 105 µm = 0.014 mm^2, respectively. o, p) Mini-microscopic images of a resolution target showing Groups 6 and 7 targets where the microscope could easily resolve lines/spacing as small as 2.19 µm; the inset shows the intensity profile across the red line in the Group 7 targets.

The body of the mini-microscope was constructed by inverting the webcam lens to magnify the object (Figure 4.1, c and d) (285). By varying the distance between the lens and the CMOS sensor using a spacer constructed from an Eppendorf tube, we could obtain a continuous gradient of magnifications. Using this approach, we were able to equip the mini-microscope with 8X, 20X, 40X, and 60X magnifications at lens-to-sensor distance of 5 mm (no spacer), 12 mm, 24 mm, and 48 mm, respectively (Figure 4.2, a and b). As shown in Figure 4.2, c-f and g-j, polystyrene microbeads of 16 μm and NIH/3T3 fibroblasts could be clearly imaged under all these four magnifications. We then imaged a hemocytometer and determined the field-of-views of the mini-microscope at different magnifications to be 0.901 mm^2, 0.200 mm^2, 0.045 mm^2, and 0.014 mm^2, respectively (Figure 4.2, k-n).

In order to suit the majority of the applications, a lower magnification of 8X was chosen for subsequent characterizations. We determined the mini-microscope resolution by imaging a photographic resolution target. As shown in Figure 4.2 (o and p), the microscope was able to resolve lines as closely spaced as 2.19 μm with clear peak separation. Such high resolution is sufficient for most laboratory applications on cell-based measurements. The design of the mini-microscope included four sets of screws/bolts for convenient focus adjustment (Figure 4.1, a and b). The working distance was determined to be 4.5 mm by imaging targets at pre-set distances from the objective. The mini-microscope had a maximal resolution of 1280 x 1024 pixels (1.31 megapixels; inherent from webcam resolution) and a maximum frame rate of 30 frames per second (fps).

4.3.2 Filter-free color separation and fluorescence capability

One critical functionality for the use of a small and portable mini-microscope is its fluorescence capability. Tagging cells, subcellular compartments, and extracellular matrix (ECM) molecules with fluorescence markers allows extended monitoring with increased sensitivity and precision. Moreover, various cellular functional assays involve the usage of fluorescence tags, which highlights the importance of constructing a fluorescence-capable

microscope. A color CMOS sensor is typically constituted by an array of interlacing red, green, and blue (RGB) sensing units (i.e. pixels, Figure 4.3a), composing a final RGB image when mixed together. A key aspect in using fluorescence is filtering the excitation light from the emission. While conventional methods are all based on the use of filters, we opted for a filter-free approach by digitally separating the red, green, and blue components of an obtained raw image, therefore distinguishing the contributions of the source from the emitter.

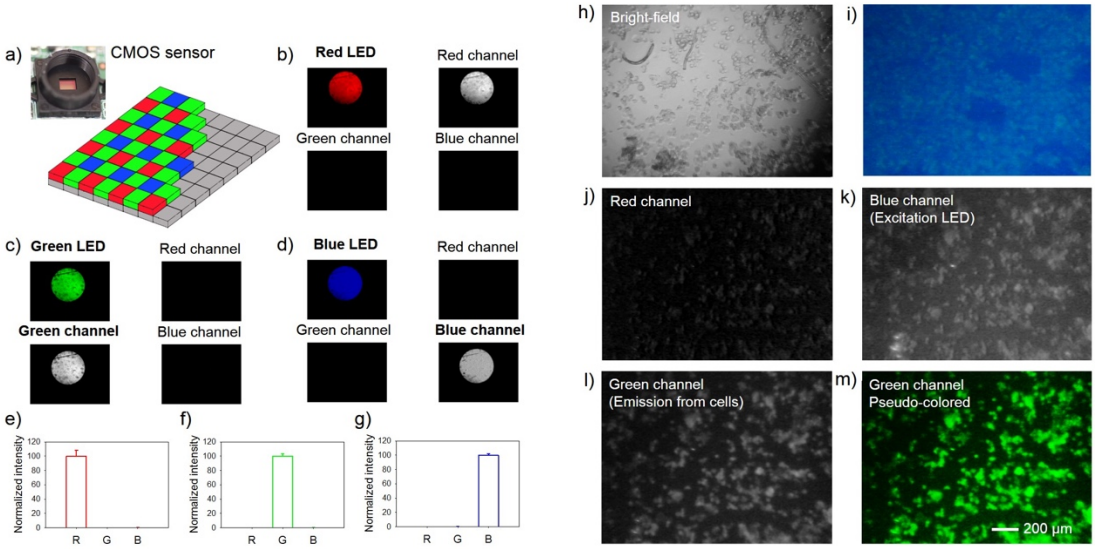

Figure 4.3 – a) Schematic showing RGB configuration of the CMOS sensor of the mini-microscope. b-d) RGB and R/G/B images showing the filter-free separation of R, G, B colors by taking advantage of the digital channel unmixing using a custom-coded MATLAB program. e-g) Quantification data showing the accuracy and sensitivity of the digital channel separation approach. h) Bright-field image showing HepG2 cells grown in a liver-on-a-chip device. i) The raw image obtained from the mini-microscope showing the same HepG2 cells stained with calcein and illuminated with a monochromatic LED at 490 nm. j-l) Images from R/G/B channels after separation, respectively. m) Pseudo-colored and contrast enhanced image of the G channel showing the fluorescence from the stained cells with minimal interference from the illuminating B channel.

A custom-coded MATLAB program was used to split the acquired images into separate R/G/B components. In order to demonstrate our concept, we used red, green, and blue LEDs as the emission sources and digitally separated the obtained images into three channels (Figure 4.3, b-d) and analyzed the emission intensities (Figure 4.3, e-g). As expected, each LED had a narrow wavelength of emission within its own range and gave a clear high-intensity signal in each respective RGB channel with minimal interference in other channels. To evaluate the fluorescence capability of the mini-microscope on imaging

biological samples, we cultured HepG2 cells at the bottom of a liver bioreactor and stained them with calcein AM (1 μM for 20 min). A bright-field image captured under a broadband LED revealed the morphology of the cells (Figure 4.3h). We then used a blue LED (490 nm) to excite calcein for fluorescence detection. Without channel separation, it is noticeable that both the excitation light (blue) and the emission light (green) were mixed together (Figure 4.3i), rendering the observation of the fluorescence signals unusable. In comparison, when we digitally split the acquired image into distinct R/G/B components (Figure 4.3, j-l), we could clearly retrieve the blue excitation component in the blue channel (Figure 4.3k) and the green emission from calcein AM in the green channel (Figure 4.3l), with slight residual emission in the red channel (Figure 4.3j). A final pseudo-colored image (Figure 4.3m) with minimal interference from other channels was then obtained, showing the fluorescently labelled cells in the same way as viewed on a bench-top fluorescence microscope.

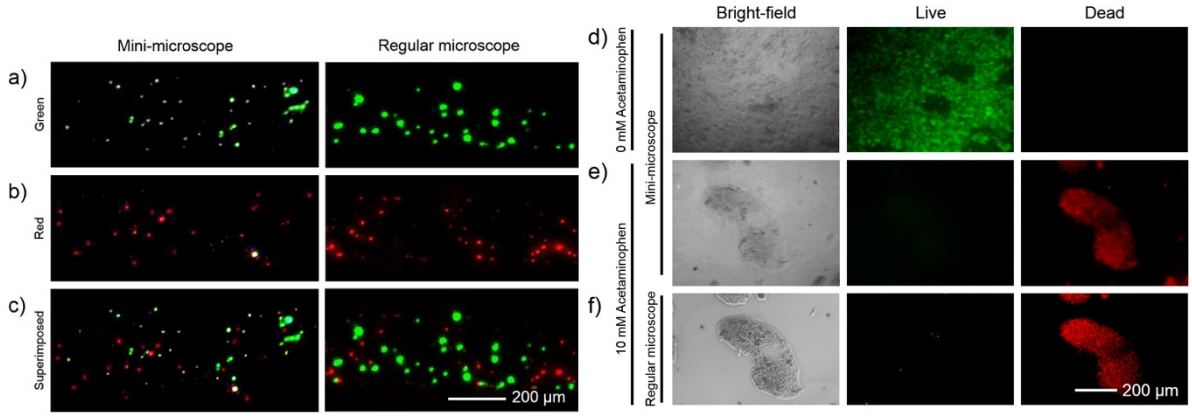

Figure 4.4 – a-c) Dual-channel fluorescence imaging with the mini-microscope and the bench-top microscope (Nikon Eclipse) for (a) green fluorescent and (b) red fluorescent beads; superimposed images of the two channels are indicated in (c). d, e) Mini-microscopic images of live/dead staining results showing HepG2 cells non-treated or treated with 10 mM acetaminophen for 24 h in the liver bioreactors. f) Bench-top microscope (Zeiss Axio Observer D1) image showing the same cell colony as in (e), indicating the accuracy in the detection of the live/dead cells using the mini-microscope.

4.3.3 Dual-channel fluorescence imaging with mini-microscope

We next examined the capability of the fluorescent mini-microscope to simultaneously detect green and red fluorescence signals. We co-infused polystyrene beads labelled with fluorescein isothiocyanate (FITC) and rhodamine into a microfluidic channel. The mixture of the beads was then subjected to imaging under both the mini-microscope and a bench-top

microscope (Nikon Eclipse Ti-S). It was clear that the mini-microscope could obtain images of the beads with green and red fluorescence, clearly differentiating the two types from a mixture (Figure 4.4, a-c, left panel). Significantly, the images captured using the mini-microscope were comparable with those from the bench-top microscope (Figure 4.4, a-c, left versus right panels), revealing the strong fluorescence capacity of the mini-microscope.

4.3.4 Drug toxicity assessment of liver-on-a-chip with fluorescence mini-microscope

To further assess the usability of the fluorescence mini-microscope to track cellular events we performed a cytotoxicity Live/Dead assay. HepG2 cells in a liver bioreactor were treated with 10 mM acetaminophen for 24 h to induce cell death and subsequently stained with a Live/Dead kit. For fluorescence analysis, images were acquired using a blue and a green LED as excitation sources, for emissions in the green (live cells) and red (dead cells) channels, respectively. Filter-free color separation was performed as described above to separate the excitation and emission images. Without any drug administration, we could clearly image cells in green (live cells) with essentially no dead cells present (Figure 4.4d). At 24 h post administration of acetaminophen massive cell death was observed in red (Figure 4.4e) with the mini-microscope. The images were compared with those obtained using a bench-top microscope (Zeiss Axio Observer D1), which exhibited similar results (Figure 4.4f). We proved with this experiment that our fluorescence mini-microscope could be used to assess cell viability *in situ* to screen cytotoxic drugs in an organs-on-a-chip platform.

4.3.5 Dynamic examination of liver- and heart-on-chips

The dynamic behaviors of the tissues/organoids in an organs-a-chip platform is a major parameter in assessing their viability and functionality. For example, the attachment, proliferation, and migration of cells in a bioreactor is highly dependent on the local microenvironment, including the supply of nutrients/oxygen, the fluid shear stress, and the administration of pharmaceutical compounds (289-291). This is particularly true for heart-on-

chip applications, where beating of the cardiac tissues indicates not only the viability but also the functionality of the organoids (292, 293). While the beating rate stays constant for the cardiomyocytes under normal conditions, it is easily diminished when an external stimulus is introduced into the system, such as mechanical disturbance or change in temperature. The sensitive nature of these cells further emphasizes the necessity of integrating a miniaturized microscope that can be directly fitted underneath the bioreactor for long-term monitoring of undisturbed responses. The need is enhanced by the dependence and relation of beating rate of cardiomyocytes with drug treatments (293, 294).

We first demonstrated the capability of our mini-microscope to follow the dynamic processes of simplified heart- and liver-on-a-chip models. HepG2 cells were seeded onto the bottom of the microfluidic bioreactor at a density of approximately 1000 cells mm^{-2}. The culture was maintained at a flow rate of 200 µL h^{-1}. Mini-microscope was fitted at the bottom of the hepatic bioreactor for continuous observation. As shown in Figure 4.5, a-d, HepG2 cells started to aggregate from time zero, and when compact structures of cell aggregates were formed they began to proliferate, well matching the reported motility and growth pattern of the cells (295, 296). We then cultured NIH/3T3 fibroblasts in another bioreactor and monitored their migration. Again, the mini-microscope demonstrated a very high resolution and could efficiently follow the motility of individual cells over a period of 2.5 h tested.

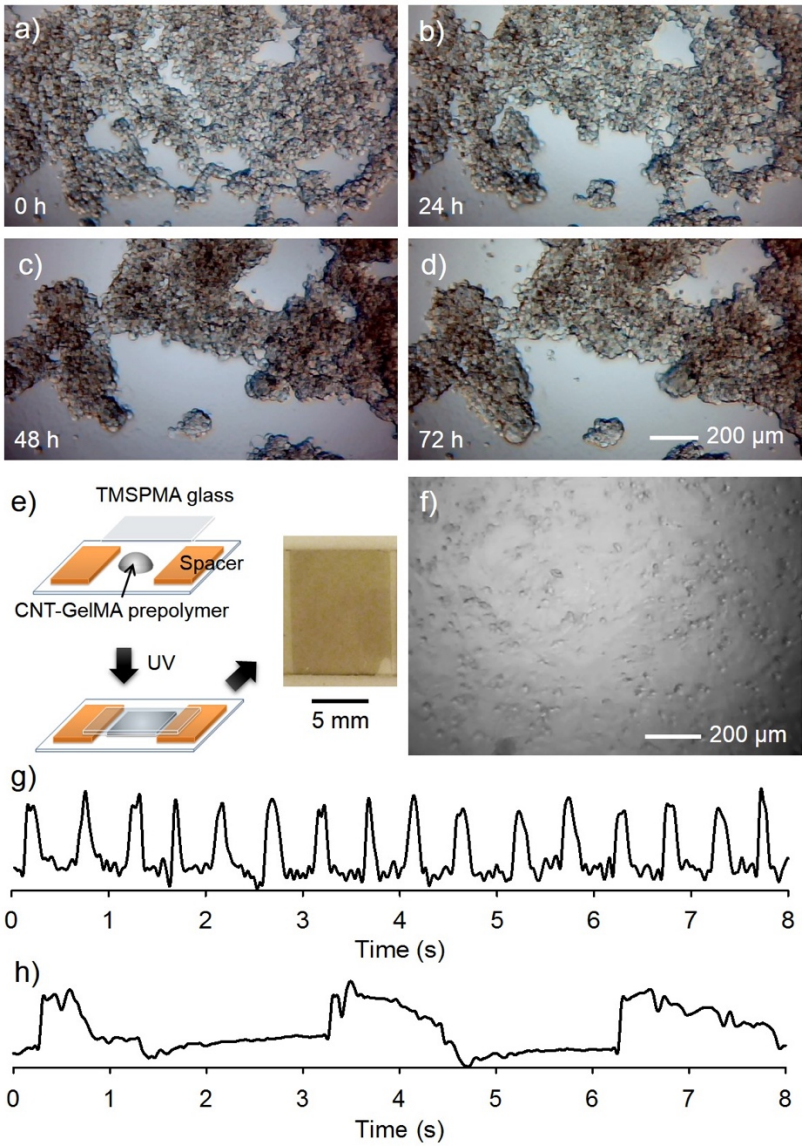

Figure 4.5 – a-d) Time lapse mini-microscopic images showing the migration of HepG2 cells at the bottom of the bioreactor over a course of 72 h. e) Schematic and photograph showing the preparation of a glass substrate coated with GelMA-CNTs for cardiomyocytes culture. f) Mini-microscopic image showing rat neonatal cardiomyocytes seeded onto the substrate and embedded in the chamber of the bioreactor at Day 5. g) Real-time measurement of cardiomyocytes beating *in situ*, using custom-coded MATLAB program with the bioreactor-integrated mini-microscope. h) Measurement of cardiomyocytes beating using a bench-top microscope after the cardiac bioreactor was removed from the incubator for 30 min.

The heart is a vital organ in the body that functions as a biological pump to circulate the blood among all organs in the body. Heart-on-a-chip provides a viable platform for not only studying the biology but also screening cardiotoxic pharmaceutical compounds (292, 293, 297). Here we built a cardiac bioreactor to evaluate the capability of the mini-

microscope to analyze the beating of the heart-on-a-chip (Figure 5e). A mixture of GelMA prepolymer and CNT was sandwiched between two glass surfaces spaced at 1 mm and UV-cured. Cardiomyocytes were then seeded on top of the substrate to form a confluent cell sheet mimicking the myocardium. In this case, CNTs were incorporated into the GelMA matrix in order to enhance the intercellular communication between the cardiomyocytes, promoting their functionality (287, 298). Figure 4.5f shows a bright-field image of the cardiomyocytes in the bioreactor, revealing the morphology of the cardiac tissue. The mini-microscope was able to continuously record the beating of the cardiac tissue, which could further be analyzed in real-time using custom-written MATLAB program based on an intensity or pixel-shift method (Figure 4.5g). Beating of the cardiomyocytes in the heart-on-a-chip platform was monitored for up to 3 days without any disturbance and the cells maintained stable beating over the entire course of observation. In contrast, when using the conventional bench-top microscope where the cardiac bioreactor was required to stay exposed to a decreased temperature for an extended period of time and/or under mechanical disturbance, the cardiac tissues demonstrated a slowed or irregular beating rate (Figure 4.5h), greatly interfering with experimental observations of cardiac behaviors when potentially altered beating patterns are expected upon drug treatment.

4.4.6 Fluorescence mini-microscope-based oxygen sensor

Besides imaging cellular structures, measurement of the physical microenvironment of the platform is equally important in an organs-on-a-chip platform (299). These physical parameters, including but not limited to pH value, oxygen level, temperature, and osmotic pressure, all contribute to maintaining the homeostasis of the system and normal functionality of the embedded organoids. Among these parameters, the oxygen level is critical as it strongly depends on organ type and tissue architecture (266, 300). Detection of oxygen levels in a microfluidic device and particularly oxygen consumption within the organoids however, is challenging. Conventional approaches such as those based on electrochemistry (301), are not suitable due to strong interference caused by proteins and

small molecules secreted by cells that lead to rapid biofouling of the sensor surfaces. Optical oxygen sensors are convenient and barely affected by biofouling (302-305), but the methods using bench-top microscopy does not allow *in situ* measurements based on compact devices. Here again, we proved that our fluorescence mini-microscope could be a versatile tool as an oxygen sensor for measurement of intra-organoid oxygen levels in a liver-on-a-chip platform.

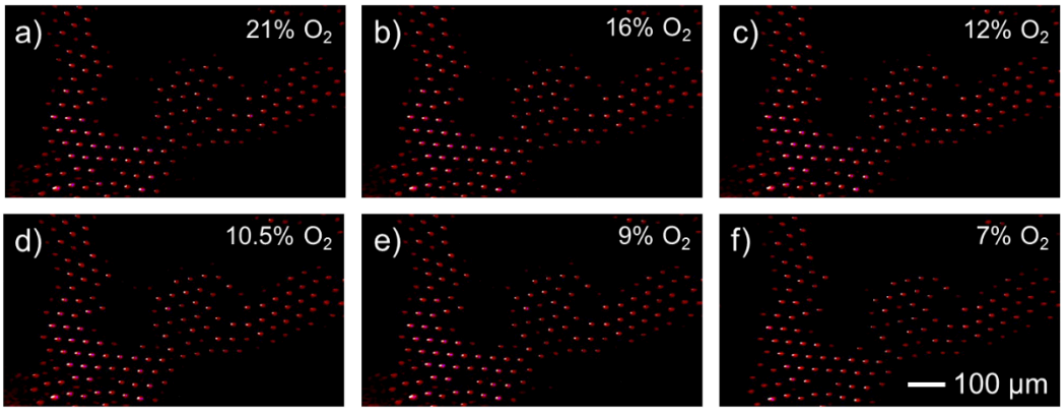

Figure 4.6 – Fluorescence images obtained from the mini-microscope showing no difference in fluorescence intensity of beads at different oxygen concentrations using the Nile Blue channel.

Oxygen-sensitive PDMS microbeads were fabricated using a microfluidic device following our recently developed protocol (Figure 4.7a). The PDMS microbeads had a uniform diameter of 30 µm (Figure 4.7b), which could be well dispersed inside an organoid for microscopic observation. The microbeads were then doped with two fluorescent dyes, the oxygen-sensitive ruthenium dye and the inert, oxygen-irresponsive Nile Blue. While the fluorescence intensity of ruthenium is inversely proportional to the oxygen concentration (i.e. its fluorescence is quenched by oxygen molecules), that of Nile Blue is independent on oxygen and would serve as the internal control. In this case, a single piece of high-pass filter of >610 nm (common emission for both dyes) was inserted underneath the bioreactor to improve the sensitivity of the imaging compared to the filter-free approach. In addition, two programmed excitation LEDs were fitted on the top of the bioreactor: 455 nm for exiting ruthenium, and 591 nm for excitation of Nile Blue. Calibration curves were obtained using the setup in the absence of organoids (Figure 4.7c). It was clear from both the calibration curves

and the mini-microscopic image that, the fluorescence intensities of ruthenium followed an exponential decay from 7-21% oxygen (Figure 4.7, d-i), whereas those of Nile Blue remained constant over the range (Figure 4.6).

We then embedded the oxygen-sensitive PDMS microbeads inside a liver organoid prepared by UV-crosslinking a GelMA spheroid encapsulating a mixture of HepG2 cells and the beads, at the bottom of a liver bioreactor; another layer of GelMA containing only the beads then encased the core (Figure 4.7j). The system was maintained in a perfusion culture at a flow rate of 200 µL h^{-1} for 24 h. Individual cells were also clearly discernible in the image captured by the mini-microscope under bright-field (Figure 4.7k). Mini-microscope images were further taken at both ruthenium channel and Nile Blue channel, and oxygen intensities of beads at different locations were recorded (Figure 4.7l) to calculate their respective oxygen levels based on the calibration curves.

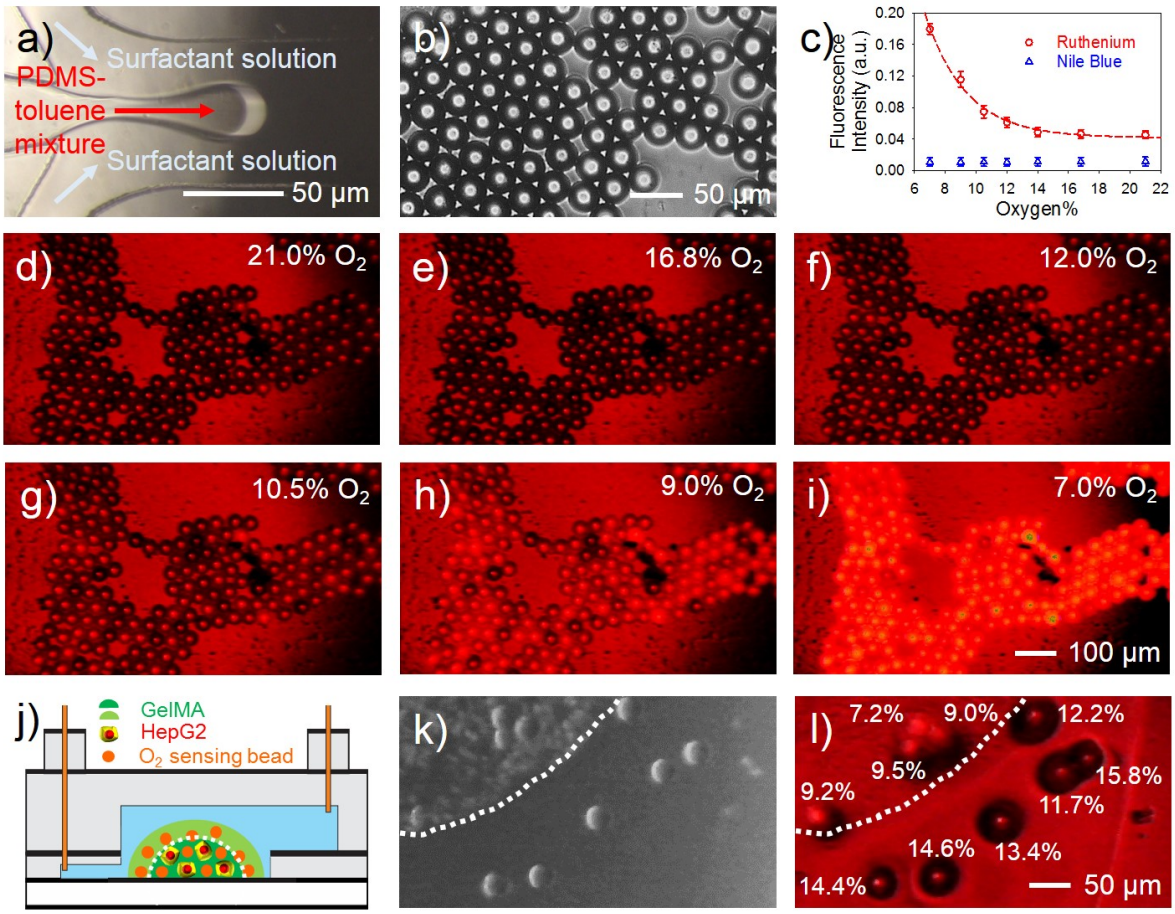

Figure 4.7 – a) Microfluidic device to fabricate uniform PDMS microspheres. b) PDMS microbeads fabricated by the microfluidic device and infiltration of ruthenium dye to produce oxygen-sensitive

beads. c) Calibration curve showing fluorescence intensity versus oxygen concentration. d-i) Fluorescence images obtained from the mini-microscope showing beads at different oxygen concentrations. Ruthenium channel was used for imaging. j) Schematic diagram showing the setup for real-time sensing of oxygen levels in a liver bioreactor. k, l) Bright-field and fluorescence images showing the cells and the oxygen sensing beads at 24 h post seeding.

As expected, in the core of the liver organoid the oxygen level dropped significantly to only <10%, with a trend of less oxygen towards the core and more along the periphery. By comparison, in the outer layer of the hydrogel where no cells were present, the oxygen levels were much higher ranging from 12-16%. Such capability of the mini-microscope combined with oxygen-sensing beads have provided a unique opportunity for convenient investigation of the intra-organoid oxygen consumption in an organ-on-a-chip platform, particularly useful for complex organs where multiple cells types are involved. Due to the compact size of the mini-microscope and its easy integration with microfluidic platforms, many other applications in biosensing are also potentially feasible, such as inclusion of multiple modules to monitor oxygen levels up- and downstream of each bioreactor.

4.4 Conclusions

We have designed and fabricated a portable miniature microscope from off-the-shelf components and webcam, which had built-in multi-color fluorescence capability to follow cell motility, analyze cell/tissue viability, and as optical sensors to measure biophysical properties of the microenvironment such as oxygen levels inside organoids based on an oxygen-sensitive fluorescent dye. The mini-microscope has adjustable magnifications of 8-60X, a high resolution of <2 μm, and a long working distance of 4.5 mm (at 8X). The cost of the mini-microscope barely exceeds $9, and the modular design allows ready integration with a wide variety of pre-existing platforms including for example, petri dishes, cell culture plates, and microfluidic bioreactors. We believe that our fluorescence mini-microscope can likely replace the conventional bench-top microscopes in several biomedical applications where long-term *in situ* and high-throughput imaging capacity is required for investigations such as drug screening in organs-on-a-chip systems.

CHAPTER V

CONTROLLING ORGANS-ON-CHIP

Adapted from Yu Shrike Zhang, João Ribas, et al., and Ali Khademhosseini, “Google Glass-Directed Monitoring and Control of Microfluidic Biosensors and Actuators”, Scientific Reports, 6: 22237 (2016).

Ribas devised the concept with Zhang, Ribas wrote the paper, Ribas performed experiments to create the system together with Julio Aleman and Fabio Busignani. Sensors were provided by a collaborator.

CHAPTER V – Controlling organs-on-a-chip

5.1 Introduction

Accurate monitoring and control are key aspects in generating and collecting biological data, from morphology to physiology and respective responses to stimuli. Advancements in the past decades have led to the development of a variety of high-precision biosensors and actuators for unprecedented biomedical applications (306-310). Particularly, the recent advancements in combining them with microfluidic devices have garnered tremendous attention due to their capability of low-volume analysis, high-throughput fluid handling, and miniaturization (262, 311, 312). For example, microfluidic bioreactors have been fabricated to mimic the human physiological system, termed as the organs-on-a-chip platforms (264-269, 271-276, 300, 313). These platforms predict physiological responses with high accuracy, and typically encompass a set of finely designed microfluidic organoid modules interconnected together (313, 314), pneumatic-driven valves (307-310) and biosensing units (299, 315). However, they generally require frequent, on-demand monitoring and control, since the observation period can last from hours to weeks (23, 276, 299).

The use of conventional desktop computers limits the user mobility and data accessibility, slowing down data-driven decision-making processes, especially problematic when monitoring over extended periods of time. Recent advances in mobile technologies such as smartphones and tablets (316-327), and especially new wearable devices such as bands and smart watches (328-330), have paved an entirely new avenue for fulfilling these tasks in a much more flexible and remote manner, greatly reducing the labor effort and improving data accessibility. Among all, the Google Glass accounts for one of the most promising smart device concept, relying on a hands-free computing system with accurate voice control and imaging capabilities to enable on-the-fly human-machine interactions. The built-in wireless functions (Wi-Fi and Bluetooth) potentiate mobility by connecting directly (Wi-Fi) or indirectly (*via* Bluetooth-paired smartphone/tablet). These advantages have proven the Google Glass useful for a range of biological/biomedical applications including plant disease detection (331), remote surgical communications and image-guided surgery (332), diabetes

management (333), and point-of-care diagnostics (334).

Here, we demonstrate a Google Glass-directed monitoring and control of microfluidic biosensors and actuators using a set of integrated sensors, hardware, software, and Glassware. Using a liver- and heart-on-a-chip systems as a model platform, we demonstrate seamless transmission of biosensor data onto the Google Glass for on-demand visualization and analysis of *i*) temperature and pH values, *ii*) microscopic observations (*e.g.* morphology of liver/cardiac organoids and video of beating cardiac organoids), and *iii*) on-Glass analysis (*e.g.* beating rate). Moreover, we showed our capability to selectively actuate microfluidic pneumatic valves and reservoirs to study the effects of pharmaceutical compounds on liver organoids in a primary human liver-on-a-chip platform. The Glass might be of particular importance in cases where the experimental conditions threaten human life, as when researchers work with highly contagious bacteria and virus or radioactivity. We believe that our Google Glass-based platform for monitoring and control will find widespread applications in the laboratory and may be further expanded to healthcare and environmental analysis where telemetry, remote control, and on-demand human-machine interactions are required in a safer manner.

5.2 Materials and Methods

5.2.1 Microfabricated temperature and temperature sensors

The passive chip was microfabricated in Switzerland with a two-mask process flow. Silicon wafers with a layer of native oxide 500 nm in thickness were used as the substrate. The metallization of the wafers was achieved by first evaporation of 10 nm of titanium (Ti) as the adhesive layer, followed by 100 nm of Pt on top of Ti. Passivation of the metal was performed *via* atomic layer deposition of Al_2O_3 of 20 nm in thickness (335). The pH sensor was functionalized by electrodeposition of IrOx onto the microelectrode, which was carried out by applying a constant current density of 0.15 mA cm^{-2} for 80 min in a solution of IrOx (336). The pH was measured by reading the open circuit potential produced by the electrodes using a potentiostat (CHI684, CH instruments) and an external Ag/AgCl reference

electrode (ET072-1, eEAQ). Temperature sensing was achieved by reading the sensor resistance using a precision source meter (B2901A, Agilent).

5.2.2 Software and Glassware

The Google Glass Explorer Edition was used in this project, and programmed using the Glass Development Kit in Java. The embedded Linux board BeagleBone Black was programmed in C++ and bash command. The OpenCV was used to calculate the beating rate of cardiomyocytes and cURL library was used to performing http *post* and *get* operations to the Google App Engine. The project used the cloud-based Google App Engine, programmed in Python, and local video storing performed using the Qt framework.

5.2.3 Design of printed circuit board (PCB)

A custom made PCB was designed using the National Instruments Circuit Design Suite, to accommodate the pH/temperature multisensor and the electrovalves driver and made to be attached on the headers of the BeagleBone Black. A conditioning circuit for both pH and temperature sensors was designed to provide noise filtering with a low-pass filter. Additionally, the pH circuit performed a signal level shift, due to the fact that the pH sensor signals are bipolar. To drive the electrovalves (normally open; MH1-A-24VDC-N-HC-8V-PR-K01-QM-AP-BP-CX-DX, Festo), a specific circuit was designed with a low-side switch metal-oxide semiconductor (MOS). A DC-DC converter circuit was designed to provide the compatibility with both 24V and 12V solenoid valves, and a relay circuit (voltage supply switch) provided the switch between these. Circuit designs followed the guidelines for reduced electromagnetic interference.

5.2.4 Mini-microscope

The mini-microscope was built according to the previous chapter.

5.2.5 Liver- and heart-on-chips

Re-usable and re-sealable microfluidic bioreactors based on polydimethylsiloxane (PDMS, Dow Corning Sylgard 184, Ellsworth) were fabricated by modifying our recently developed protocol (313). Specifically, the bioreactors had a double-layer configuration with the inlet and organoid chamber at the bottom and outlet on the top layer. The two PDMS layers could be disassembled for seeding the organoid, following which sealing were achieved by clamping the pieces using a pair of PMMA structures tightened by sets of screws/bolts. HepG2 human hepatocellular carcinoma cells (HB-8065, ATCC) were seeded onto the bottom of the bioreactors at a density of 2000 cells mm^{-2}. Cultures of the organoids were maintained at a constant flow rate of 200 µL h^{-1} in a Dulbecco's Modified Eagle's Medium (DMEM, Life Technologies) supplemented with 10 vol.% fetal bovine serum (FBS, Life Technologies) and 1 vol.% penicillin-streptomycin (P/S, Life Technologies). Primary human hepatocytes (HUCPI6, Triangle Research Labs, Research Triangle Park, NC) were seeded in a PDMS model containing arrays of 200-µm wells. To maintain the high cell viability, the hepatocyte growth media (Lonza) was replaced every 48 h. At Day 5 the spheroids were harvested and mixed with an aqueous solution containing 10 w/v% GelMA and 0.5 w/v% photo initiator Irgacure 2959 (Ciba, Hawthorne, NY). GelMA droplets with approximately 1 mm in size were bioprinted in the bioreactor chamber using a NovoGen MMX bioprinter (Organovo, San Diego, CA). After 17-s of UV exposure at 850 mW at a distance of 8.5 cm, the GelMA dots were successfully crosslinked to the bottom of the bioreactor. When necessary, APAP was introduced into the bioreactor at a concentration of 15 mM. Cardiac bioreactors were constructed as described in the previous chapter The constructs were subsequently transferred to the chambers of the bioreactors and perfusion-cultured at a flow rate of 200 µL h^{-1}.

5.3 Results and Discussion

5.3.1 Hardware, software, and Glassware for data transmission

Wearable devices allow us to interact in new ways with data and enable us to take

fast decision-making actions. When designing such wearable technological solutions, it is ideal that the interaction is a two-way process – one should be able to see new data and take appropriate action through the wearable that translates into tangible changes in the system. With this aim, we designed a Glassware solution to monitor and control microfluidic and organs-on-a-chip systems, aided by a set of custom-developed hardware and software.

The Google Glass communicates with the sensors *via* the Google App Engine (Figure 5.1A). Data is stored in the Google Cloud, and the Glass periodically checks for new sensor data, such as the latest video of cardiomyocyte beating. A custom-built printed circuit board (PCB) shield interfaces the sensors and the actuators (electrovalves) to an embedded Linux board (BeagleBone Black). This board was chosen for its low-cost, powerful processor, and high number (in total 92) of pins that allow the connection of multiple sensors and controllers. Furthermore, the board, programmed using C++, uses the Open Source Computer Vision (OpenCV) library to plot beating patterns from cardiomyocyte videos, following our previously published work on the pixel-shift method (281, 337). To transmit data from the Beagle Bone to the Google App Engine we used the cURL library with simple *http post* and *http get* operations.

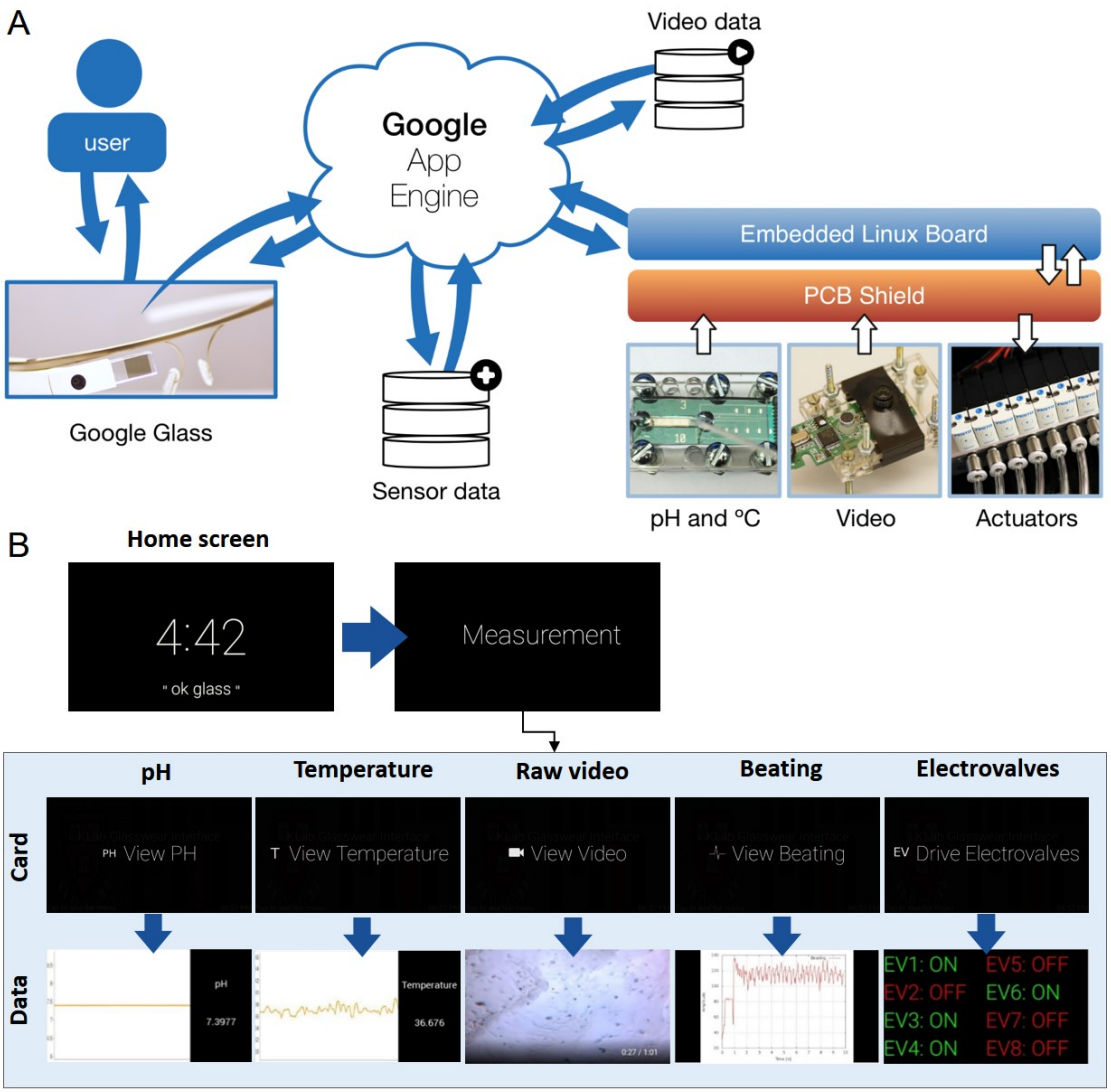

Figure 5.1 – Principle of Google Glass-directed monitoring of sensor data and control of actuators. (**A**) Scheme of the interactions between the Google Glass and the hardware and software components. (**B**) Diagrams showing the operation procedure on the Google Glass. Upper panel shows the home screen, which upon voice control ("ok glass") or tapping brings out the custom card Measurement and enters the application; lower panel shows a series of live cards can then be reached by swiping. Tapping on each card shows the corresponding measurement data, beating analysis, or the control card for the electrovalves.

The voice control command ("ok glass") gives the users access to the designed Glassware custom card (Measurement, Figure 5.1B). Once the Glassware is launched, a set of live cards can be accessed via swiping, giving the user access to view the pH and temperature values, a video of the cells and a plot of the beating patterns (Figure 5.1B, bottom panel). Additionally, the user has access to a live card that controls electrovalves,

which can control the flow direction and addition of drugs in the microfluidic system. For the electrovalves a driver circuit was specifically designed to meet their voltage and current needs, and was controlled *via* digital output signals from the BeagleBone board. We have also designed custom circuits for temperature and pH sensors in order to amplify the signals and reduce the noise of the sensors.

Overall, the sensor data is stored in the Google App Engine, and retrieved whenever the Glassware application is started and then periodically. Video files are also stored locally in a computer, so that data from any different time-point can be retrieved when needed. To actuate the different electrovalves, the Google Glass changes the status (on/off) of each one in the Google App Engine, and the Linux board periodically checks for these status and makes concordant changes. Together, the developed platform allows the Glassware to update the user on data coming from the sensors and allow the user to taking action through the control of electrovalves.

5.3.2 Physical sensing units for real-time temperature and pH monitoring

Microfabricated sensors were obtained using our published miniaturized approach (338). Figure 5.2A shows a schematic of the sensor array measuring 2.2 x 15 mm^2, which hosts five biosensor platforms, a temperature sensor, and a pH electrode. The entire sensor array was fabricated from biocompatible materials and integrated with a complementary metal-oxide semiconductor (CMOS) chip for measurements. As a proof of principle, we chose to only probe the temperature and pH responses of the sensor array to characterize the physical microenvironment of our system. The right panel in Figure 5.2A indicates a magnified view of the temperature and pH sensing units of the sensor array, where the T sensor consisted of a platinum (Pt) zigzagging path of 0.02 x 16 mm^2 for each turn. Pt was chosen due to its linearity within the physiological temperature range and higher resistivity, which efficiently confined the size of the sensor to a small footprint (339). The pH sensor was consisted of a 250-μm^2 metal pad that was electrodeposited with a thin film of iridium oxide (IrOx). Changes in the pH of the surrounding medium were measured by open circuit

potential of the electrode (340, 341). To achieve continual monitoring of the microenvironment, the sensor array was enclosed in a microfluidic device, with a 3 x 15 x 0.2 mm^3 chamber placed directly on top of the sensing units, resulting in a small working volume of <10 µL (Figure 5.2B). Calibration curves for temperature and pH utilizing the enclosed microfluidic device show a linear correlation, and a sensitivity of 3.6 Ω $ºC^{-1}$ and -67.9 mV pH^{-1} at the flow rate of 200 µm h^{-1} (Figure 2C-D).

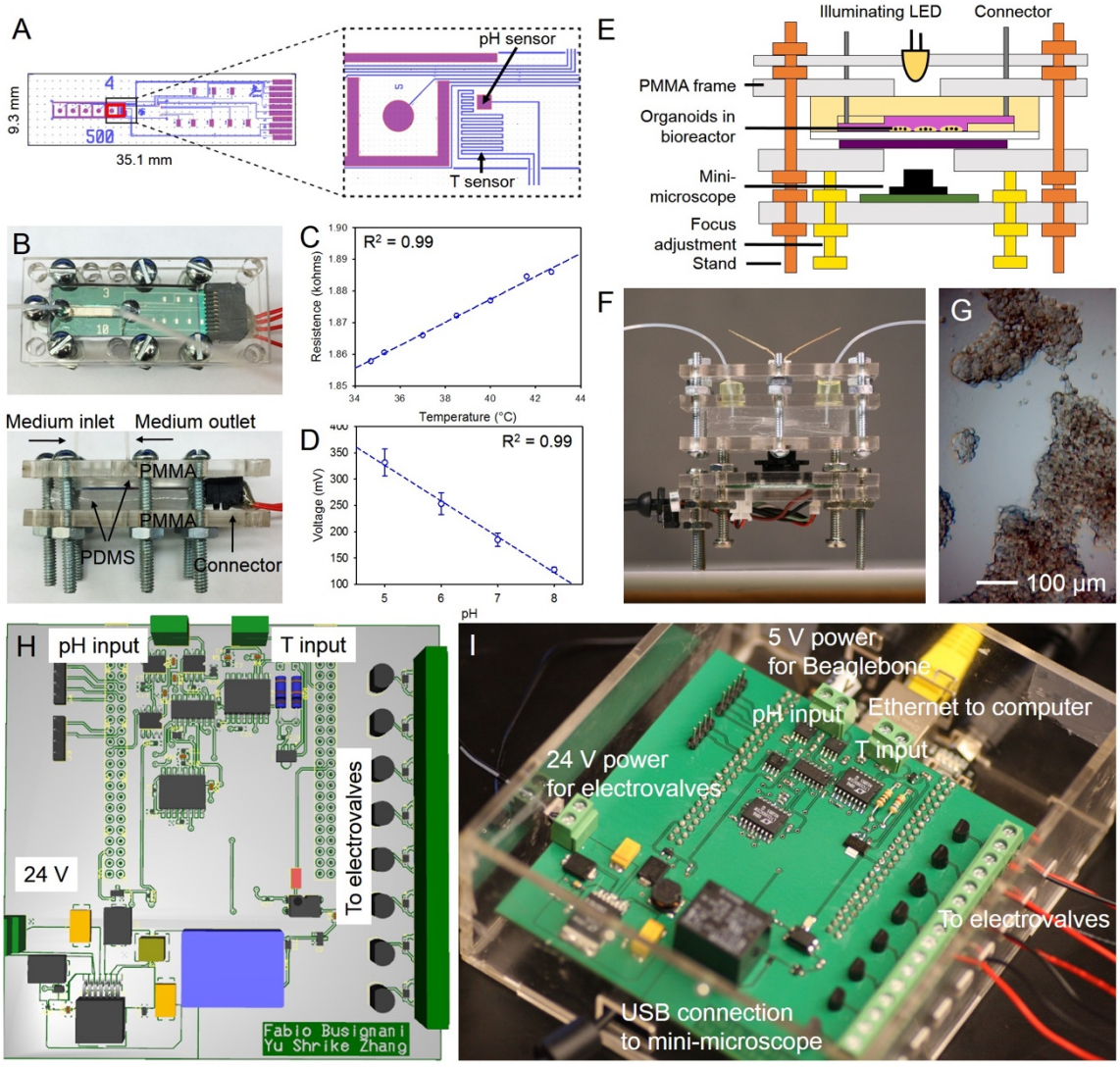

Figure 5.2 – Biosensors and hardware for data recording, transmission, and command control. (**A**) Schematic showing the microfabricated biosensor chip containing T sensor, electrochemical pH sensor, and immunosensor array. (**B**) A microfluidic device hosting the biosensor chip for continuous sensing. (**C**,**D**) Calibration curves for T and pH sensors, respectively. (**E**,**F**) Schematic and photograph showing the mini-microscope. (**G**) Resolution testing of the mini-microscope. (**H**) Schematic showing the design of the electronic circuit for T/pH reading from the sensor and controlling electrovalves. (**I**) Photograph showing the assembled platform of the electronic circuit (top) and a Beaglebone board

(bottom) for simultaneous reading of the sensor data, communication with the mini-microscope, and control over electrovalves.

We further integrated a miniature microscope that we have recently developed for image and video acquisition (281, 285, 337). The microscope was fabricated from a webcam and off-the-shelf components (337). Figure 5.2E-F show a schematic and a photograph of the mini-microscope integrated with a microfluidic bioreactor, respectively. The imaging unit was constructed by flipping the webcam lens and re-attaching it to the CMOS sensor in order to achieve magnification rather than the de-magnifying mechanism that a webcam requires (337). This imaging unit was fit on a set of poly(methyl methacrylate) (PMMA) frames sandwiched by screws/bolts and the microfluidic bioreactor placed above the sensor. A mini-microscope image of HepG2 cells in a liver bioreactor is shown in Figure 5.2G, where individual cells could be observed, highlighting the high resolution of the mini-microscope.

In order to transmit the data to the Google App Engine a custom PCB board was designed to accommodate the BealgeBone Black for connection with the pH and temperature sensors as well as the mini-microscope (Figure 5.2H-I). The micro-computing unit then records the data and image/videos and constantly transmits them remotely to the Cloud for the Glass to fetch and display.

5.3.3 Remote monitoring of liver- and heart-on-a-chip platforms

To test the capability of our Google Glass system for visualizing sensor data we monitored liver- and heart-on-a-chip platforms. The multi-layer microfluidic bioreactor was fabricated following our recently published protocol (Figure 5.3A-B) (313), where the bioreactor chambers are made of polydimethylsiloxane (PDMS). The bioreactor was designed to be re-usable and re-sealable, providing easy access to seeding cells or placing organoids inside the chamber. To construct the liver bioreactor we seeded HepG2 cells in the bottom chamber at a density of approximately 1000 cells mm^{-2}. The mini-microscope was fitted at the bottom of the culture chamber for continuous monitoring of cell behavior. The images acquired from the mini-microscope were successfully transmitted to the Google

Glass wirelessly and visualized in the View Image Live Card (Figure 5.3C). The mini-microscope images can be acquired at a pre-set time interval and saved locally on the computer. Importantly, the latest acquired image is wirelessly transmitted to the Google Glass, where it then refreshes the Live Card for visualization. This feature enables the user to remotely access the microscopic images of the organoids in the bioreactors and monitor their morphological changes as a function of time.

However, in many cases, static images cannot be used to follow and measure fast dynamic cellular behaviors. We next demonstrated the capability of the Google Glass to simultaneously visualize and analyze mini-microscope videos using a simplified heart-on-a-chip platform. Heart-on-a-chip provides a versatile approach for studying the biology, physiology, as well as screening pharmaceutical compounds possessing cardiotoxicity (23, 292, 293). The heart-on-a-chip platform was constructed by seeding rat neonatal cardiomyocytes on a piece of glass coated with a thin layer of 5 wt.% gelatin methacryloyl (GelMA) and 1 mg mL^{-1} carbon nanotubes (CNTs), followed by placement of the construct in the chamber of a cardiac bioreactor (Figure 5.3D). CNTs were embedded into the GelMA to promote the intercellular connections among the cardiomyocytes, therefore improving the functionality of the fabricated cardiac organoids (287, 298). Figure 3E is the View Image Live Card showing a mini-microscope image of the cardiomyocytes in the cardiac bioreactor transmitted to the Google Glass, indicating the formation of a confluent layer of cardiomyocytes on the GelMA/CNTs substrate.

Neonatal cardiomyocytes beat synchronously, but the beating frequency and pattern can be disturbed easily by administration of drugs/toxins or by changing the surrounding microenvironment (*e.g.* temperature). We therefore performed two sets of experiments to perturb the regular beating of the cardiac organoid in the heart-on-a-chip device. We first opened the incubator door for 10 min to allow the temperature to drop from 37 °C to 27 °C, and then closed it back. The temperature sensor detected the drop in real-time (Figure 5.3F), and the data was transmitted *via* the integrated system to the Google Glass and visualized in

the View Temperature Live Card. The temperature data was consistent with that collected by a commercial sensor directly connected with a National Instruments data acquisition (NI-DAQ) card and LabVIEW (Figure 5.3G), highlighting the accuracy and time responsiveness of the sensor data transmitted to the Google Glass. The beating of the cardiac organoid was

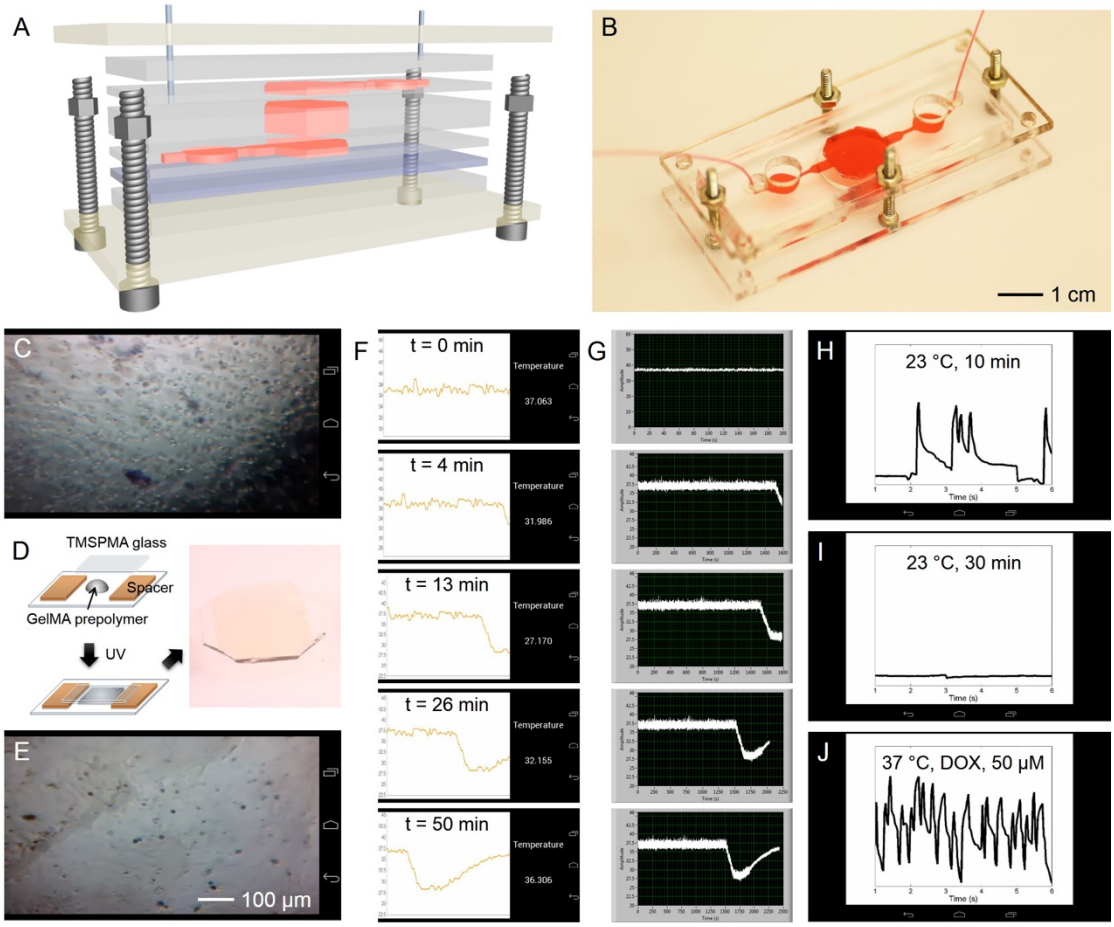

Figure 5.3 – Real-time monitoring of organoid behaviors in an integrated liver-and-heart-on-a-chip platform on Google Glass. (**A**, **B**) Schematic and photograph showing the resealable microfluidic bioreactor. The mini-microscopes were fitted at the bottom of the bioreactors while the biosensor unit was placed downstream of the bioreactors. (**C**) Google Glass view obtained from the mini-microscope fitted underneath the liver bioreactor showing the morphology of HepG2 cells. (**D**) Schematics showing the fabrication process of a GelMA substrate for constructing the cardiac tissue. The cardiac tissue was then transferred into the cardiac bioreactor. (**E**) Google Glass view obtained from the mini-microscope fitted underneath the cardiac bioreactor showing the morphology of rat cardiomyocytes. (**F**) Temperature sensing data visualized on the Google Glass, where the door of the incubator was opened for 10 min and then closed. (**G**) The same data was recorded on a LabVIEW program, indicating the same trend and accuracy of the data transmitted onto the Google Glass. (**H-J**) Beating analysis on the Google Glass of the cardiomyocytes under different conditions: (**H**) 23 °C for 10 min; (**I**) 23 °C for 30 min; and (**J**) 37 °C post treatment of DOX for 1 h.

monitored during the external manipulation of the temperature, recorded using the mini-microscope and the video wirelessly transmitted to the Google Glass. When the heart-on-a-chip temperature decreased to 23 °C, even for only 10 min, the cardiomyocytes showed an irregular and reduced beating rate, which was analyzed and plotted on the Google Glass in the View Beating Live Card (Figure 5.3H). Furthermore, when the cardiac bioreactor was completely removed from the incubator and cooled to room temperature for over 30 min, the cardiomyocytes completely ceased beating (Figure 5.3I). Alternative to changing environmental conditions, the beating of the cardiac organoid was also tested by addition of cardiotoxic drugs. We infused the heart-on-a-chip with 50 μM of doxorubicin (DOX) for 1 h at 37 °C and monitored the beating. DOX, an anti-cancer drug with adverse side effects on cardiac tissue, was shown to induce acute arrhythmia of the cardiac organoid upon treatment at high doses (Figure 5.3J) (23, 281, 294, 342).

The integrated BeagleBone board and software/Glassware sets allowed the data from the microfabricated sensor, as well as still images and videos recorded by the mini-microscope, to be visualized and transmitted wirelessly to the Google Glass. The sensing capabilities of our system deepen with real-time analysis and concomitant visualization in the Google Glass. Importantly, the data were simultaneously recorded locally (on the computer where the BeagleBone board was connected), facilitating on-demand retrieval of the data at any time. In addition to organoids in bioreactors, a range of other static images or dynamic videos such as micropatterns and microfluidic droplet generation could also be remotely monitored in real-time using the Google Glass (Figure S5.1).

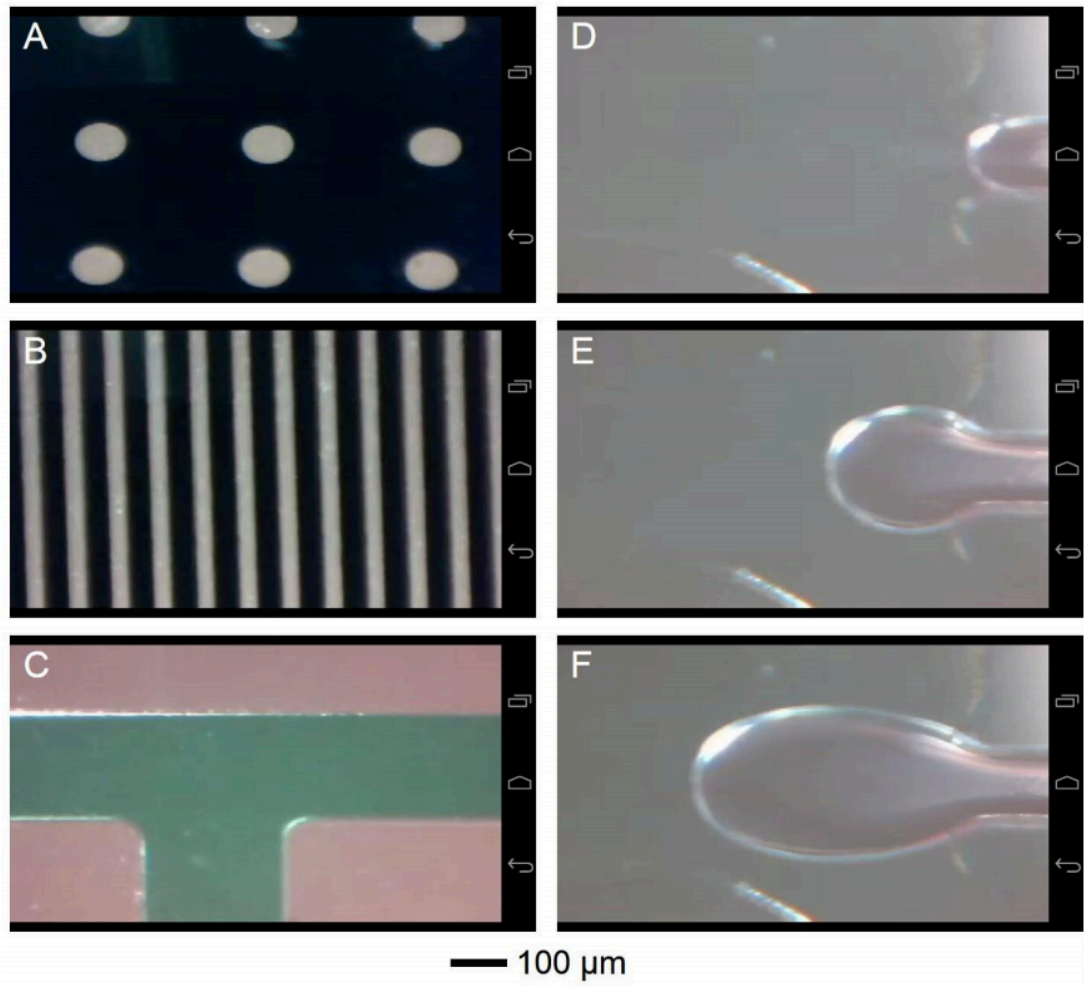

Figure S5.1 – Display of mini-microscopic observations on the Google Glass of A) a mask with dot arrays, B) a mask with line arrays, C) a T-shaped microfluidic channel filled with food dye, and E-F) sequential screenshots showing the formation of an aqueous droplet in oil in a microfluidic device.

5.3.4 Remote control of actuators using Google Glass

Actuators play a pivotal role in microdevices, functioning as gating mechanisms for controlling a variety of devices based on electricity and mechanics (343, 344). For example, electrovalves are a category of electrically actuated valves that allow for opening and closure of pressure-driven valves that can be used to conveniently manipulate liquid flows inside a microfluidic device. Here we have developed a remote control platform where the BeagleBone board reads the wirelessly transmitted Google Glass commands and responds to actuate the electrovalves (Figure 5.1A). The Glassware application has a set of Live Cards that allow turning on and off each electrovalve switch upon command (Figure 4A). Selection

of the “Drive Electrovalves” Card enables a list of eight valves in the screen of the Glass; upon swiping of the touch pad eight Live Cards will be sequentially shown, each of which can be individually triggered. To visually show the working concept, we prepared an array of eight LEDs connected to the outputs on the BeagleBone board (Figure 5.2H-I). As shown in Figure 4B-E, when the switches were selectively activated on the Google Glass the corresponding LEDs could be turned on and off. The capabilities to sequentially activate and deactivate LEDs and random manipulation are further shown in Supplementary Movies 5 and 6.

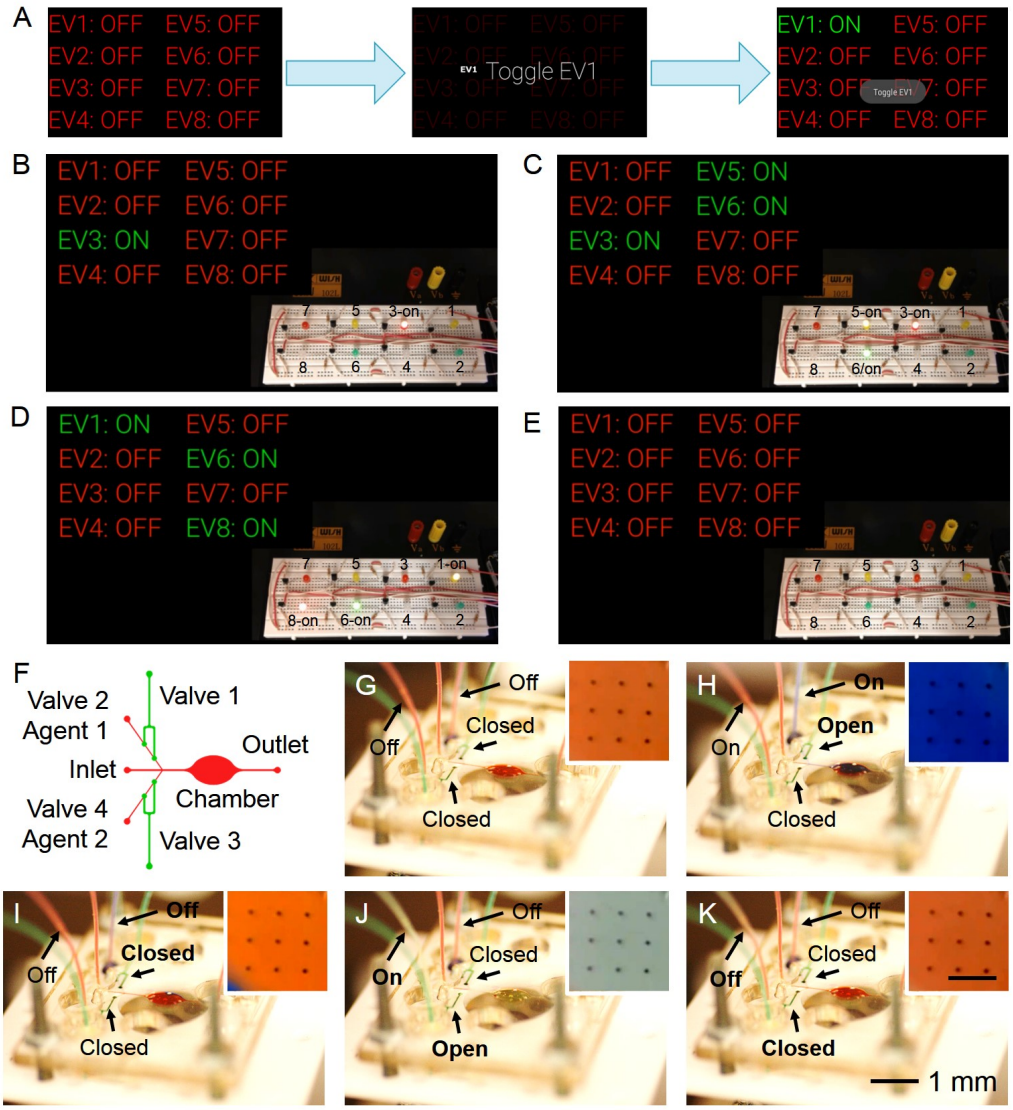

Figure 5.4 – Controlling electrovalves and microfluidic actuators using Google Glass. (**A**) Diagrams showing the control of the electrovalves on the Google Glass. (**B-E**) Demonstration of control over the blinking of LEDs from the Glass. (**E**) A microfluidic bioreactor with built-in valves and inlets for drug testing. A mini-microscope was fitted at the bottom of the bioreactor for real-time analysis. (**F**) Schematic of the microfluidic bioreactor for evaluating the Google Glass-directed

electrovalve controllers. (**F-K**) Sequential activation of Valve 1 and Valve 2 from the Glass, as indicated by alternation of food colors injected from the inlet, Agent 1 channel, and Agent 2 channel. Insets show images taken by the mini-microscope at the bottom of the bioreactor chamber clearly indicating matching color changes in the flow.

We subsequently constructed a microfluidic bioreactor consisting of an elliptical chamber, one central inlet for medium circulation, and two side inlets with corresponding pressure-driven pneumatic valves, which together with linked pressure-driven reservoirs (both activated by electrovalves), accomplish the injection of target agents (Figure 5.4F). We then first demonstrated the capability to remotely actuate the valves with the commands wirelessly transmitted from the Google Glass to the BeagleBone board. As shown in Figure 5.4G-K, we initially injected medium in the central inlet, with both side channels closed by the valves (Figure 5.4G). To drive blue dye from the reservoir to the bioreactor chamber we sequentially opened the channel by deactivating Valve 1 and pressurized the blue dye reservoir by activating Valve 2 (Figure 5.4H). Reversing these actions and performing the same Google Glass commands on Valves 3 and 4 allowed yellow dye to infuse the bioreactor chamber (Figure 5.4J). Finally, the valves were reset to the initial configuration, restoring the circulation of the medium through the central inlet (Figure 5.4K).

Additionally, a mini-microscope was fitted at the bottom of the bioreactor for real-time monitoring, and connected to the BeagleBone board. The insets in Figure 5.4F-J, show the change in color of the liquid pumped into the bioreactor chamber, monitored by the mini-microscope in real-time.

5.3.5 Simultaneous remote control and monitoring of liver-on-a-chip for drug testing

The main purpose of the liver is to provide detoxification of various metabolites, protein/enzyme synthesis, and the production of bile necessary for digestion of food, rendering hepatotoxicity studies an important target for multiple fields. Here we introduced human primary hepatocytes into the chamber of the microfluidic bioreactor to construct a liver-on-a-chip platform. Liver spheroids of approximately 200 μm were first formed using a

non-adherent microwell array (345), which were then retrieved, suspended in GelMA, and crosslinked to the bottom of the bioreactor chamber. Prior to the experiment, acetaminophen (APAP), a hepatotoxic drug, was added to the reservoir of one of the side channels. The liver bioreactor was initially perfused with hepatocyte growth medium from the central inlet in the first 24 h with the side channels closed (Figure 5.5A-B). At 24 h we used the Google Glass to inject APAP for 1 min. Commands were sent from the Glass deactivating the valve and activating the pressure to inject APAP (Figure 5.5C-D). The channel was then closed to stop the APAP injection and restore the regular perfusion with the hepatocyte growth medium (Figure 5.5E-F). The mini-microscope fitted at the bottom of the bioreactor monitored the morphology of the liver spheroids, transmitting the data to the Google Glass for real-time, *in situ* monitoring of drug treatment effect. Without any drug, the liver organoid remained healthy and tightly agglomerated (Figure 5.5G-H). In comparison, 12 h post injection of 15 mM APAP, the liver spheroid micrographs transmitted through the mini-microscope to the Google Glass showed swollen cellular structures (Figure 5.5I), clearly exhibiting signs of a toxicological response to APAP treatment. The decreased liver functionality was further confirmed by off-chip viability assay and analysis of damage biomarker glutathione S-transferase *α* (GST-*α*, Figure 5.5J-L), well correlating to the observed hepatotoxicity with the Google Glass-directed drug administration and organoid monitoring.

In this particular demonstration we highlight that the entire process, including the operation of the valves, injection of the drug, restoration of the main perfusion, and monitoring the morphology with the mini-microscope was solely controlled by the Google Glass without direct manipulation of the liver-on-a-chip device or the valves system. Such seamless interface allows for remote actuation of microfluidic devices and easy access of sensed data, potentially enabling long-term communication and control between humans and microdevices.

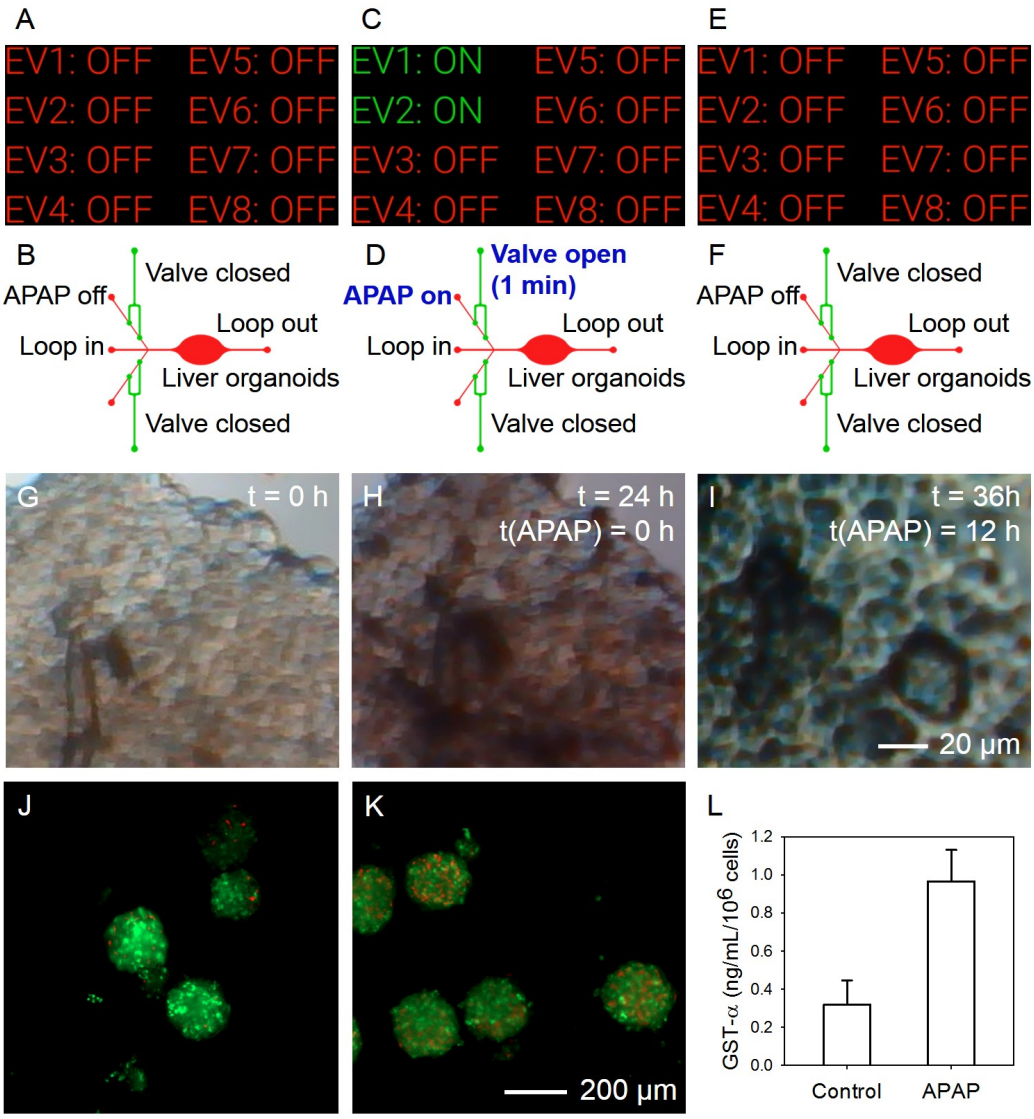

Figure 5.5 – Remote activation of electrovalves using the Google Glass for drug testing on the liver-on-a-chip platform fabricated from human primary hepatocyte spheroids. (A,B) All valves were off to allow regular culture of the liver organoids. (C,D) At 24 h post culture, Valves 1/2 were activated from the Glass and 15 mM APAP was injected into the circulation for 1 min. (E,F) Valves 1/2 were then deactivated and the culture was maintained for another 12 h. (G-I) Mini-microscopic image clearly showed swelling, sign of apoptosis of the liver organoid post APAP treatment. (J,K) Live/dead assay of the liver organoids (J) with and (K) without APAP treatment, indicating increased cell death when the cells were incubated with APAP. (L) Levels of the liver damage biomarker GST-α measured by ESLIA, showing the same trend of cell death when treated with APAP.

5.3 Conclusions

For the first time we have developed a set of hardware, firmware, and Glassware that enabled wireless transmission of sensor data onto the Google Glass for on-demand data visualization and real-time analysis. We have further engineered the hardware and software

to allow the control of electrical outputs from commands entered by the Glass. We demonstrated the platform's capability to monitor physical and physiological parameters such as temperature, pH, and microscopic morphological images and videos, of an integrated liver-and-heart-on-a-chip. The Glass also achieved beating analysis of the cardiac organoids. We then proved that the pneumatic electrovalves could be remotely activated by the Glass to introduce pharmaceutical compounds into the microfluidic liver bioreactor at desired time points, with their effects being transmitted to the Glass for continuous real-time monitoring.

We believe that such an innovative platform is a premise in wearable sensing and controlling technology for applications in biomedicine, surgery and general laboratory. The Glass might be of particular importance in cases where the experimental conditions threat human life, as when researchers work with highly contagious bacteria and virus or radioactivity.

CHAPTER VI

CONCLUSIONS AND FUTURE WORK

CHAPTER VI – Conclusions

6.1 Main findings

Through this thesis, we unveiled that mechanical strain is an important inducer of inflammatory and vascular injury response in SMCs derived from Progeria iPSCs. On the one hand, when cells were placed in conventional cell culture systems (e.g. petri dish, well plate), there is no inflammatory and vascular injury response at a transcriptional level. On the other hand, when cells were cultured inside a novel microfluidic system that applies strain mimicking that of blood vessels, the transcriptional response emerges and is exacerbated with the magnitude of strain. Several are the implications of the results observed. A common issue in progeria patients is the monitoring of disease progression, with a lack of clinical biomarkers. Inflammation-related biomarkers have been explored as markers of aging. For example, C-reactive protein (CRP), IL-6, and TNFα elevation in plasma levels seems to be related to aging, with strong evidence as a predictor of mortality in individuals without progeria (346). At the same time higher levels of these cytokines have been linked to increased arterial stiffness (347). In our results we showed that IL-6, a pro-inflammatory cytokine, is highly expressed in progeria iPS-SMCs under mechanical strain, which suggests that it could be used to monitor disease progression, especially in clinical trials or drug discovery pipelines. Several other clinical markers have been used during progeria clinical trials (253). These include skeletal rigidity changes (bone mineral density), weight gain, cardiovascular changes, audiological changes, among others (253). Regarding cardiovascular alterations, a lonafarnib clinical trial showed that it could reduce the carotid-femoral pulse wave velocity (a measure of arterial stiffness) and intima media thickness in progeria patients. We hypothesize that IL-6 could indeed precede changes in pulse wave velocity, as well as contribute to the observed increase in arterial stiffness and intima media thickening. This could be in part due to the contribution of IL-6 to the inflammatory state of the blood vessel wall, leading to increased stiffness. IL-6 mRNA has been reported in progeria models *in vivo*, and we showed in our system similar responses. It is not clear, however, if IL-6 increases precede clinical changes such as bone density loss, and further

studies this cytokine are required to validate it as a potential marker of disease. IL-6 studies should also be extended to CRP, TNFα, CXCL1, NF-KB and potentially other pro-inflammatory cytokines that could be used alone, or in combination, to evaluate the progress of disease. A wide scale mapping of such differences, potentiated by the progeria-on-a-chip, could shed light into the combined effect of different cytokines, and provide a cytokine fingerprint that could be used to statistically differentiate both disease states and progression. Different lines of evidence suggest that inflammation might play a critical role, but it is uncertain if inflammation starts before or after other clinical markers. In addition to transcriptome level changes, we observed increased DNA damage and cell senescence in progeria SMCs under mechanical strain. These further suggested a higher rate of cellular "aging", although additional studies are required to show other markers of aging, such as mitochondrial dysfunction, genomic instability, epigenetic alterations, among others.

This thesis contributed also to underpinning the importance of mechanical strain on primary SMCs and induction of vascular disease. We focused on the hypertensive phenotype generated by incubation with angiotensin II, and observed differences in ROS, caveolin-1, and pro-inflammatory markers IL-6 and IL-1β. One interesting observation came from assessing the levels of cytosolic and mitochondrial superoxide dismutase (SOD1 and SOD2), where we found that different levels of strain regulate superoxide production through different pathways. With normal strain levels we observed an increase in cytosolic SOD, but pathological levels of strain induced mitochondrial SOD. We have additionally shown that by inhibiting NAPDH oxidase (source of cytosolic superoxide) in normal strain we could restore SOD1 mRNA levels without affecting SOD2 ones. The observation points towards a mechanical modulator of ROS production, and further research is required to understand how and why this happens. In addition to these, we have shown that markers observed in models of hypertension, or even in patients, were altered also in our system upon application of pathological strain. This was an important step to simulating the effects of a vascular disease without requiring pharmaceutical inducers. Systems that naturally recapitulate a disease state are especially important for pharmaceutical industry because they avoid adding

multiple drugs to cell lines (disease-inducing drug and disease-treating drug) due to potentially cross-effects.

The microfluidic platform generated here was built on previous work and improved several design aspects. As identified in chapter 1, manufacturing and standardization are a critical issue affecting the industrial use of organs-on-a-chip. The fabrication process developed in this thesis for the progeria-on-a-chip system is simpler and has less steps than previously published ones, and does not require highly trained operators. These two factors make the system more affordable that previous approaches. Furthermore, by using a design thinking approach during the design stage of the device it was possible to include early-on user feedback. This approach allowed making a device that is extremely user friendly and requires minimal adoption effort to be used.

The second part of this thesis produced a new way of monitoring microfluidic processes and organs-on-a-chip devices, and a new paradigm of interaction with microfluidics through augmented reality. Microscopy in organs-on-a-chip is often challenging due to the bulk of the devices and the impracticality of high-content imaging. In this thesis we created a mini-microscope based on a lens-free approach, and further extended it to multiple magnifications, fluorescence capabilities, and introduced applications in oxygen sensing. The high versatility and low cost of the solution are such that we envision laboratories and companies can replicate these for certain applications. However, a limitation of the current system is the quality of image and resolution, which is far from confocal or two-photon capabilities. Nevertheless, several applications are relevant in this system, such as oxygen sensing in organ-on-a-chip systems. The field is also moving towards real-time sensing, either morphology analysis or metabolite sensing. New miniaturized equipment and capabilities will be required to answer these needs, and the mini-microscope and applications developed here are a step forward towards that direction. Finally, two other contributions were introduced in this thesis, (i) remote monitoring and control of microfluidics and (ii) augmented reality solutions for the laboratory setting. Regarding the first, often times researchers have to deal with materials harmful to human health (virus, bacteria, biological

weapons, among others). In these cases, safety protocols and guidelines are strict, and protective equipment is mandatory. The system developed with the Google Glass provide a novel way of interacting and controlling microfluidic and organ-on-a-chip systems, allowing researchers to conduct experiments with harmful reagents without risk to human health. At the same time, the usage of the Google Glass introduces the concept of augment reality in a laboratory setting, and the potential applications thereof. Such technologies are being currently used in surgeries, but have not found a place in a laboratory setting. We envision several applications of the augmented reality system developed. For instance, laborious tasks such as filling a qPCR plate can be made easier by visualizing an overlay of which samples to place in each well, all while observing said plate, bench and pipette. The utilization of these new technologies will enable faster, reliable, and protected access to data, as well as decision making.

In summary, we were able to generate a new vascular in vitro system to model vascular disease and aging, the set of tools required to operate it, and new ways of monitoring and controlling organ-on-chip systems through augmented reality.

6.2 Future work

The systems developed here are a platform technology that aims to open new lines of research or strengthen the capabilities to answer questions already opened. First and foremost, this work opened several questions in the area of vascular aging. The early indication of an exacerbated pro-inflammatory state needs to be confirmed at a protein level, and other cytokines need to be evaluated. In particular, the balance between pro- and anti-inflammatory cytokines needs to be determined to evaluate whether strain impacts a combined dysregulation, or only an increase in pro-inflammatory cytokines. Due to the small dimension of the device, it is often difficult to gather enough media to measure different protein markers offline. Developments that include our technology mentioned in Chapter 4 and 5 are able to measure specific targets (via respective antibody/aptamer) in-line with organ-on-a-chip platforms and in real-time (348). It is important to combine these platforms to

understand in real-time the evolution of inflammatory markers. The pro-inflammatory gene expression observed in the progeria-on-a-chip needs further validation, especially through *in vivo* models such as in the $LMNA^{G609G/G609G}$ mouse(349), which exhibits NF-KB activation and related increase in IL-6, TNFα, and CXCL1 (167). Rapamycin is able to block nuclear translocation of NF-KB in SMCs (350) and is showing promise as a therapeutic alternative for progeria (211, 250, 351). The progeria-on-a-chip model can be a prime system to test and understand the mechanisms behind rapamycin function in progeria and aging especially relating to anti-inflammatory functions. Testing the effects of rapamycin, as well as other anti-inflammatory drugs or gene targeting strategies (IL-6 targeted) in a context of exacerbated strain responses would allow to understand if such therapies are valid. Importantly, other factors need to be taken into account besides inflammation, as discussed above, such as mitochondrial dysfunction, senescence, nuclear abnormalities among others.

There are several reports on the influence of mechanical strain and shear stress on ECs but fewer on SMCs. In particular, there is a lack of systems that integrate several cell types such as EC and SMC in a unified platform. The signaling interplay between ECs and SMCs in crucial for the homeostasis of the blood vessel wall, with NO and other cellular signaling pathways affecting the responses to pathologic stimuli. Going forward we propose the generation of a co-culture system with SMCs and ECs under dynamic cell culture conditions. We have already started combining the two cells types, and showed the feasibility of having such co-cultures for short periods of time in culture under cyclic strain. The combination of the two cell types, and potentially more in the future (pericytes, fibroblasts, etc), would allow studying and questioning the effects of mechanical stimuli on blood vessels and its impact on physiological and pathological conditions, as well as aging.

Another avenue of research for future studies is the variation of several parameters such as cyclic strain amount, frequency and modality of strain. For instance, certain patterns of application of shear stress can be deleterious to ECs, while others prove to be harmless. It is important to understand how different patterns of application of strain influences SMC behavior. As an immediate example, during exercise, blood vessels experience a momentary

increase in strain. Given the beneficial effects of exercise, it is reasonable to question how temporary increase of mechanical stimuli results in health improvements.

The field of organs-on-a-chip is increasingly moving towards the integration of multiple organ systems. Individual organ modules are to be combined together in order to observe system wide effects. Pro-drugs can be metabolized in liver modules and the resulting metabolite can exert its effects on the heart and blood vessel modules. Immediate impact can be achieved with individual organ modules, such as the one developed here. We envision that developments in the near future will lead to organ system modules, and in the long run a full human-on-a-chip system. The next sensible goal would be to integrate the vasculature-on-a-chip with heart- and lung-on-chip systems, as well as perfusion using blood. This would allow to re-create a circulatory system of a-chip system. However, challenges still exist and need to be tackled in order to generate multi organ-on-a-chip systems. Perfusion can be an issue, especially when several cell types require different cell medias. Another important factor that researchers have been struggling with is deciding a scaling factor and rationale, whether it is based on cell number, volume or mass.

The application of the new platforms developed here by the pharmaceutical and/or other industries require several other challenges to be solved. The models currently generated are fabricated in a laboratory setting and present batch to batch variability. Fabrication methodologies and materials need to be addressed to allow the large scale production of such systems, with quality control processes that guarantee minimal or no batch-to-batch variation. In addition, the choice of materials is crucial. For example, PDMS is easy to use and ideal for prototyping but might be permeable to certain pharmaceutical compounds. Other elastomeric or plastic-based materials could be used to avoid such problems. We have taken the first steps moving toward automation of organ-on-a-chip devices. To harvest their full potential and be economically feasible, automated systems need to be further developed to allow controlling, monitoring and sensing analytes of interest on-the-run and in real-time. Finally, regulatory issues need to be addressed by validating the

models generated with in vivo test, and compared to human data obtained through clinical trials.

Overall, organs-on-a-chip represent a new field of research that intersects molecular biology, pharmacology, medicine, and engineering. The work developed here is another stepping stone towards the usage of such systems by researchers in academic laboratories as well as pharmaceutical companies during the drug development pipeline.

References

1. Mozaffarian D, Benjamin EJ, Go AS, Arnett DK, Blaha MJ, Cushman M, et al. Heart Disease and Stroke Statistics-2015 Update: A Report From the American Heart Association. Circulation. 2014;131:e29-322.

2. Faxon DP, Fuster V, Libby P, Beckman JA, Hiatt WR, Thompson RW, et al. Atherosclerotic Vascular Disease Conference: Writing Group III: pathophysiology. Circulation. 2004;109:2617-25.

3. Nicolini F, Gherli T. Alternatives to transplantation in the surgical therapy for heart failure. European journal of cardio-thoracic surgery : official journal of the European Association for Cardio-thoracic Surgery. 2009;35:214-28.

4. Effects of enalapril on mortality in severe congestive heart failure. Results of the Cooperative North Scandinavian Enalapril Survival Study (CONSENSUS). The CONSENSUS Trial Study Group. The New England journal of medicine. 1987;316:1429-35.

5. Effect of enalapril on survival in patients with reduced left ventricular ejection fractions and congestive heart failure. The SOLVD Investigators. The New England journal of medicine. 1991;325:293-302.

6. Lechat P, Packer M, Chalon S, Cucherat M, Arab T, Boissel J-P. Clinical Effects of -Adrenergic Blockade in Chronic Heart Failure : A Meta-Analysis of Double-Blind, Placebo-Controlled, Randomized Trials. Circulation. 1998;98:1184-91.

7. Heusch G, Libby P, Gersh B, Yellon D, Böhm M, Lopaschuk G, et al. Cardiovascular remodelling in coronary artery disease and heart failure. Lancet. 2014;383:1933-43.

8. Ciociola AA, Cohen LB, Kulkarni P. How drugs are developed and approved by the FDA: current process and future directions. The American journal of gastroenterology. 2014;109:620-3.

9. Paul SM, Mytelka DS, Dunwiddie CT, Persinger CC, Munos BH, Lindborg SR, et al. How to improve R&D productivity: the pharmaceutical industry's grand challenge. Nature reviews Drug discovery. 2010;9:203-14.

10. Cook D, Brown D, Alexander R, March R, Morgan P, Satterthwaite G, et al. Lessons learned from the fate of AstraZeneca's drug pipeline: a five-dimensional framework. Nature reviews Drug discovery. 2014;13:419-31.

11. Kola I, Landis J. Can the pharmaceutical industry reduce attrition rates? Nature reviews Drug discovery. 2004;3:711-5.

12. Menna P, Salvatorelli E, Minotti G. Cardiotoxicity of antitumor drugs. Chemical research in toxicology. 2008;21:978-89.

13. Piccini JP, Whellan DJ, Berridge BR, Finkle JK, Pettit SD, Stockbridge N, et al. Current challenges in the evaluation of cardiac safety during drug development: translational medicine meets the Critical Path Initiative. American heart journal. 2009;158:317-26.
14. Shah RR. Can pharmacogenetics help rescue drugs withdrawn from the market? Pharmacogenomics. 2006;7:889-908.
15. Chu X, Bleasby K, Evers R. Species differences in drug transporters and implications for translating preclinical findings to humans. Expert Opinion on Drug Metabolism & Toxicology. 2013.
16. Hirt MN, Hansen A, Eschenhagen T. Cardiac tissue engineering: state of the art. Circulation research. 2014;114:354-67.
17. Zhang WJ, Liu W, Cui L, Cao Y. Tissue engineering of blood vessel. J Cell Mol Med. 2007;11:945-57.
18. Benam KH, Dauth S, Hassell B, Herland A, Jain A, Jang K-J, et al. Engineered In Vitro Disease Models. Annual review of pathology. 2015;10:195-262.
19. Li S, Sengupta D, Chien S. Vascular tissue engineering: From in vitro to in situ. Wiley Interdisciplinary Reviews: Systems Biology and Medicine. 2014;6:61-76.
20. Mathur A, Ma Z, Loskill P, Jeeawoody S, Healy KE. In Vitro Cardiac Tissue Models: Current Status and Future Prospects. Advanced Drug Delivery Reviews. 2015.
21. Bhatia SN, Ingber DE. Microfluidic organs-on-chips. Nature biotechnology. 2014;32:760-72.
22. Polini A, Prodanov L, Bhise NS, Manoharan V, Dokmeci MR, Khademhosseini A. Organs-on-a-chip: a new tool for drug discovery. Expert opinion on drug discovery. 2014;9:335-52.
23. Zhang YS, Aleman J, Arneri A, Bersini S, Piraino F, Shin SR, et al. From Cardiac Tissue Engineering to Heart-on-a-Chip: Beating Challenges. Biomed Mater. 2015;10:034006.
24. Bhise NS, Ribas J, Manoharan V, Zhang YS, Polini A, Massa S, et al. Organ-on-a-chip platforms for studying drug delivery systems. Journal of controlled release : official journal of the Controlled Release Society. 2014;190:82-93.
25. Ghaemmaghami AM, Hancock MJ, Harrington H, Kaji H, Khademhosseini A. Biomimetic tissues on a chip for drug discovery. Drug discovery today. 2012;17(3-4):173-81.
26. Gregorio CC, Antin PB. To the heart of myofibril assembly. Trends in cell biology. 2000;10:355-62.
27. Holt E, Lunde PK, Sejersted OM, Christensen G. Electrical stimulation of adult rat cardiomyocytes in culture improves contractile properties and is associated with altered calcium handling. Basic research in cardiology. 1997;92:289-98.
28. Brutsaert DL. Cardiac endothelial-myocardial signaling: its role in cardiac growth, contractile performance, and rhythmicity. Physiological reviews. 2003;83(1):59-115.

29. Roberts DE, Scher AM. Effect of tissue anisotropy on extracellular potential fields in canine myocardium in situ. Circulation research. 1982;50:342-51.

30. Souders CA, Bowers SLK, Baudino TA. Cardiac Fibroblast: The Renaissance Cell. Circulation Research. 2009;105:1164-76.

31. Neuži P, Giselbrecht S, Länge K, Huang TJ, Manz A. Revisiting lab-on-a-chip technology for drug discovery. Nature reviews Drug discovery. 2012;11:620-32.

32. Duffy DC, McDonald JC, Schueller OJ, Whitesides GM. Rapid Prototyping of Microfluidic Systems in Poly(dimethylsiloxane). Analytical chemistry. 1998;70(23):4974-84.

33. Halldorsson S, Lucumi E, Gómez-Sjöberg R, Fleming RMT. Advantages and challenges of microfluidic cell culture in polydimethylsiloxane devices. Biosensors & bioelectronics. 2015;63:218-31.

34. Annabi N, Selimović Š, Acevedo Cox JP, Ribas J, Afshar Bakooshli M, Heintze D, et al. Hydrogel-coated microfluidic channels for cardiomyocyte culture. Lab on a chip. 2013;13:3569-77.

35. Nichol JW, Koshy ST, Bae H, Hwang CM, Yamanlar S, Khademhosseini A. Cell-laden microengineered gelatin methacrylate hydrogels. Biomaterials. 2010;31(21):5536-44.

36. Wise SG, Mithieux SM, Weiss AS. Engineered tropoelastin and elastin-based biomaterials. Advances in protein chemistry and structural biology. 2009;78:1-24.

37. Annabi N, Shin SR, Tamayol A, Miscuglio M, Bakooshli MA, Assmann A, et al. Highly Elastic and Conductive Human-Based Protein Hybrid Hydrogels. Advanced materials. 2015.

38. Agarwal A, Goss JA, Cho A, McCain ML, Parker KK. Microfluidic heart on a chip for higher throughput pharmacological studies. Lab on a chip. 2013;13:3599-608.

39. Saffitz JE, Kanter HL, Green KG, Tolley TK, Beyer EC. Tissue-specific determinants of anisotropic conduction velocity in canine atrial and ventricular myocardium. Circ Res. 1994;74(6):1065-70.

40. Spach MS, Heidlage JF, Dolber PC, Barr RC. Changes in anisotropic conduction caused by remodeling cell size and the cellular distribution of gap junctions and Na(+) channels. Journal of electrocardiology. 2001;34 Suppl:69-76.

41. Bian W, Jackman CP, Bursac N. Controlling the structural and functional anisotropy of engineered cardiac tissues. Biofabrication. 2014;6(2):024109.

42. Grosberg A, Alford PW, McCain ML, Parker KK. Ensembles of engineered cardiac tissues for physiological and pharmacological study: Heart on a chip. Lab on a Chip. 2011;11:4165.

43. Tandon N, Cannizzaro C, Chao PH, Maidhof R, Marsano A, Au HT, et al. Electrical stimulation systems for cardiac tissue engineering. Nature protocols. 2009;4(2):155-73.

44. Aubin H, Nichol JW, Hutson CB, Bae H, Sieminski AL, Cropek DM, et al. Directed 3D cell alignment and elongation in microengineered hydrogels. Biomaterials. 2010;31:6941-51.

45. Heidi Au HT, Cui B, Chu ZE, Veres T, Radisic M. Cell culture chips for simultaneous application of topographical and electrical cues enhance phenotype of cardiomyocytes. Lab on a chip. 2009;91:564-75.

46. Xiao Y, Zhang B, Liu H, Miklas JW, Gagliardi M, Pahnke A, et al. Microfabricated perfusable cardiac biowire: a platform that mimics native cardiac bundle. Lab on a chip. 2014;14:869-82.

47. Davis RP, Casini S, van den Berg CW, Hoekstra M, Remme CA, Dambrot C, et al. Cardiomyocytes derived from pluripotent stem cells recapitulate electrophysiological characteristics of an overlap syndrome of cardiac sodium channel disease. Circulation. 2012;125:3079-91.

48. Itzhaki I, Maizels L, Huber I, Zwi-Dantsis L, Caspi O, Winterstern A, et al. Modelling the long QT syndrome with induced pluripotent stem cells. Nature. 2011;471:225-9.

49. Sun N, Yazawa M, Liu J, Han L, Sanchez-Freire V, Abilez OJ, et al. Patient-specific induced pluripotent stem cells as a model for familial dilated cardiomyopathy. Science translational medicine. 2012;4:130ra47.

50. Chang MG, Zhang Y, Chang CY, Xu L, Emokpae R, Tung L, et al. Spiral waves and reentry dynamics in an in vitro model of the healed infarct border zone. Circulation research. 2009;105:1062-71.

51. Katare RG, Ando M, Kakinuma Y, Sato T. Engineered heart tissue: a novel tool to study the ischemic changes of the heart in vitro. PloS one. 2010;5:e9275.

52. Mosadegh B, Dabiri BE, Lockett MR, Derda R, Campbell P, Parker KK, et al. Three-dimensional paper-based model for cardiac ischemia. Advanced healthcare materials. 2014;3:1036-43.

53. Song H, Zandstra PW, Radisic M. Engineered heart tissue model of diabetic myocardium. Tissue engineering Part A. 2011;17:1869-78.

54. Stöhr A, Friedrich FW, Flenner F, Geertz B, Eder A, Schaaf S, et al. Contractile abnormalities and altered drug response in engineered heart tissue from Mybpc3-targeted knock-in mice. Journal of molecular and cellular cardiology. 2013;63:189-98.

55. Li AH, Liu PP, Villarreal FJ, Garcia RA. Dynamic changes in myocardial matrix and relevance to disease: Translational perspectives. Circulation Research. 2014;114:916-27.

56. Ieda M, Tsuchihashi T, Ivey KN, Ross RS, Hong TT, Shaw RM, et al. Cardiac fibroblasts regulate myocardial proliferation through beta1 integrin signaling. Developmental cell. 2009;16(2):233-44.

57. Schroer AK, Merryman WD. Mechanobiology of myofibroblast adhesion in fibrotic cardiac disease. Journal of cell science. 2015;128(10):1865-75.

58. McCain ML, Parker KK. Mechanotransduction: the role of mechanical stress, myocyte shape, and cytoskeletal architecture on cardiac function. Pflugers Archiv : European journal of physiology. 2011;462(1):89-104.

59. McCain ML, Sheehy SP, Grosberg A, Goss JA, Parker KK. Recapitulating maladaptive, multiscale remodeling of failing myocardium on a chip. Proceedings of the National Academy of Sciences of the United States of America. 2013;110:9770-5.

60. Ho CY. Hypertrophic cardiomyopathy: preclinical and early phenotype. Journal of cardiovascular translational research. 2009;2:462-70.

61. Ren L, Liu W, Wang Y, Wang J-C, Tu Q, Xu J, et al. Investigation of hypoxia-induced myocardial injury dynamics in a tissue interface mimicking microfluidic device. Analytical chemistry. 2013;85:235-44.

62. Chen MB, Srigunapalan S, Wheeler AR, Simmons CA. A 3D microfluidic platform incorporating methacrylated gelatin hydrogels to study physiological cardiovascular cell-cell interactions. Lab on a chip. 2013;13:2591-8.

63. Garbern JC, Lee RT. Cardiac stem cell therapy and the promise of heart regeneration. Cell stem cell. 2013;12(6):689-98.

64. He J, Ma C, Liu W, Wang J. On-chip monitoring of skeletal myoblast transplantation for the treatment of hypoxia-induced myocardial injury. The Analyst. 2014;1391:4482-90.

65. Taylor PM, Batten P, Brand NJ, Thomas PS, Yacoub MH. The cardiac valve interstitial cell. The international journal of biochemistry & cell biology. 2003;35:113-8.

66. Wipff PJ, Rifkin DB, Meister JJ, Hinz B. Myofibroblast contraction activates latent TGF-beta1 from the extracellular matrix. The Journal of cell biology. 2007;179(6):1311-23.

67. Merryman WD, Schoen FJ. Mechanisms of calcification in aortic valve disease: role of mechanokinetics and mechanodynamics. Current cardiology reports. 2013;15:355.

68. Rajamannan NM, Evans FJ, Aikawa E, Grande-Allen KJ, Demer LL, Heistad DD, et al. Calcific aortic valve disease: not simply a degenerative process: A review and agenda for research from the National Heart and Lung and Blood Institute Aortic Stenosis Working Group. Executive summary: Calcific aortic valve disease-2011 update. Circulation. 2011;124:1783-91.

69. Simmons CA, Grant GR, Manduchi E, Davies PF. Spatial heterogeneity of endothelial phenotypes correlates with side-specific vulnerability to calcification in normal porcine aortic valves. Circulation research. 2005;96:792-9.

70. Martins AM, Vunjak-Novakovic G, Reis RL. The current status of iPS cells in cardiac research and their potential for tissue engineering and regenerative medicine. Stem cell reviews. 2014;10:177-90.

71. Mercola M, Colas A, Willems E. Induced pluripotent stem cells in cardiovascular drug discovery. Circulation research. 2013;112:534-48.

72. Wang G, McCain ML, Yang L, He A, Pasqualini FS, Agarwal A, et al. Modeling the mitochondrial cardiomyopathy of Barth syndrome with induced pluripotent stem cell and heart-on-chip technologies. Nature medicine. 2014;20:616-23.

73. Bianchi E, Molteni R, Pardi R, Dubini G. Microfluidics for in vitro biomimetic shear stress-dependent leukocyte adhesion assays. Journal of biomechanics. 2013;46(2):276-83.

74. Swartz MA, Fleury ME. Interstitial flow and its effects in soft tissues. Annual review of biomedical engineering. 2007;9:229-56.

75. Wong KH, Chan JM, Kamm RD, Tien J. Microfluidic models of vascular functions. Annual review of biomedical engineering. 2012;14:205-30.

76. Kim S, Lee H, Chung M, Jeon NL. Engineering of functional, perfusable 3D microvascular networks on a chip. Lab Chip. 2013;13(8):1489-500.

77. Bertassoni LE, Cardoso JC, Manoharan V, Cristino AL, Bhise NS, Araujo WA, et al. Direct-write bioprinting of cell-laden methacrylated gelatin hydrogels. Biofabrication. 2014;6(2):024105.

78. Hasenberg T, Muhleder S, Dotzler A, Bauer S, Labuda K, Holnthoner W, et al. Emulating human microcapillaries in a multi-organ-chip platform. Journal of biotechnology. 2015;216:1-10.

79. Morgan JP, Delnero PF, Zheng Y, Verbridge SS, Chen J, Craven M, et al. Formation of microvascular networks in vitro. Nature protocols. 2013;8(9):1820-36.

80. Wang XY, Jin ZH, Gan BW, Lv SW, Xie M, Huang WH. Engineering interconnected 3D vascular networks in hydrogels using molded sodium alginate lattice as the sacrificial template. Lab Chip. 2014;14(15):2709-16.

81. Yeon JH, Ryu HR, Chung M, Hu QP, Jeon NL. In vitro formation and characterization of a perfusable three-dimensional tubular capillary network in microfluidic devices. Lab Chip. 2012;12(16):2815-22.

82. Schimek K, Busek M, Brincker S, Groth B, Hoffmann S, Lauster R, et al. Integrating biological vasculature into a multi-organ-chip microsystem. Lab Chip. 2013;13(18):3588-98.

83. Gunther A, Yasotharan S, Vagaon A, Lochovsky C, Pinto S, Yang J, et al. A microfluidic platform for probing small artery structure and function. Lab Chip. 2010;10(18):2341-9.

84. Bogorad MI, DeStefano J, Karlsson J, Wong AD, Gerecht S, Searson PC. Review: in vitro microvessel models. Lab Chip. 2015;15(22):4242-55.

85. Yasotharan S, Pinto S, Sled JG, Bolz SS, Gunther A. Artery-on-a-chip platform for automated, multimodal assessment of cerebral blood vessel structure and function. Lab Chip. 2015;15(12):2660-9.

86. Kusunose J, Zhang H, Gagnon MK, Pan T, Simon SI, Ferrara KW. Microfluidic system for facilitated quantification of nanoparticle accumulation to cells under laminar flow. Ann Biomed Eng. 2013;41(1):89-99.

87. Kim D, Finkenstaedt-Quinn S, Hurley KR, Buchman JT, Haynes CL. On-chip evaluation of platelet adhesion and aggregation upon exposure to mesoporous silica nanoparticles. Analyst. 2014.

88. Korin N, Kanapathipillai M, Matthews BD, Crescente M, Brill A, Mammoto T, et al. Shear-activated nanotherapeutics for drug targeting to obstructed blood vessels. Science. 2012;337(6095):738-42.

89. Young EW, Watson MW, Srigunapalan S, Wheeler AR, Simmons CA. Technique for real-time measurements of endothelial permeability in a microfluidic membrane chip using laser-induced fluorescence detection. Analytical chemistry. 2010;82(3):808-16.

90. Lamberti G, Tang Y, Prabhakarpandian B, Wang Y, Pant K, Kiani MF, et al. Adhesive interaction of functionalized particles and endothelium in idealized microvascular networks. Microvasc Res. 2013;89:107-14.

91. Doshi N, Prabhakarpandian B, Rea-Ramsey A, Pant K, Sundaram S, Mitragotri S. Flow and adhesion of drug carriers in blood vessels depend on their shape: a study using model synthetic microvascular networks. Journal of controlled release : official journal of the Controlled Release Society. 2010;146(2):196-200.

92. Rosano JM, Tousi N, Scott RC, Krynska B, Rizzo V, Prabhakarpandian B, et al. A physiologically realistic in vitro model of microvascular networks. Biomed Microdevices. 2009;11(5):1051-7.

93. Mahto SK, Yoon TH, Rhee SW. A new perspective on in vitro assessment method for evaluating quantum dot toxicity by using microfluidics technology. Biomicrofluidics. 2010;4(3).

94. Namdee K, Thompson AJ, Charoenphol P, Eniola-Adefeso O. Margination propensity of vascular-targeted spheres from blood flow in a microfluidic model of human microvessels. Langmuir. 2013;29(8):2530-5.

95. Samuel SP, Jain N, O'Dowd F, Paul T, Kashanin D, Gerard VA, et al. Multifactorial determinants that govern nanoparticle uptake by human endothelial cells under flow. Int J Nanomedicine. 2012;7:2943-56.

96. Kolhar P, Anselmo AC, Gupta V, Pant K, Prabhakarpandian B, Ruoslahti E, et al. Using shape effects to target antibody-coated nanoparticles to lung and brain endothelium. Proc Natl Acad Sci U S A. 2013;110(26):10753-8.

97. Fraikin JL, Teesalu T, McKenney CM, Ruoslahti E, Cleland AN. A high-throughput label-free nanoparticle analyser. Nat Nanotechnol. 2011;6(5):308-13.

98. Wang F, Wang H, Wang J, Wang H-Y, Rummel PL, Garimella SV, et al. Microfluidic delivery of small molecules into mammalian cells based on hydrodynamic focusing. Biotechnology and Bioengineering. 2008;100(1):150-8.
99. Bischel LL, Young EW, Mader BR, Beebe DJ. Tubeless microfluidic angiogenesis assay with three-dimensional endothelial-lined microvessels. Biomaterials. 2013;34(5):1471-7.
100. Galie PA, Nguyen DH, Choi CK, Cohen DM, Janmey PA, Chen CS. Fluid shear stress threshold regulates angiogenic sprouting. Proc Natl Acad Sci U S A. 2014;111(22):7968-73.
101. Buchanan CF, Verbridge SS, Vlachos PP, Rylander MN. Flow shear stress regulates endothelial barrier function and expression of angiogenic factors in a 3D microfluidic tumor vascular model. Cell adhesion & migration. 2014;8(5):517-24.
102. Jeon JS, Bersini S, Gilardi M, Dubini G, Charest JL, Moretti M, et al. Human 3D vascularized organotypic microfluidic assays to study breast cancer cell extravasation. Proc Natl Acad Sci U S A. 2015;112(1):214-9.
103. Wang XY, Pei Y, Xie M, Jin ZH, Xiao YS, Wang Y, et al. An artificial blood vessel implanted three-dimensional microsystem for modeling transvascular migration of tumor cells. Lab Chip. 2015;15(4):1178-87.
104. Li M, Hotaling NA, Ku DN, Forest CR. Microfluidic thrombosis under multiple shear rates and antiplatelet therapy doses. PLoS One. 2014;9(1):e82493.
105. Muthard RW, Diamond SL. Side view thrombosis microfluidic device with controllable wall shear rate and transthrombus pressure gradient. Lab Chip. 2013;13(10):1883-91.
106. Tsui JH, Lee W, Pun SH, Kim J, Kim DH. Microfluidics-assisted in vitro drug screening and carrier production. Adv Drug Deliv Rev. 2013;65(11-12):1575-88.
107. Tsai M, Kita A, Leach J, Rounsevell R, Huang JN, Moake J, et al. In vitro modeling of the microvascular occlusion and thrombosis that occur in hematologic diseases using microfluidic technology. The Journal of clinical investigation. 2012;122(1):408-18.
108. Hu R, Li F, Lv J, He Y, Lu D, Yamada T, et al. Microfluidic analysis of pressure drop and flow behavior in hypertensive micro vessels. Biomed Microdevices. 2015;17(3):9959.
109. Franco D, Milde F, Klingauf M, Orsenigo F, Dejana E, Poulikakos D, et al. Accelerated endothelial wound healing on microstructured substrates under flow. Biomaterials. 2013;34(5):1488-97.
110. Sato M, Sasaki N, Ato M, Hirakawa S, Sato K, Sato K. Microcirculation-on-a-Chip: A Microfluidic Platform for Assaying Blood- and Lymphatic-Vessel Permeability. PLoS One. 2015;10(9):e0137301.

111. Arends F, Sellner S, Seifert P, Gerland U, Rehberg M, Lieleg O. A microfluidics approach to study the accumulation of molecules at basal lamina interfaces. Lab Chip. 2015;15(16):3326-34.

112. Chrobak KM, Potter DR, Tien J. Formation of perfused, functional microvascular tubes in vitro. Microvasc Res. 2006;71(3):185-96.

113. Lee H, Kim S, Chung M, Kim JH, Jeon NL. A bioengineered array of 3D microvessels for vascular permeability assay. Microvasc Res. 2014;91:90-8.

114. Price GM, Wong KH, Truslow JG, Leung AD, Acharya C, Tien J. Effect of mechanical factors on the function of engineered human blood microvessels in microfluidic collagen gels. Biomaterials. 2010;31(24):6182-9.

115. Li LM, Wang XY, Hu LS, Chen RS, Huang Y, Chen SJ, et al. Vascular lumen simulation and highly-sensitive nitric oxide detection using three-dimensional gelatin chip coupled to TiC/C nanowire arrays microelectrode. Lab Chip. 2012;12(21):4249-56.

116. Shao J, Wu L, Wu J, Zheng Y, Zhao H, Jin Q, et al. Integrated microfluidic chip for endothelial cells culture and analysis exposed to a pulsatile and oscillatory shear stress. Lab Chip. 2009;9(21):3118-25.

117. Zheng W, Jiang B, Wang D, Zhang W, Wang Z, Jiang X. A microfluidic flow-stretch chip for investigating blood vessel biomechanics. Lab Chip. 2012;12(18):3441-50.

118. Wang JC, Bennett M. Aging and atherosclerosis: mechanisms, functional consequences, and potential therapeutics for cellular senescence. Circ Res. 2012;111(2):245-59.

119. Harvey A, Montezano AC, Touyz RM. Vascular biology of ageing-Implications in hypertension. J Mol Cell Cardiol. 2015;83:112-21.

120. Mozaffarian D, Benjamin EJ, Go AS, Arnett DK, Blaha MJ, Cushman M, et al. Heart disease and stroke statistics--2015 update: a report from the American Heart Association. Circulation. 2015;131(4):e29-322.

121. Assar ME, Angulo J, Rodriguez-Manas L. Diabetes and ageing-induced vascular inflammation. J Physiol. 2016;594(8):2125-46.

122. Ungvari Z, Csiszar A, Kaley G. Vascular inflammation in aging. Herz. 2004;29(8):733-40.

123. Chung HY, Sung B, Jung KJ, Zou Y, Yu BP. The molecular inflammatory process in aging. Antioxid Redox Signal. 2006;8(3-4):572-81.

124. Zou Y, Yoon S, Jung KJ, Kim CH, Son TG, Kim MS, et al. Upregulation of aortic adhesion molecules during aging. The journals of gerontology Series A, Biological sciences and medical sciences. 2006;61(3):232-44.

125. Maggio M, Guralnik JM, Longo DL, Ferrucci L. Interleukin-6 in aging and chronic disease: a magnificent pathway. The journals of gerontology Series A, Biological sciences and medical sciences. 2006;61(6):575-84.

126. Humbert M, Monti G, Brenot F, Sitbon O, Portier A, Grangeot-Keros L, et al. Increased interleukin-1 and interleukin-6 serum concentrations in severe primary pulmonary hypertension. American journal of respiratory and critical care medicine. 1995;151(5):1628-31.

127. Chamarthi B, Williams GH, Ricchiuti V, Srikumar N, Hopkins PN, Luther JM, et al. Inflammation and hypertension: the interplay of interleukin-6, dietary sodium, and the renin-angiotensin system in humans. Am J Hypertens. 2011;24(10):1143-8.

128. Kranzhofer R, Schmidt J, Pfeiffer CA, Hagl S, Libby P, Kubler W. Angiotensin induces inflammatory activation of human vascular smooth muscle cells. Arteriosclerosis, thrombosis, and vascular biology. 1999;19(7):1623-9.

129. Bautista LE, Vera LM, Arenas IA, Gamarra G. Independent association between inflammatory markers (C-reactive protein, interleukin-6, and TNF-alpha) and essential hypertension. Journal of human hypertension. 2005;19(2):149-54.

130. Harrison DG, Guzik TJ, Lob HE, Madhur MS, Marvar PJ, Thabet SR, et al. Inflammation, immunity, and hypertension. Hypertension. 2011;57(2):132-40.

131. Rodriguez-Menocal L, Faridi MH, Martinez L, Shehadeh LA, Duque JC, Wei Y, et al. Macrophage-derived IL-18 and increased fibrinogen deposition are age-related inflammatory signatures of vascular remodeling. American journal of physiology Heart and circulatory physiology. 2014;306(5):H641-53.

132. Zampetaki A, Zhang Z, Hu Y, Xu Q. Biomechanical stress induces IL-6 expression in smooth muscle cells via Ras/Rac1-p38 MAPK-NF-kappaB signaling pathways. American journal of physiology Heart and circulatory physiology. 2005;288(6):H2946-54.

133. Csiszar A, Wang M, Lakatta EG, Ungvari Z. Inflammation and endothelial dysfunction during aging: role of NF-kappaB. J Appl Physiol (1985). 2008;105(4):1333-41.

134. Donato AJ, Gano LB, Eskurza I, Silver AE, Gates PE, Jablonski K, et al. Vascular endothelial dysfunction with aging: endothelin-1 and endothelial nitric oxide synthase. American journal of physiology Heart and circulatory physiology. 2009;297(1):H425-32.

135. Dikalov SI, Nazarewicz RR, Bikineyeva A, Hilenski L, Lassegue B, Griendling KK, et al. Nox2-induced production of mitochondrial superoxide in angiotensin II-mediated endothelial oxidative stress and hypertension. Antioxid Redox Signal. 2014;20(2):281-94.

136. Dikalova A, Clempus R, Lassegue B, Cheng G, McCoy J, Dikalov S, et al. Nox1 overexpression potentiates angiotensin II-induced hypertension and vascular smooth muscle hypertrophy in transgenic mice. Circulation. 2005;112(17):2668-76.

137. El Assar M, Angulo J, Rodriguez-Manas L. Oxidative stress and vascular inflammation in aging. Free Radic Biol Med. 2013;65:380-401.

138. Gonzalez J, Valls N, Brito R, Rodrigo R. Essential hypertension and oxidative stress: New insights. World J Cardiol. 2014;6(6):353-66.

139. Lozhkin A, Vendrov AE, Pan H, Wickline SA, Madamanchi NR, Runge MS. NADPH oxidase 4 regulates vascular inflammation in aging and atherosclerosis. J Mol Cell Cardiol. 2017;102:10-21.

140. Mata-Greenwood E, Grobe A, Kumar S, Noskina Y, Black SM. Cyclic stretch increases VEGF expression in pulmonary arterial smooth muscle cells via TGF-beta1 and reactive oxygen species: a requirement for NAD(P)H oxidase. Am J Physiol Lung Cell Mol Physiol. 2005;289(2):L288-9.

141. Touyz RM, Chen X, Tabet F, Yao G, He G, Quinn MT, et al. Expression of a functionally active gp91phox-containing neutrophil-type NAD(P)H oxidase in smooth muscle cells from human resistance arteries: regulation by angiotensin II. Circ Res. 2002;90(11):1205-13.

142. Ungvari Z, Kaley G, de Cabo R, Sonntag WE, Csiszar A. Mechanisms of vascular aging: new perspectives. The journals of gerontology Series A, Biological sciences and medical sciences. 2010;65(10):1028-41.

143. Ungvari Z, Sonntag WE, Csiszar A. Mitochondria and aging in the vascular system. Journal of molecular medicine. 2010;88(10):1021-7.

144. Jurk D, Wilson C, Passos JF, Oakley F, Correia-Melo C, Greaves L, et al. Chronic inflammation induces telomere dysfunction and accelerates ageing in mice. Nature communications. 2014;2:4172.

145. Jain MK, Ridker PM. Anti-inflammatory effects of statins: clinical evidence and basic mechanisms. Nat Rev Drug Discov. 2005;4(12):977-87.

146. Marcuzzi A, De Leo L, Decorti G, Crovella S, Tommasini A, Pontillo A. The farnesyltransferase inhibitors tipifarnib and lonafarnib inhibit cytokines secretion in a cellular model of mevalonate kinase deficiency. Pediatric research. 2011;70(1):78-82.

147. Csiszar A, Labinskyy N, Jimenez R, Pinto JT, Ballabh P, Losonczy G, et al. Anti-oxidative and anti-inflammatory vasoprotective effects of caloric restriction in aging: role of circulating factors and SIRT1. Mech Ageing Dev. 2009;130(8):518-27.

148. Merideth MA, Gordon LB, Clauss S, Sachdev V, Smith AC, Perry MB, et al. Phenotype and course of Hutchinson-Gilford progeria syndrome. N Engl J Med. 2008;358(6):592-604.

149. De Sandre-Giovannoli A, Bernard R, Cau P, Navarro C, Amiel J, Boccaccio I, et al. Lamin a truncation in Hutchinson-Gilford progeria. Science. 2003;300(5628):2055.

150. Eriksson M, Brown WT, Gordon LB, Glynn MW, Singer J, Scott L, et al. Recurrent de novo point mutations in lamin A cause Hutchinson-Gilford progeria syndrome. Nature. 2003;423(6937):293-8.

151. Goldman RD, Shumaker DK, Erdos MR, Eriksson M, Goldman AE, Gordon LB, et al. Accumulation of mutant lamin A causes progressive changes in nuclear architecture in Hutchinson-Gilford progeria syndrome. Proc Natl Acad Sci U S A. 2004;101(24):8963-8.

152. Dahl KN, Ribeiro AJ, Lammerding J. Nuclear shape, mechanics, and mechanotransduction. Circ Res. 2008;102(11):1307-18.

153. Dahl KN, Scaffidi P, Islam MF, Yodh AG, Wilson KL, Misteli T. Distinct structural and mechanical properties of the nuclear lamina in Hutchinson-Gilford progeria syndrome. Proc Natl Acad Sci U S A. 2006;103(27):10271-6.

154. Cau P, Navarro C, Harhouri K, Roll P, Sigaudy S, Kaspi E, et al. Nuclear matrix, nuclear envelope and premature aging syndromes in a translational research perspective. Seminars in cell & developmental biology. 2014;29:125-47.

155. Trigueros-Motos L, Gonzalez JM, Rivera J, Andres V. Hutchinson-Gilford progeria syndrome, cardiovascular disease and oxidative stress. Frontiers in bioscience. 2011;3:1285-97.

156. McClintock D, Gordon LB, Djabali K. Hutchinson-Gilford progeria mutant lamin A primarily targets human vascular cells as detected by an anti-Lamin A G608G antibody. Proc Natl Acad Sci U S A. 2006;103(7):2154-9.

157. Zhang J, Lian Q, Zhu G, Zhou F, Sui L, Tan C, et al. A human iPSC model of Hutchinson Gilford Progeria reveals vascular smooth muscle and mesenchymal stem cell defects. Cell stem cell. 2011;8(1):31-45.

158. Swift J, Ivanovska IL, Buxboim A, Harada T, Dingal PC, Pinter J, et al. Nuclear lamin-A scales with tissue stiffness and enhances matrix-directed differentiation. Science. 2013;341(6149):1240104.

159. Sterneckert JL, Reinhardt P, Scholer HR. Investigating human disease using stem cell models. Nature reviews Genetics. 2014;15(9):625-39.

160. Liu GH, Barkho BZ, Ruiz S, Diep D, Qu J, Yang SL, et al. Recapitulation of premature ageing with iPSCs from Hutchinson-Gilford progeria syndrome. Nature. 2011;472(7342):221-5.

161. Burtner CR, Kennedy BK. Progeria syndromes and ageing: what is the connection? Nature reviews Molecular cell biology. 2010;11(8):567-78.

162. Olive M, Harten I, Mitchell R, Beers JK, Djabali K, Cao K, et al. Cardiovascular pathology in Hutchinson-Gilford progeria: correlation with the vascular pathology of aging. Arteriosclerosis, thrombosis, and vascular biology. 2010;30(11):2301-9.

163. Dreesen O, Stewart CL. Accelerated aging syndromes, are they relevant to normal human aging? Aging. 2011;3(9):889-95.

164. Nissan X, Blondel S, Navarro C, Maury Y, Denis C, Girard M, et al. Unique preservation of neural cells in Hutchinson- Gilford progeria syndrome is due to the expression of the neural-specific miR-9 microRNA. Cell reports. 2012;2(1):1-9.

165. Brassard JA, Fekete N, Garnier A, Hoesli CA. Hutchinson-Gilford progeria syndrome as a model for vascular aging. Biogerontology. 2016;17(1):129-45.

166. Verstraeten VL, Ji JY, Cummings KS, Lee RT, Lammerding J. Increased mechanosensitivity and nuclear stiffness in Hutchinson-Gilford progeria cells: effects of farnesyltransferase inhibitors. Aging cell. 2008;7(3):383-93.

167. Osorio FG, Barcena C, Soria-Valles C, Ramsay AJ, de Carlos F, Cobo J, et al. Nuclear lamina defects cause ATM-dependent NF-kappaB activation and link accelerated aging to a systemic inflammatory response. Genes & development. 2012;26(20):2311-24.

168. NCHS C, editor Underlying Cause of Death 1999-20132015.

169. Organization WH. Prevention of Cardiovascular Disease: Guidelines for Assessment and Management of Cardiovascular Risk2007.

170. Fuster V. Top 10 cardiovascular therapies and interventions for the next decade. Nat Rev Cardiol. 2014;11(11):671-83.

171. Scannell JW, Blanckley A, Boldon H, Warrington B. Diagnosing the decline in pharmaceutical R{&}D efficiency. Nature reviews Drug discovery. 2012;11:191-200.

172. Drug Testing, Now Without the Chimp. Bloomberg Business, (2015).

173. Holmes A, Bonner F, Jones D. Assessing drug safety in human tissues - what are the barriers? Nature reviews Drug discovery. 2015;advance on:1-3.

174. Dahlin JL, Inglese J, Walters MA. Mitigating risk in academic preclinical drug discovery. Nature Reviews Drug Discovery. 2015;14:279-94.

175. Pound P, Ebrahim S, Sandercock P, Bracken MB, Roberts I. Where is the evidence that animal research benefits humans? BMJ. 2004;328(7438):514-7.

176. Bracken MB. Why animal studies are often poor predictors of human reactions to exposure. Journal of the Royal Society of Medicine. 2009;102(3):120-2.

177. Barnard ND, Kaufman SR. Animal research is wasteful and misleading. Scientific American. 1997;276.

178. Cato A, Sutton L, Cato AIII. Clinical Drug Trials and Tribulations, Revised and Expanded. 2002.

179. Mattison DR. Improving Pediatric Drug Development: Challenges, Opportunities and Lessons Learned. Frontiers in Pharmacology. 2010;1:1-2.

180. Medicine CoARDRaOPDBoHSPIo. Rare Diseases and Orphan Products: Accelerating Research and Development (2011): National Academies Press, of the National Academies Press 2010.

181. Junod SW. FDA and Clinical Drug Trials: A Short History. United States Food and Drug Administration; 2014.

182. Ralph Landau BA, Alexander Scriabine. Pharmaceutical Innovation: Revolutionizing Human Health: Chemical Heritage Foundation; 1999.

183. Paul SM, Mytelka DS, Dunwiddie CT, Persinger CC, Munos BH, Lindborg SR, et al. How to improve R&D productivity: the pharmaceutical industry's grand challenge. Nat Rev Drug Discov. 2010;9(3):203-14.

184. Alcendor DJ, Block III FE, Cliffel DE, Daniels JS, Ellacott KLJ, Goodwin CR, et al. Neurovascular unit on a chip: implications for translational applications. Stem Cell Research {&} Therapy. 2013;4:1-5.

185. Mathur A, Loskill P, Shao K, Huebsch N, Hong S, Marcus SG, et al. Human iPSC-based Cardiac Microphysiological System For Drug Screening Applications. Scientific Reports. 2015;5:8883.

186. Wang G, McCain ML, Yang L, He A, Pasqualini FS, Agar A, et al. Modeling the mitochondrial cardiomyopathy of Barth syndrome with iPSC and heart-on-chip technologies. Nature Methods. 2014;20:616-23.

187. Vladisavljevic GT, Khalid N, Neves MA, Kuroiwa T, Nakajima M, Uemura K, et al. Industrial lab-on-a-chip: design, applications and scale-up for drug discovery and delivery. Adv Drug Deliv Rev. 2013;65(11-12):1626-63.

188. Davis MJ, Hill MA. Signaling mechanisms underlying the vascular myogenic response. Physiological reviews. 1999;79(2):387-423.

189. Stefanadis C, Stratos C, Vlachopoulos C, Marakas S, Boudoulas H, Kallikazaros I, et al. Pressure-diameter relation of the human aorta. A new method of determination by the application of a special ultrasonic dimension catheter. Circulation. 1995;92(8):2210-9.

190. Williams B. Mechanical influences on vascular smooth muscle cell function. Journal of hypertension. 1998;16(12 Pt 2):1921-9.

191. Anwar MA, Shalhoub J, Lim CS, Gohel MS, Davies AH. The effect of pressure-induced mechanical stretch on vascular wall differential gene expression. Journal of vascular research. 2012;49(6):463-78.

192. Heerkens EH, Izzard AS, Heagerty AM. Integrins, vascular remodeling, and hypertension. Hypertension. 2007;49(1):1-4.

193. Rensen SS, Doevendans PA, van Eys GJ. Regulation and characteristics of vascular smooth muscle cell phenotypic diversity. Netherlands heart journal : monthly journal of the Netherlands Society of Cardiology and the Netherlands Heart Foundation. 2007;15(3):100-8.

194. Lu D, Kassab GS. Role of shear stress and stretch in vascular mechanobiology. Journal of the Royal Society, Interface / the Royal Society. 2011;8(63):1379-85.

195. Savoia C, Schiffrin EL. Inflammation in hypertension. Current opinion in nephrology and hypertension. 2006;15(2):152-8.

196. Lopez-Otin C, Blasco MA, Partridge L, Serrano M, Kroemer G. The hallmarks of aging. Cell. 2013;153(6):1194-217.

197. Polacheck WJ, Li R, Uzel SG, Kamm RD. Microfluidic platforms for mechanobiology. Lab Chip. 2013;13(12):2252-67.

198. Bhatia SN, Ingber DE. Microfluidic organs-on-chips. Nature biotechnology. 2014;32(8):760-72.

199. Ribas J, Sadeghi H, Manbachi A, Leijten J, Brinegar K, Zhang YS, et al. Cardiovascular Organ-on-a-Chip Platforms for Drug Discovery and Development. Applied In Vitro Toxicology. 2016;2(2):82-96.

200. Huh D, Matthews BD, Mammoto A, Montoya-Zavala M, Hsin HY, Ingber DE. Reconstituting organ-level lung functions on a chip. Science. 2010;328(5986):1662-8.

201. Huh D, Leslie DC, Matthews BD, Fraser JP, Jurek S, Hamilton GA, et al. A human disease model of drug toxicity-induced pulmonary edema in a lung-on-a-chip microdevice. Sci Transl Med. 2012;4(159):159ra47.

202. Douville NJ, Zamankhan P, Tung YC, Li R, Vaughan BL, Tai CF, et al. Combination of fluid and solid mechanical stresses contribute to cell death and detachment in a microfluidic alveolar model. Lab Chip. 2011;11(4):609-19.

203. Kim HJ, Huh D, Hamilton G, Ingber DE. Human gut-on-a-chip inhabited by microbial flora that experiences intestinal peristalsis-like motions and flow. Lab Chip. 2012;12(12):2165-74.

204. Kim HJ, Ingber DE. Gut-on-a-Chip microenvironment induces human intestinal cells to undergo villus differentiation. Integrative biology : quantitative biosciences from nano to macro. 2013;5(9):1130-40.

205. Kim HJ, Li H, Collins JJ, Ingber DE. Contributions of microbiome and mechanical deformation to intestinal bacterial overgrowth and inflammation in a human gut-on-a-chip. Proc Natl Acad Sci U S A. 2016;113(1):E7-E15.

206. Lee J, Wong M, Smith Q, Baker AB. A novel system for studying mechanical strain waveform-dependent responses in vascular smooth muscle cells. Lab Chip. 2013;13(23):4573-82.

207. Shao Y, Tan X, Novitski R, Muqaddam M, List P, Williamson L, et al. Uniaxial cell stretching device for live-cell imaging of mechanosensitive cellular functions. The Review of scientific instruments. 2013;84(11):114304.

208. Sinha R, Le Gac S, Verdonschot N, van den Berg A, Koopman B, Rouwkema J. A medium throughput device to study the effects of combinations of surface strains and fluid-flow shear stresses on cells. Lab Chip. 2015;15(2):429-39.
209. Meza D, Abejar L, Rubenstein DA, Yin W. A Shearing-Stretching Device That Can Apply Physiological Fluid Shear Stress and Cyclic Stretch Concurrently to Endothelial Cells. Journal of biomechanical engineering. 2016;138(3).
210. Zhang W, Zhang YS, Bakht SM, Aleman J, Shin SR, Yue K, et al. Elastomeric free-form blood vessels for interconnecting organs on chip systems. Lab Chip. 2016;16(9):1579-86.
211. Blagosklonny MV. Progeria, rapamycin and normal aging: recent breakthrough. Aging. 2011;3(7):685-91.
212. Blondel S, Egesipe AL, Picardi P, Jaskowiak AL, Notarnicola M, Ragot J, et al. Drug screening on Hutchinson Gilford progeria pluripotent stem cells reveals aminopyrimidines as new modulators of farnesylation. Cell death & disease. 2016;7:e2105.
213. Pritchard RH, Lava P, Debruyne D, Terentjev EM. Precise determination of the Poisson ratio in soft materials with 2D digital image correlation. Soft Matter. 2013;9(26):6037-45.
214. Miller BG, Gattone VH, 2nd, Overhage JM, Bohlen HG, Evan AP. Morphological evaluation of vascular smooth muscle cell: length and width from a single scanning electron micrograph of microvessels. The Anatomical record. 1986;216(1):95-103.
215. Costa KD. Single-cell elastography: probing for disease with the atomic force microscope. Disease markers. 2003;19(2-3):139-54.
216. Libby P, O'Brien KV. Culture of quiescent arterial smooth muscle cells in a defined serum-free medium. Journal of cellular physiology. 1983;115(2):217-23.
217. Vazao H, das Neves RP, Graos M, Ferreira L. Towards the maturation and characterization of smooth muscle cells derived from human embryonic stem cells. PLoS One. 2011;6(3):e17771.
218. Ugolini GS, Rasponi M, Pavesi A, Santoro R, Kamm R, Fiore GB, et al. On-chip assessment of human primary cardiac fibroblasts proliferative responses to uniaxial cyclic mechanical strain. Biotechnol Bioeng. 2016;113(4):859-69.
219. Zheng W, Huang R, Jiang B, Zhao Y, Zhang W, Jiang X. An Early-Stage Atherosclerosis Research Model Based on Microfluidics. Small. 2016;12(15):2022-34.
220. Aragona M, Panciera T, Manfrin A, Giulitti S, Michielin F, Elvassore N, et al. A mechanical checkpoint controls multicellular growth through YAP/TAZ regulation by actin-processing factors. Cell. 2013;154(5):1047-59.

221. Zhou J, Niklason LE. Microfluidic artificial "vessels" for dynamic mechanical stimulation of mesenchymal stem cells. Integrative biology : quantitative biosciences from nano to macro. 2012;4(12):1487-97.

222. Wilson E, Sudhir K, Ives HE. Mechanical strain of rat vascular smooth muscle cells is sensed by specific extracellular matrix/integrin interactions. The Journal of clinical investigation. 1995;96(5):2364-72.

223. Greiner AM, Chen H, Spatz JP, Kemkemer R. Cyclic tensile strain controls cell shape and directs actin stress fiber formation and focal adhesion alignment in spreading cells. PLoS One. 2013;8(10):e77328.

224. Liu B, Qu MJ, Qin KR, Li H, Li ZK, Shen BR, et al. Role of cyclic strain frequency in regulating the alignment of vascular smooth muscle cells in vitro. Biophysical journal. 2008;94(4):1497-507.

225. Albinsson S, Nordstrom I, Hellstrand P. Stretch of the vascular wall induces smooth muscle differentiation by promoting actin polymerization. The Journal of biological chemistry. 2004;279(33):34849-55.

226. Bader M, Peters J, Baltatu O, Muller DN, Luft FC, Ganten D. Tissue renin-angiotensin systems: new insights from experimental animal models in hypertension research. Journal of molecular medicine. 2001;79(2-3):76-102.

227. Hardin CD, Vallejo J. Caveolins in vascular smooth muscle: form organizing function. Cardiovascular research. 2006;69(4):808-15.

228. Yu J, Bergaya S, Murata T, Alp IF, Bauer MP, Lin MI, et al. Direct evidence for the role of caveolin-1 and caveolae in mechanotransduction and remodeling of blood vessels. The Journal of clinical investigation. 2006;116(5):1284-91.

229. Grayson TH, Ohms SJ, Brackenbury TD, Meaney KR, Peng K, Pittelkow YE, et al. Vascular microarray profiling in two models of hypertension identifies caveolin-1, Rgs2 and Rgs5 as antihypertensive targets. BMC genomics. 2007;8:404.

230. Patel HH, Zhang S, Murray F, Suda RY, Head BP, Yokoyama U, et al. Increased smooth muscle cell expression of caveolin-1 and caveolae contribute to the pathophysiology of idiopathic pulmonary arterial hypertension. FASEB journal : official publication of the Federation of American Societies for Experimental Biology. 2007;21(11):2970-9.

231. Wang KY, Lee MF, Ho HC, Liang KW, Liu CC, Tsai WJ, et al. Serum Caveolin-1 as a Novel Biomarker in Idiopathic Pulmonary Artery Hypertension. BioMed research international. 2015;2015:173970.

232. Golembeski SM, West J, Tada Y, Fagan KA. Interleukin-6 causes mild pulmonary hypertension and augments hypoxia-induced pulmonary hypertension in mice. Chest. 2005;128(6 Suppl):572S-3S.

233. Datla SR, Griendling KK. Reactive oxygen species, NADPH oxidases, and hypertension. Hypertension. 2010;56(3):325-30.
234. Paravicini TM, Touyz RM. NADPH oxidases, reactive oxygen species, and hypertension: clinical implications and therapeutic possibilities. Diabetes care. 2008;31 Suppl 2:S170-80.
235. Kojima M, Shiojima I, Yamazaki T, Komuro I, Zou Z, Wang Y, et al. Angiotensin II receptor antagonist TCV-116 induces regression of hypertensive left ventricular hypertrophy in vivo and inhibits the intracellular signaling pathway of stretch-mediated cardiomyocyte hypertrophy in vitro. Circulation. 1994;89(5):2204-11.
236. ten Freyhaus H, Huntgeburth M, Wingler K, Schnitker J, Baumer AT, Vantler M, et al. Novel Nox inhibitor VAS2870 attenuates PDGF-dependent smooth muscle cell chemotaxis, but not proliferation. Cardiovascular research. 2006;71(2):331-41.
237. Kappert K, Schmidt G, Doerr G, Wollert-Wulf B, Fleck E, Graf K. Angiotensin II and PDGF-BB stimulate beta(1)-integrin-mediated adhesion and spreading in human VSMCs. Hypertension. 2000;35(1 Pt 2):255-61.
238. North BJ, Sinclair DA. The intersection between aging and cardiovascular disease. Circ Res. 2012;110(8):1097-108.
239. Cao K, Blair CD, Faddah DA, Kieckhaefer JE, Olive M, Erdos MR, et al. Progerin and telomere dysfunction collaborate to trigger cellular senescence in normal human fibroblasts. The Journal of clinical investigation. 2011;121(7):2833-44.
240. Austin ED, Ma L, LeDuc C, Berman Rosenzweig E, Borczuk A, Phillips JA, 3rd, et al. Whole exome sequencing to identify a novel gene (caveolin-1) associated with human pulmonary arterial hypertension. Circulation Cardiovascular genetics. 2012;5(3):336-43.
241. Fahmy RG, Waldman A, Zhang G, Mitchell A, Tedla N, Cai H, et al. Suppression of vascular permeability and inflammation by targeting of the transcription factor c-Jun. Nat Biotechnol. 2006;24(7):856-63.
242. Collado M, Blasco MA, Serrano M. Cellular senescence in cancer and aging. Cell. 2007;130(2):223-33.
243. Endisha H, Merrill-Schools J, Zhao M, Bristol M, Wang X, Kubben N, et al. Restoring SIRT6 Expression in Hutchinson-Gilford Progeria Syndrome Cells Impedes Premature Senescence and Formation of Dysmorphic Nuclei. Pathobiology : journal of immunopathology, molecular and cellular biology. 2015;82(1):9-20.
244. Acosta JC, O'Loghlen A, Banito A, Guijarro MV, Augert A, Raguz S, et al. Chemokine signaling via the CXCR2 receptor reinforces senescence. Cell. 2008;133(6):1006-18.
245. Kuilman T, Michaloglou C, Vredeveld LC, Douma S, van Doorn R, Desmet CJ, et al. Oncogene-induced senescence relayed by an interleukin-dependent inflammatory network. Cell. 2008;133(6):1019-31.

246. Bifulco M, D'Alessandro A, Paladino S, Malfitano AM, Notarnicola M, Caruso MG, et al. N6-isopentenyladenosine improves nuclear shape in fibroblasts from humans with progeroid syndromes by inhibiting the farnesylation of prelamin A. The FEBS journal. 2013;280(23):6223-32.

247. Varela I, Pereira S, Ugalde AP, Navarro CL, Suarez MF, Cau P, et al. Combined treatment with statins and aminobisphosphonates extends longevity in a mouse model of human premature aging. Nat Med. 2008;14(7):767-72.

248. Capell BC, Erdos MR, Madigan JP, Fiordalisi JJ, Varga R, Conneely KN, et al. Inhibiting farnesylation of progerin prevents the characteristic nuclear blebbing of Hutchinson-Gilford progeria syndrome. Proc Natl Acad Sci U S A. 2005;102(36):12879-84.

249. Yang SH, Meta M, Qiao X, Frost D, Bauch J, Coffinier C, et al. A farnesyltransferase inhibitor improves disease phenotypes in mice with a Hutchinson-Gilford progeria syndrome mutation. The Journal of clinical investigation. 2006;116(8):2115-21.

250. Cao K, Graziotto JJ, Blair CD, Mazzulli JR, Erdos MR, Krainc D, et al. Rapamycin reverses cellular phenotypes and enhances mutant protein clearance in Hutchinson-Gilford progeria syndrome cells. Sci Transl Med. 2011;3(89):89ra58.

251. Schonbeck U, Libby P. Inflammation, immunity, and HMG-CoA reductase inhibitors: statins as antiinflammatory agents? Circulation. 2004;109(21 Suppl 1):II18-26.

252. Weitz-Schmidt G. Statins as anti-inflammatory agents. Trends in Pharmacological Sciences. 2002;23(10):482-7.

253. Gordon LB, Kleinman ME, Miller DT, Neuberg DS, Giobbie-Hurder A, Gerhard-Herman M, et al. Clinical trial of a farnesyltransferase inhibitor in children with Hutchinson-Gilford progeria syndrome. Proc Natl Acad Sci U S A. 2012;109(41):16666-71.

254. Zernike F. Phase contrast, a new method for the microscopic observation of transparent objects. Physica. 1942;9(7):686-98.

255. Pluta M, editor Nomarski's DIC microscopy: a review. Phase Contrast and Differential Interference Contrast Imaging Techniques and Applications; 1994: International Society for Optics and Photonics.

256. Lichtman JW, Conchello J-A. Fluorescence microscopy. Nat Meth. 2005;2(12):910-9.

257. Hell SW, Wichmann J. Breaking the diffraction resolution limit by stimulated emission: stimulated-emission-depletion fluorescence microscopy. Opt Lett. 1994;19(11):780-2.

258. Klar TA, Hell SW. Subdiffraction resolution in far-field fluorescence microscopy. Opt Lett. 1999;24(14):954-6.

259. Denk W, Strickler JH, Webb WW. Two-photon laser scanning fluorescence microscopy. Science. 1990;248(4951):73-6.

260. Minsky M. Memoir on inventing the confocal scanning microscope. Scanning. 1988;10(4):128-38.

261. Figeys D, Pinto D. Lab-on-a-chip: a revolution in biological and medical sciences. Analytical chemistry. 2000;72(9):330 A-5 A.

262. Whitesides GM. The origins and the future of microfluidics. Nature. 2006;442(7101):368-73.

263. El-Ali J, Sorger PK, Jensen KF. Cells on chips. Nature. 2006;442(7101):403-11.

264. Huh D, Hamilton GA, Ingber DE. From 3D cell culture to organs-on-chips. Trends in Cell Biology. 2011;21(12):745-54.

265. Moraes C, Mehta G, Lesher-Perez SC, Takayama S. Organs-on-a-chip: a focus on compartmentalized microdevices. Annals of biomedical engineering. 2012;40(6):1211-27.

266. Bhatia SN, Ingber DE. Microfluidic organs-on-chips. Nat Biotechnol. 2014;32(8):760-72.

267. Moya ML, George SC. Integrating in vitro organ-specific function with the microcirculation. Current opinion in chemical engineering. 2014;3:102-11.

268. Sei Y, Justus K, LeDuc P, Kim Y. Engineering living systems on chips: from cells to human on chips. Microfluid Nanofluid. 2014:1-14.

269. Wikswo JP. The relevance and potential roles of microphysiological systems in biology and medicine. Experimental Biology and Medicine. 2014;239(9):1061-72.

270. Esch M, King T, Shuler M. The role of body-on-a-chip devices in drug and toxicity studies. Annual review of biomedical engineering. 2011;13:55-72.

271. Ghaemmaghami AM, Hancock MJ, Harrington H, Kaji H, Khademhosseini A. Biomimetic tissues on a chip for drug discovery. Drug Discov Today. 2012;17(3):173-81.

272. Selimović Š, Dokmeci MR, Khademhosseini A. Organs-on-a-chip for drug discovery. Current Opinion in Pharmacology. 2013;13(5):829-33.

273. Bhise NS, Ribas J, Manoharan V, Zhang YS, Polini A, Massa S, et al. Organ-on-a-chip platforms for studying drug delivery systems. J Controlled Release. 2014;190(0):82-93.

274. Ebrahimkhani MR, Young CL, Lauffenburger DA, Griffith LG, Borenstein JT. Approaches to in vitro tissue regeneration with application for human disease modeling and drug development. Drug discovery today. 2014;19(6):754-62.

275. Polini A, Prodanov L, Bhise NS, Manoharan V, Dokmeci MR, Khademhosseini A. Organs-on-a-chip: a new tool for drug discovery. Expert opinion on drug discovery. 2014;9(4):335-52.

276. Zhang YS, Khademhosseini A. Seeking the Right Context for Evaluating Nanomedicine: from Tissue Models in Petri Dishes to Microfluidic Organs-on-a-Chip. Nanomedicine. 2015;10:685-8.

277. Greenbaum A, Luo W, Su TW, Gorocs Z, Xue L, Isikman SO, et al. Imaging without lenses: achievements and remaining challenges of wide-field on-chip microscopy. Nat Methods. 2012;9(9):889-95.

278. Greenbaum A, Zhang Y, Feizi A, Chung PL, Luo W, Kandukuri SR, et al. Wide-field computational imaging of pathology slides using lens-free on-chip microscopy. Sci Transl Med. 2014;6(267):267ra175.

279. Ozcan A, Demirci U. Ultra wide-field lens-free monitoring of cells on-chip. Lab on a Chip. 2008;8(1):98-106.

280. Coskun AF, Su T-W, Ozcan A. Wide field-of-view lens-free fluorescent imaging on a chip. Lab on a Chip. 2010;10(7):824-7.

281. Kim SB, Bae H, Cha JM, Moon SJ, Dokmeci MR, Cropek DM, et al. A cell-based biosensor for real-time detection of cardiotoxicity using lensfree imaging. Lab on a Chip. 2011;11(10):1801-7.

282. Cybulski JS, Clements J, Prakash M. Foldscope: origami-based paper microscope. PLoS One. 2014;9(6):e98781.

283. Wei Q, Luo W, Chiang S, Kappel T, Mejia C, Tseng D, et al. Imaging and sizing of single DNA molecules on a mobile phone. ACS nano. 2014;8(12):12725-33.

284. Wei Q, Qi H, Luo W, Tseng D, Ki SJ, Wan Z, et al. Fluorescent imaging of single nanoparticles and viruses on a smart phone. ACS nano. 2013;7(10):9147-55.

285. Kim SB, Koo K-i, Bae H, Dokmeci MR, Hamilton GA, Bahinski A, et al. A mini-microscope for in situ monitoring of cells. Lab on a chip. 2012;12(20):3976-82.

286. Khademhosseini A, Eng G, Yeh J, Kucharczyk P, Langer R, Vunjak-Novakovic G, et al. Microfluidic patterning for fabrication of contractile cardiac organoids. Biomedical Microdevices. 2007;9(2):149-57.

287. Shin SR, Jung SM, Zalabany M, Kim K, Zorlutuna P, Kim Sb, et al. Carbon-Nanotube-Embedded Hydrogel Sheets for Engineering Cardiac Constructs and Bioactuators. ACS nano. 2013;7(3):2369-80.

288. Nichol JW, Koshy ST, Bae H, Hwang CM, Yamanlar S, Khademhosseini A. Cell-laden microengineered gelatin methacrylate hydrogels. Biomaterials. 2010;31(21):5536-44.

289. Khetani SR, Bhatia SN. Microscale culture of human liver cells for drug development. Nat Biotech. 2008;26(1):120-6.

290. Lan S-F, Safiejko-Mroczka B, Starly B. Long-term cultivation of HepG2 liver cells encapsulated in alginate hydrogels: A study of cell viability, morphology and drug metabolism. Toxicology in Vitro. 2010;24(4):1314-23.

291. Mao S, Gao D, Liu W, Wei H, Lin J-M. Imitation of drug metabolism in human liver and cytotoxicity assay using a microfluidic device coupled to mass spectrometric detection. Lab on a Chip. 2012;12(1):219-26.

292. Grosberg A, Alford PW, McCain ML, Parker KK. Ensembles of engineered cardiac tissues for physiological and pharmacological study: heart on a chip. Lab Chip. 2011;11(24):4165-73.

293. Agarwal A, Goss JA, Cho A, McCain ML, Parker KK. Microfluidic heart on a chip for higher throughput pharmacological studies. Lab on a Chip. 2013;13(18):3599-608.
294. Menna P, Salvatorelli E, Minotti G. Cardiotoxicity of Antitumor Drugs†. Chemical research in toxicology. 2008;21(5):978-89.
295. Manley P, Lelkes PI. A novel real-time system to monitor cell aggregation and trajectories in rotating wall vessel bioreactors. Journal of biotechnology. 2006;125(3):416-24.
296. Chang TT, Hughes-Fulford M. Monolayer and Spheroid Culture of Human Liver Hepatocellular Carcinoma Cell Line Cells Demonstrate Distinct Global Gene Expression Patterns and Functional Phenotypes. Tissue Engineering Part A. 2008;15(3):559-67.
297. Zhang YS, Aleman J, Arneri A, Bersini S, Piraino F, Shin SR, et al. From Cardiac Tissue Engineering to Heart-on-a-Chip: Beating Challenges. Biomed Mater. 2015.
298. Shin SR, Bae H, Cha JM, Mun JY, Chen Y-C, Tekin H, et al. Carbon nanotube reinforced hybrid microgels as scaffold materials for cell encapsulation. ACS nano. 2011;6(1):362-72.
299. Wikswo JP, Block FE, Cliffel DE, Goodwin CR, Marasco CC, Markov DA, et al. Engineering Challenges for Instrumenting and Controlling Integrated Organ-on-Chip Systems. Biomedical Engineering, IEEE Transactions on. 2013;60(3):682-90.
300. Wikswo JP, Curtis EL, Eagleton ZE, Evans BC, Kole A, Hofmeister LH, et al. Scaling and systems biology for integrating multiple organs-on-a-chip. Lab Chip. 2013;13(18):3496-511.
301. Thévenot DR, Toth K, Durst RA, Wilson GS. Electrochemical biosensors: recommended definitions and classification1. Biosensors and Bioelectronics. 2001;16(1–2):121-31.
302. Chan C-M, Chan M-Y, Zhang M, Lo W, Wong K-Y. The performance of oxygen sensing films with ruthenium-adsorbed fumed silica dispersed in silicone rubber. Analyst. 1999;124(5):691-4.
303. Jiang K, Thomas PC, Forry SP, DeVoe DL, Raghavan SR. Microfluidic synthesis of monodisperse PDMS microbeads as discrete oxygen sensors. Soft Matter. 2012;8(4):923-6.
304. Sud D, Mehta G, Mehta K, Linderman J, Takayama S, Mycek M. Optical imaging in microfluidic bioreactors enables oxygen monitoring for continuous cell culture. Journal of biomedical optics. 2006;11(5):50504-6.
305. Mehta G, Mehta K, Sud D, Song JW, Bersano-Begey T, Futai N, et al. Quantitative measurement and control of oxygen levels in microfluidic poly (dimethylsiloxane) bioreactors during cell culture. Biomedical microdevices. 2007;9(2):123-34.
306. Nardini C, Carrara S, Liu Y, Devescovi V, Lu Y, Zhou X. i-Needle: Detecting the biological mechanisms of acupuncture. Science. 2014;346(EPFL-ARTICLE-204677):S21-S2.

307. Ottesen EA, Hong JW, Quake SR, Leadbetter JR. Microfluidic digital PCR enables multigene analysis of individual environmental bacteria. science. 2006;314(5804):1464-7.
308. Groisman A, Enzelberger M, Quake SR. Microfluidic memory and control devices. Science. 2003;300(5621):955-8.
309. Thorsen T, Maerkl SJ, Quake SR. Microfluidic large-scale integration. Science. 2002;298(5593):580-4.
310. Unger MA, Chou H-P, Thorsen T, Scherer A, Quake SR. Monolithic microfabricated valves and pumps by multilayer soft lithography. Science. 2000;288(5463):113-6.
311. Beebe DJ, Mensing GA, Walker GM. Physics and applications of microfluidics in biology. Annual review of biomedical engineering. 2002;4(1):261-86.
312. Stone HA, Stroock AD, Ajdari A. Engineering flows in small devices: microfluidics toward a lab-on-a-chip. Annu Rev Fluid Mech. 2004;36:381-411.
313. Bhise NS, Manoharan V, Massa S, Tamayol A, Ghaderi M, Miscuglio M, et al. A Liver-on-a-Chip Platform with Bioprinted Hepatic Spheroids. Biofabrication. 2015.
314. Ebrahimkhani MR, Neiman JAS, Raredon MSB, Hughes DJ, Griffith LG. Bioreactor technologies to support liver function in vitro. Advanced drug delivery reviews. 2014;69:132-57.
315. Eklund SE, Thompson RG, Snider RM, Carney CK, Wright DW, Wikswo J, et al. Metabolic discrimination of select list agents by monitoring cellular responses in a multianalyte microphysiometer. Sensors. 2009;9(3):2117-33.
316. Stradolini S, Riario S, Boero C, Baj-Rossi C, Surrel G, De Micheli G, et al. Wireless Monitoring of Endogenous and Exogenous Biomolecules on an Android Interface. IEEE Sensors Journal. 2015.
317. Laksanasopin T, Guo TW, Nayak S, Sridhara AA, Xie S, Olowookere OO, et al. A smartphone dongle for diagnosis of infectious diseases at the point of care. Science translational medicine. 2015;7(273):273re1-re1.
318. Im H, Castro CM, Shao H, Liong M, Song J, Pathania D, et al. Digital diffraction analysis enables low-cost molecular diagnostics on a smartphone. Proceedings of the National Academy of Sciences. 2015:201501815.
319. Vashist SK, Mudanyali O, Schneider EM, Zengerle R, Ozcan A. Cellphone-based devices for bioanalytical sciences. Analytical and bioanalytical chemistry. 2014;406(14):3263-77.
320. Petryayeva E, Algar WR. Multiplexed homogeneous assays of proteolytic activity using a smartphone and quantum dots. Analytical chemistry. 2014;86(6):3195-202.
321. Liang P-S, San Park T, Yoon J-Y. Rapid and reagentless detection of microbial contamination within meat utilizing a smartphone-based biosensor. Scientific reports. 2014;4.
322. Giller G. Using a Smartphone to Detect Cancer. Scientific American. 2014;310(5):28-.

323. Olivo J, Foglia L, Casulli MA, Boero C, Carrara S, De Micheli G, editors. Android Interface for Wireless Monitoring of Cell Cultures. Proceedings of the 10th International IEEE Conference BioCAS; 2014.
324. Gallegos D, Long KD, Yu H, Clark PP, Lin Y, George S, et al. Label-free biodetection using a smartphone. Lab on a Chip. 2013;13(11):2124-32.
325. Khatua S, Orrit M. Toward single-molecule microscopy on a smart phone. ACS nano. 2013;7(10):8340-3.
326. Wei Q, Qi H, Luo W, Tseng D, Ki SJ, Wan Z, et al. Fluorescent imaging of single nanoparticles and viruses on a smart phone. ACS nano. 2013;7(10):9147-55.
327. Lam SCK, Wong KL, Wong KO, Wong W, Mow WH, editors. A smartphone-centric platform for personal health monitoring using wireless wearable biosensors. Information, Communications and Signal Processing, 2009 ICICS 2009 7th International Conference on; 2009: IEEE.
328. Windmiller JR, Wang J. Wearable electrochemical sensors and biosensors: a review. Electroanalysis. 2013;25(1):29-46.
329. Shim BS, Chen W, Doty C, Xu C, Kotov NA. Smart electronic yarns and wearable fabrics for human biomonitoring made by carbon nanotube coating with polyelectrolytes. Nano letters. 2008;8(12):4151-7.
330. Iguchi S, Kudo H, Saito T, Ogawa M, Saito H, Otsuka K, et al. A flexible and wearable biosensor for tear glucose measurement. Biomedical microdevices. 2007;9(4):603-9.
331. Cortazar B, Koydemir HC, Tseng D, Feng S, Ozcan A. Quantification of plant chlorophyll content using Google Glass. Lab on a chip. 2015;15(7):1708-16.
332. Shao P, Ding H, Wang J, Liu P, Ling Q, Chen J, et al. Designing a Wearable Navigation System for Image-Guided Cancer Resection Surgery. Annals of Biomedical Engineering. 2014;42(11):2228-37.
333. Wall D, Ray W, Pathak RD, Lin SM. A Google Glass Application to Support Shoppers With Dietary Management of Diabetes. Journal of Diabetes Science and Technology. 2014;8(6):1245-6.
334. Feng S, Caire R, Cortazar B, Turan M, Wong A, Ozcan A. Immunochromatographic diagnostic test analysis using Google Glass. ACS nano. 2014;8(3):3069-79.
335. Cavallini A, Baj-Rossi C, Ghoreishizadeh S, De Micheli G, Carrara S, editors. Design, fabrication, and test of a sensor array for perspective biosensing in chronic pathologies. Proceedings of the IEEE Biomedical Circuits and Systems Conference (BioCAS 2012); 2012.
336. Ges IA, Ivanov BL, Schaffer DK, Lima EA, Werdich AA, Baudenbacher FJ. Thin-film IrO x pH microelectrode for microfluidic-based microsystems. Biosensors and Bioelectronics. 2005;21(2):248-56.

337. Zhang YS, Ribas J, Nadhman A, Aleman J, Selimović Š, Lesher-Perez SC, et al. A Cost-Effective Fluorescence Mini-Microscope with Adjustable Magnifications for Biomedical Applications. Lab on a Chip. 2015;15(18):3661-9.
338. Cavallini A, Jost TR, Ghoreishizadeh SS, Olivo J, de Beeck MO, Gorissen B, et al. A Subcutaneous Biochip for Remote Monitoring of Human Metabolism: packaging and biocompatibility assessment. Sensors Journal, IEEE. 2015;15(1):417-24.
339. Baker B. Temperature sensing technologies. AN679, Microchip Technology Inc. 1998.
340. Weiland JD, Anderson DJ, Humayun MS. In vitro electrical properties for iridium oxide versus titanium nitride stimulating electrodes. Biomedical Engineering, IEEE Transactions on. 2002;49(12):1574-9.
341. Olthuis W, Robben M, Bergveld P, Bos M, Van der Linden W. pH sensor properties of electrochemically grown iridium oxide. Sensors and Actuators B: Chemical. 1990;2(4):247-56.
342. Zhang S, Liu X, Bawa-Khalfe T, Lu L-S, Lyu YL, Liu LF, et al. Identification of the molecular basis of doxorubicin-induced cardiotoxicity. Nature medicine. 2012;18(11):1639-42.
343. Weibel DB, Kruithof M, Potenta S, Sia SK, Lee A, Whitesides GM. Torque-actuated valves for microfluidics. Analytical chemistry. 2005;77(15):4726-33.
344. Unger MA, Chou HP, Thorsen T, Scherer A, Quake SR. Monolithic microfabricated valves and pumps by multilayer soft lithography. Science. 2000;288(5463):113-6.
345. Hwang YS, Chung BG, Ortmann D, Hattori N, Moeller HC, Khademhosseini A. Microwell-mediated control of embryoid body size regulates embryonic stem cell fate via differential expression of WNT5a and WNT11. Proc Natl Acad Sci U S A. 2009;106(40):16978-83.
346. Lara J, Cooper R, Nissan J, Ginty AT, Khaw KT, Deary IJ, et al. A proposed panel of biomarkers of healthy ageing. BMC Med. 2015;13:222.
347. Mahmud A, Feely J. Arterial stiffness is related to systemic inflammation in essential hypertension. Hypertension. 2005;46(5):1118-22.
348. Zhang YS, Aleman J, Shin SR, Kilic T, Kim D, Mousavi Shaegh SA, et al. Multisensor-integrated organs-on-chips platform for automated and continual in situ monitoring of organoid behaviors. Proc Natl Acad Sci U S A. 2017;114(12):E2293-E302.
349. Osorio FG, Navarro CL, Cadinanos J, Lopez-Mejia IC, Quiros PM, Bartoli C, et al. Splicing-directed therapy in a new mouse model of human accelerated aging. Sci Transl Med. 2011;3(106):106ra7.
350. Giordano A, Avellino R, Ferraro P, Romano S, Corcione N, Romano MF. Rapamycin antagonizes NF-κB nuclear translocation activated by TNF-α in primary vascular smooth muscle cells and enhances apoptosis. American Journal of Physiology - Heart and Circulatory Physiology. 2006;290(6):H2459-H65.

351. Mendelsohn AR, Larrick JW. Rapamycin as an antiaging therapeutic?: targeting mammalian target of rapamycin to treat Hutchinson-Gilford progeria and neurodegenerative diseases. Rejuvenation Res. 2011;14(4):437-41.